Biomimetic Cilia Arrays - Fabrication, Magnetic Actuation, and Driven Fluid Transport Phenomena

by
Adam Shields

A dissertation submitted to the faculty of the University of North Carolina at Chapel Hill in partial fulfillment of the requirements for the degree of Doctor of Philosophy in the Department of Physics and Astronomy.

Chapel Hill
2010

Approved by:

Rich Superfine, Advisor

Sorin Mitran, Reader

Michael Falvo, Reader

Greg Forest, Reader

Christian Illiadis, Reader

"Terms swarm up to tempt me in the course of this description: *Greek Orthodox, Romanesque, flying buttress,* etc. These guessing words I find junked in my brain in deranged juxtaposition, like files randomly stuffed into cabinets by a dispirited secretary with no notion of what, if anything, might ever be usefully retrieved. Often all language seems this way: a monstrous compendium of embedded histories I'm helpless to understand. I employ it the way a dog drives a car, without grasping how the car came to exist or what makes a combustion engine possible. That is, of course, if dogs drove cars. They don't. Yet I go around forming sentences."

- *Chronic City*, by Jonathan Lethem

ABSTRACT
ADAM SHIELDS: Biomimetic Cilia Arrays - Fabrication, Magnetic Actuation, and Driven Fluid Transport Phenomena.
(Under the direction of Rich Superfine.)

The cilium is one of biology's most basic functional nanostructures, present on nearly every cell and increasingly realized as vital to many aspects of human health. A fundamental reason for the ubiquity of cilia is their ability to effectively interact with fluids at the microscale, where the Reynolds number is low and thus inertia is irrelevant. This ability makes cilia an attractive and popular candidate for an engineered biomimic with potential applications in microfluidics and sensing. In addition, biological ciliated systems are difficult to study for many reasons, and so I demonstrate how a functional biomimetic system can also serve as a model platform for highly controlled studies of biologically relevant, cilia-driven hydrodynamics.

Using the template-based microfabrication of a magnetic nanoparticle/polymer composite, I fabricate arrays of magnetically actuated biomimetic cilia at the scale of their biological analogues. I will discuss this fabrication technique and the magnetic actuation of these arrays to mimic the beat of biological cilia. I also report on the nature of the fluid flows driven by the cilia beat, and demonstrate how these cilia arrays can simultaneously generate long-range fluid transport and mixing in distinct fluid flow regimes. Finally, I present these results within the context of canonical hydrodynamics problems and discuss the implications for biological systems, such as the motile cilia recently discovered in the embryonic node.

ACKNOWLEDGMENTS

Often, acknowledgments are concluded with a thanks to the person who is most important to the author. In this moment, however, I can think of no one who deserves to be thanked before my wife, Kate. There is no way that without her I could have made it through the last six years, and I cannot even begin to think about what it would have been like to survive the past six weeks. My daughter Sophia is nearly two and deserves both thanks and a bit of a scowl, as the last six years would probably be more like the last five without her (of course she can hardly be blamed). I love you both!

I have always enjoyed learning about science, but I feel strongly that no one has taught me more about what it means to be a scientist than my advisor, Rich Superfine. I appreciate his ability to understand phenomena at a deep level, and I cannot count the times I've thought he was off his rocker for one idea or another, only to realize much later that he was trying to steer me towards something significant (there's another year out of the six).

The group of faculty and students I have worked with as part of NSRG are truly an amazing bunch of nerds, because in large part one would never realize that that is exactly what we all are (okay, maybe they would realize, but it would take them a minute or two). Mike Falvo and Sean Washburn have been excellent advisors as well, and each has taught me a valuable way to look at science and the world in general. I have made many friends in my time here. To Jerome Carpenter, Lamar Mair, Vinay Swaminathan, Adam Hall, Jeremy Cribb, Ricky Spero, Kwan Skinner, and everyone else, thanks for making work not such a bad place to spend six years, it sure went fast. Included in this group, but separately listed so that I can especially thank them, are the students I have worked most closely with over the years on biomimetic cilia arrays, Ben Evans and Briana Fiser. I couldn't have done it without you.

Finally, since I got my beautiful wife out of the way early, I can use my last thanks for my sister and my parents. They all deserve tremendous credit for having dealt with me all their lives. To my dad, especially, thanks for teaching me that the world is a fascinating place, and for telling me that the best way to avoid being put to work was to be found with a book in my hands. These things, more than anything else, have led me to this point.

A note on embedded videos in this thesis

For better or worse, I believe that it is difficult to fully appreciate the work in this thesis in a static format like the printed page. For that reason, a number of the figures in this document contain embedded videos, which is indicated within the figure caption. The good news is that I am confident this will enhance the experience of those who read, or even just refer to, the electronic version. The less good news is that the embedded videos are only viewable within Adobe Reader, a free pdf viewer which can be obtained here. They should work on any computer which has Quicktime, which is freely available here. For those who prefer the printed page, or have trouble with the videos, I have made an effort to have the still image (which is overlaid on the video before it is played) be informative and representative of the information in the video.

In addition, the inclusion of videos in the pdf has substantially increased the file size. If necessary, a new copy of the thesis may be saved (change the filename please!) which may disable the embedded videos and reduce the overall file size. If the reader finds that the videos have already been disabled in their electronic version, please feel free to contact me at arshields@gmail.com to obtain an original version.

for Sophia

Contents

List of Figures

List of Abbreviations

PDMS	poly-dimethylsiloxane
PC flow	Poiseuille-Couette flow
IFT	intraflagellar transport
CSF	cerebrospinal fluid
PKD	polycystic kidney disease
NVP	nodal vesicular parcel
SHH	Sonic hedgehog
RA	retinoic acid
FGF	fibroblast growth factor
MIP	minimum/maximum intensity projection
MSD	mean-square displacment

Chapter 1

INTRODUCTION

"Biology is not simply writing information; it is doing something *about it. A biological system can be exceedingly small. Many of the cells are very tiny, but they are very active; they manufacture various substances; they walk around; they wiggle; and they do all kinds of marvelous things – all on a very small scale. Also, they store information. Consider the possibility that we too can make a thing very small which does what we want – that we can manufacture an object that maneuvers at that level!"*

- Richard Feynman, excerpt from his 1959 talk
at the American Physical Society annual meeting,
"There's Plenty of Room at the Bottom:
An Invitation to Enter a New Field of Physics"

This classic presentation by Richard Feynman is often heralded as the beginning of the field of nanotechnology. As one would expect during the birth of the computer age, in 1959 Feynman's talk focused largely on the new paradigms in manufacturing and computing which could be brought about by ultra-miniaturization. Biology was not the focus of this talk. However, the above quote hints at an idea that has become one of the cornerstones of nanotechnology research in the decades since: that the amazing biological machinery developed over more than a billion years of evolution provide diverse examples of how engineering at the micro- and nanometer scales can help ignite a revolution in many aspects of materials science, chemistry, and physics.

A half century since Feynman's presentation that revolution is now well underway. From the discovery of materials like carbon nanotubes with novel material properties to the development of advanced tools for nanoscale imaging and manipulation, the last two decades have witnessed such progress that we now stand at the cusp of a new age of smart, responsive materials and products which promise paradigm shifts as dramatic as the computer age.

As Feynman realized, biology has served as a fundamental example of exactly what is possible when structures and materials are structured at the microscale. The increasingly widespread impact of such bio-inspired technologies has resulted in the field of 'biomimetics', in which fascinating and useful biological phenomena serve as models for engineered mimics which duplicate, or even improve upon, the feats of their counterparts.

While biomimetics is becoming increasingly important in technologies across many size scales, a number of examples of biological phenomena with technological appeal take advantage of materials which exhibit microscopic structure. Such materials can be endowed with properties which defy conventional experience. Broadly speaking, such properties often arise from two sources: materials whose structure utilizes forces or phenomena which do not exist at large scales or, secondly, composites which combine into a single material the advantageous properties of the base materials.

In many cases, biological phenomena which depend on microscopic structure are only appreciable when surface-to-volume ratios are large. Thus, as the absolute dimension of structures approaches the microscale, gravity becomes irrelevant and effects based on Van der Waals forces, surface tension, and other forces become dominant. Several oft-noted examples of such systems are found in geckos, the lotus leaf, and a small lizard known as the thorny devil. Geckos possess the unique ability to reversibly adhere the pads of their feet to essentially any surface, wet or dry, rough or smooth,

providing the inspiration for a new class of adhesives. The microscopic structure of the lotus leaf causes water droplets to bead up and run off, performing a self-cleaning function as dust and dirt are collected by the rolling water droplets. Finally, in a feat which contrasts the abilities of the lotus leaf, by placing its foot in contact with a small puddle or a wet patch of sand, the thorny devil can wick water along its leg, up its back, and into its mouth, effectively drinking through its foot.

Another broad class of novel nanomaterials combine dissimilar materials into composites with properties which can not be found in homogenous materials. Biology has provided ample evidence of how high-strength, lightweight materials can be formed from composite materials. Nacre, the material produced by the abalone to form its shell, is a well-documented example of such a material. It is formed with a brick-like, tiled structure of crystalline calcium carbonate, known as aragonite, with the tiles mortared together by a soft organic matrix, and which has a fracture strength orders of magnitude larger than monolithic aragonite. Another common type of composite is conductive polymers based on the inclusion of conductive particles into the polymer matrix.

The use of composite materials with engineered microscale structure is at the heart of another broad aspect of nanotechnology, the development of responsive materials. Such materials are often broken down by application into sensors and actuators. The ability to manipulate objects or fluids with actuators and the ability to measure similar types of changes with sensors are critical aspects of technology across all size scales. While there is a sense in which these ideas contrast, the means to achieving either end requires responsive materials, and in reality they are two sides of the same coin. More technically, in many cases the essential difference between a sensor and an actuator is just a switch of the input and output, for example in microphones and speakers.

In much of conventional technology, the term ‘responsive materials’ can effectively

be reduced to 'moving parts'. Machines which respond to changes at the macroscale are typically built from unresponsive materials into configurations with moving parts that allow them to effect, or be affected by, change. As we seek to bring technology into the microscale, it becomes progressively more important that the responsiveness of a sensor or actuator be an intrinsic property of the material, and not solely based on the ability to construct machines with moving parts. Such microscale technology will often be produced in environments where fluid forces predominate.

Much of biology also takes place in a liquid, and as such biology provides inspiration on how to effectively interact with fluids at the microscale in the form of the cilium and flagellum. These whip-like, motile structures are evolutionary biology's answer to the question of how to interact with fluids at the cellular level and are thus found in an astonishing array of biological systems. As nanotechnology becomes more widespread, the need for efficient mechanisms for manipulating microscale fluids will become increasingly important, and so cilia and flagella have become popular candidates for engineered biomimics.

Yet, the functionality of cilia and flagella also requires moving parts! In fact, the cilium could be considered a shining example of the use of moving parts within the cell: the ATP driven transport of molecular motors along microtubules. The configurational changes of these protein-based motors cause them to 'walk' along microtubules, the fibers which form a dynamic network within the cell and which also serve as one of the cell's primary structural components. This mechanism is the foundation for the cell's ability to move objects from place to place within itself and thus to perform and regulate many of its basic processes. In the cilium, sets of paired, or doublet, microtubules run parallel to the long axis of the cilium and form its basic structural components as well as a pathway for transport of molecular cargo through the cilium.

To the chagrin of many researchers in biomimetics, the complex internal machinery

which drives the motion of a cilium shares a commonality with many other candidates for biomimicry: a man-made counterpart which *truly* mimics the size, structure, and function of the biological cilium is far from being technologically achievable. More broadly, the fine-tuned dance characteristic of biochemical processes and cellular machinery are, in general, far too complex to be currently envisioned as feasible routes for producing many biomimics.

As such, a likely method for producing a biomimetic cilium combines the two foundations of engineered nanomaterials I mentioned earlier, engineered microstructure combined with a responsive, composite material. To mimic the size of the biological cilium and produce an array of such structures requires engineering processes capable of producing robust, responsive structures at a scale which has not been previously demonstrated in a man-made system. The constraints imposed by current fabrication techniques at this scale preclude any mimic with internal machinery, and so the material they are constructed from must combine the flexibility required to deform with the ability to respond to an external stimulus. As I will describe in detail, the first fundamental thrust of my thesis work was to develop a fabrication process which would reliably produce artificial cilia at the size of the biological cilium. Briefly, the strategy I have devised involves the template-based microfabrication of a polymer-magnetic nanoparticle composite material to form free-standing arrays of magnetically actuated cilia.

With the first artificial structures to mimic the size and function of biological cilia in hand, the second fundamental thrust of my thesis has been to use these structures as one of the first examples of a biomimic which can 'close the loop' in biomimetics research. In many cases, the subjects of biomimicry to this point have been those who can be poked, prodded, and looked at to a degree which makes them well understood both theoretically and technologically. For this reason, the biology of such systems

is often well understood and the biomimetics research is primarily application driven. In contrast, despite decades of theoretical and experimental work an amazing array of functions performed by cilia are just now being discovered, and the difficulties associated with both experimental and theoretical research have limited the understanding of cilia-driven hydrodynamics. As such, in this thesis I seek to develop an engineered cilia mimic which extends the bounds of state-of-the-art microfabrication and has potential for numerous practical applications, but also provides a highly controlled model platform for elucidating issues of fundamental importance to biological ciliated systems.

In large part, the inspiration for this second thrust is due to the association of this work, and much of the other work I have been exposed to throughout graduate school, under the broader umbrella of the University of North Carolina's Virtual Lung Project (VLP). The VLP is a highly multidisciplinary collaboration between University of North Carolina professors in applied mathematics, physics, chemistry, biology, and other fields, along with a number of medical doctors from the UNC Cystic Fibrosis Center. The broad goal of the Virtual Lung Project is to seek models of airway function and dysfunction with an accuracy that would allow for computational predictions on the efficacies of therapeutical and pharmacological treatments. This type of effort is part of an increasing trend across many aspects of human health to begin the modeling of biological systems which is on par with the modeling that has been used in engineering and manufacturing for decades. The development of biomimetic cilia is a very small part of the broader goals of the VLP, with the idea that these artificial mimics would provide an alternative with advantages over conventional experimentation with cell cultures and excised tissue.

1.1 Summary of the Thesis Work

The background work which is of relevance to this thesis is broad, but a unifying concept is the importance of fluid dynamics at the microscale. For this reason, before surveying the previous work in the literature I will first present an overview of several aspects of hydrodynamics at these scales in Chapter 2. At such small scales, fluids are inherently inertialess and thus a fascinating departure from much of our learned intuition about how fluids behave, and so a brief overview will provide a foundation for a deeper understanding of issues throughout the remainder of the thesis.

In Chapter 3, I will present a more detailed picture of the various fields to which my thesis work contributes. This includes further details on biomimicry, biological cilia, other types of responsive microstructures (some of which are competing versions of artificial cilia), and an introduction to microfluidics, a rapidly growing technology which requires novel strategies for control of fluids at the microscale. In the section on biological cilia, I will describe the state of knowledge on the structure and functions of biological cilia, especially the nature of experimental studies of cilia-driven fluid flows in these systems. This section focuses on two biological ciliated systems: those which line the airway epithelia in order to clear mucus and maintain airway sterility, and embryonic nodal cilia, which are a new and fascinating example of the increasingly widespread realization that fluid dynamics plays many critical roles in biology. I will describe how the large majority of studies of such systems have been very coarse, with little or no statistical analysis, largely owing to the difficulty of both *in vivo* and cell culture studies of ciliated systems. The consequent dearth of meaningful data on ciliated systems provides additional motivation for highly controlled fluid dynamics studies in a model of biological ciliated systems.

In Chapter 4, I begin the presentation of the fabrication processes used to generate robust biomimetic cilia arrays and the actuation of the arrays to mimic biological cilia.

Artificial cilia have been developed with responsiveness to a number of stimuli, but for a variety of reasons magnetic actuation has been a popular mechanism in other microactuators, for example because permanent magnets can be used which do not require their own power source. Our method combines a novel soft rubber-magnetic nanoparticle composite with a template based fabrication strategy that has previously been demonstrated only for rigid microstructures. Biological cilia are typically 250 nm in diameter and $3-7$ μm in length, and with this approach I have successfully produced arrays in the range of diameters from 200 nm to 1 μm and lengths of either 10 or 25 μm. The resulting free-standing structures have aspect ratios ($^{length}/_{height}$) of up to 125, which for their softness makes these structures one of the most flexible free-standing (and man-made) pillars of their scale in the published literature.

In the second part of Chapter 4 I move on to the actuation of these structures via permanent magnets. I demonstrate a number of strategies that have been developed to produce different beat shapes, several of which mimic the beat of airway and nodal cilia. This chapter includes a static model, developed by Ben Evans, a collaborating fellow graduate student, which was the first model in the literature to include the effect of a magnetic gradient. I will present experimental work which demonstrated for the first time the actuation of a flexible rod based on the forces generated magnetic field gradient, as opposed to the more typical case in which the bending force is generated by the direction and strength of the field itself, relative to the axis of the cilium. This experiment also served as confirmation of the accuracy of the model in its ability to predict such an effect, with potential applications as a magnetic switch. Broadly speaking, the efforts of Chapter 4 extend the presentation and discussion of results which were published as Evans and Shields et al., *Nano Letters*, vol. 7, no. 5, pg. 1428-1434 (2007).

Chapters 5 and 6 present my result and analysis of the fluid flows generated by the

actuation of the cilia arrays. I describe the general types of flows seen in the system, which include vortices around each cilium and an overall oscillation of the entire fluid volume which is at the frequency of the cilia beat. This oscillation generates 'epicycles' in the motion of particles in the fluid, the shape of which reflect the path of the cilia tips.

Many of the fluid flow results presented in these chapters revolve around my observation that in most cases the character of the fluid flow was dramatically different below the cilia tips than above, and that the transition between these two regimes occurs over a length of just a few microns. My analyses of these flow regimes provide some of the most thorough experimental characterizations of cilia-driven fluid flow, especially in the layer of fluid below the cilia tips, an area which is especially difficult to access experimentally in biological systems.

In Chapter 5 I demonstrate the first report in the literature of long-range pumping by an artificial cilia system. I show that the cilia can generate uniform, directional fluid flow by mimicking the beat shape of the class of cilia known as embryonic nodal cilia. With this specific beat shape, the flow above the cilia tips changes from the simple epicyclic oscillations just described to a superposition of the epicycles with an overall uniform background flow. I characterize this flow regime in terms of a canonical hydrodynamics problem, Poiseuille-Couette flow, and show that this model can also be applied to the flow in the biological system of the embryonic node.

In Chapter 6 I focus on the flow regime below the cilia tips, and I demonstrate that the nodal cilia beat can produce mixing in this regime which is dramatically different from the directional transport in the pumping regime. Furthermore, mixing in ciliated systems has not been demonstrated in any theoretical or experimental work, and so my characterization of these flows has biological implications which I will discuss. For example, the function of the biological nodal cilia system hinges on the ability of the

cilia to create a flow which establishes a chemical gradient, and so the possibility of cilia-driven mixing might have repercussions on the stability of such gradients. The results presented in Chapters 5 and 6 are an extension of work which was recently published as Shields et al., *The Proceedings of the National Academy of Sciences*, vol. 107, no. 36, pg15670-15675, 2010.

Chapter 2

MICROSCALE HYDRODYNAMICS

"Now, I'm going to talk about a world which, as physicists, we almost never think about. The physicist hears about viscosity in high school when he's repeating Millikan's oil drop experiment and he never hears about it again....And Reynolds number, of course, is something for the engineers. And the low *Reynolds number regime most engineers aren't even interested in... But I want to take you into the world of very low Reynolds number – a world which is inhabited by the overwhelming majority of the organisms in this room. This world is quite different from the one that we have developed our intuitions in."*

- E.M. Purcell, "Life at Low Reynolds Number",
from a classic talk given in honor of
Victor Weisskopf and reprinted as
Amer. J. of Phys., Vol. 45, No. 1, (1977).

A common theme throughout this thesis is the importance of fluidic phenomena, especially at the microscale. For this reason I present in this chapter an overview of a variety of such phenomena. Fluid dynamics is a fascinating field for many reasons. Although our everyday experience with fluids is vast, the number and types of problems which are fully understood on a theoretical basis are relatively few. As Purcell notes, at the microscale fluids often behave in ways which defy our intuition, and although

there are a number of simple problems in this realm which are easily solved, systems with only a small amount of complexity typically require computational methods. On the other hand, at the scale of our everyday world fluids are often turbulent, a state characterized by random fluctuations in velocity components which poses great computational challenges. Thus, fluid dynamics is a field which is fundamental to a vast array of systems across all scales, yet in many cases surprisingly little is understood about many fluidic problems.

The fluid dynamics problem specific to this thesis is the nature of the fluid flow around beating cilia. Cilia are microscale structures and operate within the nonintuitive regime Purcell is describing, and so a basic understanding of how fluids work at these scales will be critical to the remainder of this thesis. To develop this understanding I present and discuss the governing equations of fluid dynamics, the Navier-Stokes and continuity equations, as well as a number of canonical solutions. The models I will describe serve several purposes. They provide basic insights into hydrodynamics, and will also serve later in this work as simple models of the fluid flows driven by my biomimetic cilia.

The need for such simple models is primarily due to the sparsity of experimental data on fluid flows driven by biological cilia. A primary goal of many theoretical models is to predict the bulk fluid flow from knowledge of a the beat of a single cilium within the array, an idea known as coarse-graining. The lack of thorough experimental characterizations of fluid flows driven by biological cilia means that accurate coarse-graining descriptions will serve as a valuable tool for comparison with more sophisticated theoretical techniques.

2.1 Fluids at Low Reynolds Number

As Purcell noted, the fluid flow regime of interest is much different from our everyday experience. This non-intuitive regime is characterized by a low value of an important dimensionless number known as the Reynolds number. Hydrodynamics is replete with dimensionless ratios, which typically serve as measures of the relative importance of two competing phenomena and are thus an important description of what types of effects will dominate a system. The Reynolds number is a widely used dimensionless ratio which compares inertial and viscous effects, or

$$Re = \frac{\text{inertial forces}}{\text{viscous forces}}. \tag{2.1}$$

As Newton realized, inertia is the tendency of motion to persist in the absence of other forces. In contrast, viscosity is the resistance of a fluid to deformation, which works to dissipate motion and competes with inertia. In general, when $Re > 1$ then the motion of fluids begins to be dominated by their momentum. When $Re < 1$ viscous forces dominate inertia.

As the Reynolds number continues to decrease so that $Re << 1$, the 'low Reynolds number world' which Purcell helped to illuminate becomes dominant. This world is difficult for us to grasp because there is essentially no inertia, which means that objects defy our Newtonian perception that motion should persist. In our world, we set objects in motion (apply force) and expect them to go some distance after we let go (remove force). In the low Reynolds number world, as soon as we let go the object stops. Any forces from the past do not matter. Everything that matters at low Reynolds number is what is happening in the present.

Purcell noted that very few physicists or engineers were interested in low Reynolds number flows. To gain a sense of who *is* interested, the Reynolds number is typically

defined as

$$Re = \frac{\rho v \ell}{\eta} \tag{2.2}$$

where ρ is the fluid density, η is the dynamic viscosity, and v and ℓ are characteristic velocity and length scales of the system, respectively (Happel and Brenner, 1963). The properties of the fluid are sometimes combined into the kinematic viscosity $\nu = {}^{\eta}/_{\rho}$ so that the Reynolds number becomes

$$Re = \frac{v\ell}{\nu}. \tag{2.3}$$

If I choose the typical density and viscosity of aqueous solutions at room temperature of $\eta = 10^{-3}\ Pa \cdot s$ and $\rho = 10^{3}\ {}^{kg}/_{m^3}$, then the Reynolds number of such aqueous solutions is

$$Re = \frac{v\ell}{10^{-6}\ {}^{m^2}/_{s}}. \tag{2.4}$$

So in order to be interested in low Reynolds number you must have $v\ell << 10^{-6}\ {}^{m^2}/_{s}$. It is now clear that those interested in low Reynolds are those who are very small or move very slowly.

Of course, this is why Purcell noted that the vast majority of organisms in the room were interested. At the microscopic scale nearly everything happens at low Reynolds number. For example, at cellular scales of $\ell \approx 10\ \mu m = 10\ \times\ 10^{-6}\ m$, in order to move at a Reynolds number equal to 1 an object must move with a velocity of $10\ {}^{cm}/_{s}$! For a microorganism this would mean moving about 10,000 body lengths per second, a truly difficult task.

Since Purcell's time microbiology and nanotechnology have come to the forefront of their respective fields, and so now those of us interested in low Reynolds number are many more (although not, I suppose, as a percentage). The biological cilium clearly operates at low Reynolds number, as do nearly all microscale biomimics, and the field

of microfluidics is almost entirely within this regime as well. Purcell's main examples concerned the swimming of microorganisms, as swimming has been a classic example of how low *Re* fluids do not work like our intuition guides us. In addition, swimming is intimately tied to the ability to produce net fluid motion, as an organism which swims in free space would produce fluid transport if it were fixed in place. In the next section I turn to a more rigorous description of low Reynolds number fluid mechanics, but to end this section and place the reader firmly within this world, another Purcell quote about swimming at low Reynolds number is in order:

"It helps to imagine under what conditions a man would be swimming at, say, the same Reynolds number as his own sperm. Well, you put him in a swimming pool that is full of molasses, and then you forbid him to move any part of his body faster than $1\ ^{cm}/_{min}$*. Now imagine yourself in that condition: you're under the swimming pool in molasses, and now you can only move like the hands of a clock. If under those ground rules you are able to move a few meters in a couple of weeks, you may qualify as a low Reynolds number swimmer."*

2.2 The Continuity and Navier-Stokes Equations

A typical starting point for the theory of fluid mechanics from a continuum perspective is the conservation laws of mass and momentum. A mathematical statement of conservation of mass can be obtained by stating that, within a finite element of fluid fixed in space, the rate at which density changes is equal to the net rate at which mass enters the element divided by its volume. In vector form this is

$$\frac{\partial \rho}{\partial t} = -\nabla \cdot (\rho \vec{u}) \tag{2.5}$$

(Happel and Brenner, 1963). This statement also implies that the velocity field is continuous, which is why it is often called the continuity equation. Low Reynolds number liquids are assumed incompressible and constant density, and so the continuity equation becomes

$$\nabla \cdot \vec{u} = 0. \tag{2.6}$$

Conservation of momentum is a formulation of Newton's $\vec{F} = m\vec{a}$ as applied to a fluid element. A restatement of this law in terms of momentum is that the external force on a system is equal to the rate of change of momentum. For a fluid element, momentum can increase within the element as well as flow in and out through its surfaces. The external forces on the element are any fluid stresses which act upon the surface, as well as any body forces such as gravity. Written out, this statement of conservation of momentum is the Navier-Stokes equation in its most general form, adapted from (Happel and Brenner, 1963):

$$\underbrace{\frac{\partial(\rho\vec{u})}{\partial t}}_{\substack{\text{Rate of increase of} \\ \text{momentum per unit} \\ \text{volume}}} + \underbrace{\nabla \cdot (\rho\vec{u}\vec{u})}_{\substack{\text{Rate of momentum} \\ \text{transport by convection} \\ \text{through the surface, per} \\ \text{unit volume}}} = \underbrace{\nabla \cdot \mathbf{\Pi}}_{\substack{\text{Stresses on the} \\ \text{surface, per unit} \\ \text{volume}}} + \underbrace{\rho\vec{f}.}_{\substack{\text{External body force} \\ \text{on element, per unit} \\ \text{volume}}} \tag{2.7}$$

The combination of this equation, which forms a set of three equations for momentum conservation in each direction, with the continuity equation forms the basic governing equations of hydrodynamics. They form a set of four equations which can be solved simultaneously for the four unknowns of the scalar pressure field and the three velocity components.

As will become clear, the most important term for low Reynolds number flow is the divergence of the total stress tensor $\mathbf{\Pi}$. The stress tensor describes the forces which are distributed over the surfaces of the fluid element. These forces are proportional to the

deformation of the element as it flows, which can be separated into two tensors which describe the element's rotation and shear. The sum of these is called the deformation-rate tensor. However, to proceed from the deformation of the element to the stress tensor requires knowledge of the material itself called a constitutive equation.

By far the most common types of fluids encountered are those, like air and water, called Newtonian fluids. These fluids obey a number of postulates, which have been confirmed by experiment, that make them amenable to calculations. For this reason, the vast majority of this chapter concerns itself with such fluids. However, in several ciliated systems, and biology in general, another common class of fluids which play important roles are viscoelastic fluids. As the name implies, the deformation of such materials causes them to store energy just as in a stretched rubber band. Such non-Newtonian behavior which makes theoretical treatments substantially more difficult, and very few theoretical models on cilia-driven fluid flow have incorporated viscoelasticity, as I will describe in more detail in Chapter 3.

Newton's observations of the fluids which bear his name revealed their defining characteristic, which is one of two postulates needed to pick a constitutive equation for the stress tensor $\mathbf{\Pi}$. Namely, Newton hypothesized in his *Principia* that, "The lack of slipperiness of the parts of a fluid is, other things being equal, proportional to the velocity with which the parts of the fluid are separated from one another" (Newton, 1687). This means that the shear stress in a fluid, the portion of the total stress which is applied parallel to the surfaces of a fluid element, is proportional by some constant to the velocity gradient perpendicular to the direction of the shear. The proportionality constant in this relationship is the definition of the viscosity of a fluid. For a fluid element under flow, the velocity gradients are elements of the deformation-rate tensor I described above. Thus, the first postulate for a Newtonian fluid is that the viscous stress is a linear function of the deformation-rate tensor.

The second postulate needed for the constitutive equation is that when the fluid element is at rest, the only stress on it is hydrostatic pressure. As opposed to shear stresses, such hydrostatic pressures are exerted perpendicular to the surfaces of the element. This means that the stress tensor for a Newtonian fluid can be separated into terms which independently describe the pressure and shear stress. The constitutive equation for a Newtonian fluid also requires two additional postulates, that the material be isotropic and that a pure rotation of an element does not induce any shear stresses. Finally, the derivation of the constitutive equation also utilizes the form of the continuity equation for an incompressible fluid (equation 2.6) and the assumption of constant viscosity to arrive at

$$\mathbf{\Pi} = -\nabla p + \eta \nabla^2 \vec{u} \tag{2.8}$$

(Happel and Brenner, 1963).

Thus, in a Newtonian, incompressible fluid, the Navier-Stokes equation (2.7) can be simplified to the form first derived by Navier (Navier, 1827)

$$\rho \left(\frac{\partial \vec{u}}{\partial t} + \vec{u} \cdot \nabla \vec{u} \right) = -\nabla p + \eta \nabla^2 \vec{u} + \rho \vec{F}. \tag{2.9}$$

This simplified form is the starting point for understanding a great number of fluidic problems. However, the second term on the left ($\vec{u} \cdot \nabla \vec{u}$), which represents convective acceleration of the fluid (for example, as the fluid goes around an obstacle), is quadratic in velocity and makes the equations non-linear, and thus substantially more difficult to solve. In a number of the canonical solutions I will present, this term is zero, the reason why they can be easily solved is that this term is identically zero to the geometry of the problem. When this is not the case, additional assumptions can provide further simplifications.

The first of these assumptions, which will apply in some cases but not all, is that $\partial\vec{u}/\partial t$ is small or zero, known as steady flow, meaning that the velocity field does not change in time. This eliminates the first term on the left, yet the troublesome non-linear term is still present. To arrive at the second assumption, it will prove interesting to simply compare dimensionally the two terms $\rho\vec{u}\cdot\nabla\vec{u}$ and $\eta\nabla^2\vec{u}$, based on characteristic lengths and velocities of the system. The dimensions of the first would be given by $\rho v^2/\ell$, while the second is $\eta v/\ell$. The ratio of these two, of course, brings us back to the Reynolds number $Re = \rho v\ell/\eta$. This reveals that the non-linear term in the Navier-Stokes equation represents inertial effects, while the Laplacian of the velocity field describes viscous effects. Thus, the assumption of low Reynolds number allows for the elimination of the non-linear term. It also explains why I stated earlier that the divergence of the stress tensor is the most important term of Navier-Stokes for low Reynolds number flows, which are also often referred to as viscous flows.

If I further assume that the effects of any body forces are negligible (gravity, at least, is rarely a significant force at the microscale), then the Navier-Stokes equation reduces to the form

$$\nabla^2\vec{u} = \frac{1}{\eta}\nabla p. \tag{2.10}$$

The combination of this result with the continuity equation ($\nabla\cdot\vec{u} = 0$) and the boundary conditions of the problem form the equations of motion for slow, viscous flow known as Stokes flow, or creeping flow.

It is important to note that the Stokes equations represent a significant simplification as they are now linearized. This is important because the solutions of linear differential equations obey the principle of superposition, which means that if (f_1, p_1) and (f_2, p_2) are separate solutions, then ($f_1 + f_2$, $p_1 + p_2$) is also a solution. Thus, for low Reynolds number flow, exact solutions to more complicated systems can be built from superpositions of the solutions to simple systems. However, the individual

systems which are superposed must share the same boundary conditions.

Such superpositions will be of relevance for the fluid flows described in Chapter 5, and I will discuss several below. In addition, many theoretical techniques used for cilia studies, such as slender body theory, rely on superposition techniques. These theories are summarized below as well, but first I present several of the canonical solutions to the Navier-Stokes equations.

2.3 Exact Solutions of the Navier-Stokes Equations

I have mentioned that the inertial term in the Navier-Stokes equations can be ignored at low Reynolds number in general, but there are a few canonical solutions of these equations which can be solved exactly without assuming low Reynolds number. In many cases these problems are simple geometries in which, at all points, the velocity vector is perpendicular to its gradient, and the inertial term $\vec{u} \cdot \nabla \vec{u}$ is identically zero. Each of the classes of solutions I will discuss in this section, Couette flow, Poiseuille flow, and Stokes 1st and 2nd problems, give examples of such scenarios where Navier-Stokes may be solved exactly. Despite the simple geometries, these solutions have been shown to be useful approximations of fluid flows in a wide array of systems, and thus widely applicable. More pertinently, in this thesis each will be of use as a model for various aspects of the fluid flows driven by biomimetic cilia arrays.

2.3.1 Couette Flow

Couette flow describes the flow of fluid between two boundaries in which the fluid is driven by the motion of the boundaries. In plane Couette flow the boundaries are two parallel plates with a lateral extent much larger than their separation h. One of the boundaries is translated in a direction parallel to the planes, and so it is assumed that

all the flow is along the same dimension, call it the x direction. The velocity profile between the plates $u(y)$ is then only a function of y. As the velocity is everywhere in the direction of x, but only a function of y, the inertial term is zero and the continuity equation is automatically satisfied. In addition, there is no pressure gradient and so the Navier-Stokes equations reduce to a single differential equation.

If I assume that the top plate translates with speed u_0 and the bottom plate is stationary then the flow is the solution of the Stokes equations with boundary conditions $u(0) = 0$ and $u(h) = u_0$. The pressure gradient is zero, and so the Stokes equations reduce to

$$\frac{\partial^2 u}{\partial y^2} = 0 \tag{2.11}$$

and so

$$u(y) = C_1 y + C_2 \tag{2.12}$$

where C_1 and C_2 are constants. With the boundary conditions this gives the velocity profile of plane Couette flow as

$$\boxed{u(y) = \frac{u_0}{h} y,} \tag{2.13}$$

so the velocity profile is simply linear between the boundaries, as shown in Figure 2.1. This solution also possesses the unique quality of a constant shear stress over the entire height, which is given by $\tau = \eta \, {}^{\partial u}/_{\partial y} = {}^{u_0}/_{h}$. This solution has many practical applications and is relevant to the case of ciliated systems, as, even though they often line cylindrical ducts, the curvature of the ducts is usually large compared to the cilia and so the cilia effectively act as if they are distributed on a flat plane.

2.4 Poiseuille Flow

While in Couette flow the motion of the boundaries drives the fluid, in this second example, Poiseuille flow (pronounced *pwah-zwee*), the fluid motion is pressure-driven. In plane Poiseuille flow, the geometry is the same infinite plates as plane Couette flow, but in this case both boundaries are stationary. The boundary conditions are then $u(0) = u(h) = 0$, and as in plane Couette flow the velocity is entirely in the x direction and only a function of y, and so the Stokes equation is given by

$$\frac{\partial^2 \vec{u}}{\partial y^2} = \frac{\nabla p}{\eta}. \tag{2.14}$$

The solution of this is obtained by double integration, and using the boundary conditions to solve for the constants of integration, which gives

$$u(y) = -\frac{\nabla p}{\eta}\left(\frac{y^2}{2} + Ay + B\right), \quad B = 0, \quad A = -\frac{h}{2}. \tag{2.15}$$

Thus, the velocity profile of Poiseuille flow is a parabola given by

$$\boxed{u(y) = -\frac{\nabla p}{2\eta}(y^2 - hy).} \tag{2.16}$$

The maximum velocity is halfway between the plates at $y = {}^{h}/_{2}$ and is given by

$$u_{max} = \frac{\nabla p}{8\eta}h^2 \tag{2.17}$$

while the average flow speed is obtained by integrating the profile and dividing by the separation

$$u_{avg} = \frac{\nabla p}{12\eta}h^2 = \frac{2}{3}u_{max}. \tag{2.18}$$

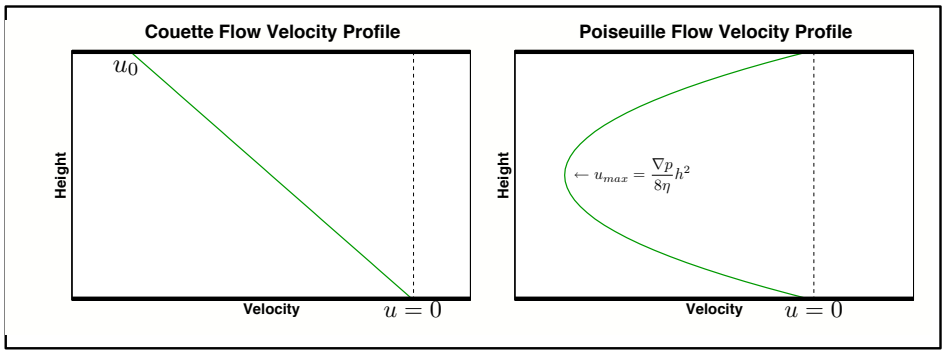

Figure 2.1: Click to Animate. The poster image and animations represent the velocity fields of Couette flow, which is driven by the motion of the upper boundary, and Poiseuille flow, which is driven by an external pressure gradient.

This last result is of some use because the volume flow rate through a channel of arbitrary cross-sectional area A is given by $Q = u_{avg}A$. Finally, the shear stress is

$$\tau = \nabla p \left(y - \frac{h}{2} \right), \tag{2.19}$$

a linear function which is zero at the midpoint and has extrema at the boundaries. This reveals a general aspect of viscous flows, which is that the relative motion of fluid and a boundary induces shear stresses which are largest near the boundary. This is because the viscosity of the fluid tries to smear out any velocity gradients, and such gradients are typically largest in proximity to boundaries.

A quick comparison between the plane Couette flow result and this result for plane Poiseuille flow is of some interest because it speaks to another broad principle of low Reynolds number flow. In Couette flow, the boundaries drive the flow and the velocity is *independent* of the fluid properties. In contrast, for pressure-driven flows the velocity does depend on the viscosity. The situation is reversed for the shear-stresses experienced by the fluid: the shear stress in the boundary-driven flow depends on viscosity due to the viscosities tendency to smooth velocity gradients, while in Poiseuille flow the shear stress only depends on the pressure.

2.5 Stokes 1st and 2nd Problems

2.5.1 Stokes 1st problem

The fluid dynamics problems known as Stokes 1st and 2nd problems also have many applications in engineering and physics. They share a common geometry and are both exact solutions of Navier-Stokes, but differ in their boundary conditions. The geometry in Stokes 1st problem is the semi-infinite space defined by a single infinite plane with a fluid above it. In Stokes 1st problem the plane and the fluid are initially at rest, but at time $t = 0$ the plane instantaneously begins translating at speed U. In Stokes 2nd problem the plane oscillates in time rather than moving with a constant velocity. Each problem introduces time, and so the assumption of a steady flow does not apply, but exact solutions may still be found owing to the simplicity of the geometry. Specifically, as the plane only moves in the x direction it can be assumed that the fluid velocity is also in x and only a function of y. There are also no pressure gradients, and so for both problems the Navier-Stokes equation reduces to

$$\frac{\partial u}{\partial t} = \nu \frac{\partial^2 u}{\partial y^2} \tag{2.20}$$

where I have again used the kinematic viscosity $\nu = \eta/\rho$. The solution to Stokes 1st problem is obtained from the boundary condition

$$u(0,t) = \begin{cases} 0, & \text{for } t \leq 0 \\ U, & \text{for } t > 0. \end{cases} \tag{2.21}$$

This can be solved exactly by similarity methods, but as Stokes 2nd problem is of much more relevance to the discussion, I will just give the solution to Stokes 1st problem, which is

$$u(y,t) = U\left(1 - \operatorname{erf}\left(\frac{y}{2\sqrt{\nu t}}\right)\right) \tag{2.22}$$

where erf is the error function. An interesting application of this result is to ask about what thickness of fluid above the plane is moving after a given time, which could be called the penetration depth of the plane's disturbance. To arrive at a clean result, a common observation is that the fluid velocity is about 4% of the plane's velocity when the argument of the error function is equal to $3/2$. If the penetration depth is δ, then $3/2 = \delta/(2\sqrt{\nu t})$, or

$$\delta = 3\sqrt{\nu t}. \tag{2.23}$$

It is worth noting that thisd result shares a similarity with the phenomenon of diffusion. Diffusion refers to the motion of small particles in a fluid, which exhibit 'random walks' due to molecular collisions. While I will discuss diffusion in more depth in Chapter 6, the penetration depth has the same form as the expected root-mean-square displacement of diffusive particles as a function of time, which also goes as $\sqrt{t}$. For this reason, the kinematic viscosity is analogous to the rate of diffusion of a particle, known as the diffusivity, which is a property of the particle just as ν describes the basic properties of the fluid. This is why the kinematic viscosity is sometimes conceptually thought of as a measure of the rate at which momentum 'diffuses' into a fluid.

2.5.2 Stokes 2nd problem

The boundary condition on Stokes 2nd problem is an oscillation of the plane described by

$$u(0,t) = U\ cos\ \omega t \tag{2.24}$$

where ω is the frequency of the oscillation and it is assumed that each fluid element oscillates with the same frequency in a plane parallel to the floor. The solution can

then be assumed to have the form

$$u(y,t) = \mathrm{Re}\left[X(y)e^{i\omega t}\right] \tag{2.25}$$

where Re signifies the real part of the complex expression, and X(y) is the amplitude of the fluid oscillation as a function of distance from the plane. Substituting this into the differential equation gives

$$\mathrm{Re}\left[i\omega X(y)e^{i\omega t}\right] = \nu \mathrm{Re}\left[\frac{d^2X}{dy^2}e^{i\omega t}\right] \tag{2.26}$$

which can be simplified to give the 2nd order, homogenous differential equation for the amplitude

$$\frac{d^2X}{dy^2} - i\frac{\omega}{\nu}X = 0. \tag{2.27}$$

Differential equations of this form, in which the second derivative of a function is equal to some constant times the function itself, can be solved by assuming the solution

$$X(y) = c_1 e^{-c_2 y} + c_3 e^{c_4 y}. \tag{2.28}$$

where c_1 and c_3 are determined by boundary conditions, and c_2 and c_4 are roots of the characteristic form of the differential equation. An additional boundary condition on this problem which I have not yet mentioned is that the fluid velocity must remain finite as $y \to \infty$. This is not the case in the second term of the assumed solution (the positive exponential), and so I must have $c_3 = 0$. Substituting the rest of the assumed solution back into the differential equation gives

$$\frac{d^2X}{dy^2} = c_1 c_2^2 e^{-c_2 y} \tag{2.29}$$

and so comparison with the original differential equation means that I must have $c_2 = \sqrt{i\omega/\nu}$. Before substituting this back in, I first note that I am eventually going to need to select the real part of the solution. Thus it will be helpful to note that, if I assume $a + ib = \sqrt{i}$, square both sides, and equate the real and imaginary parts then $\sqrt{i} = (1+i)/\sqrt{2}$.

The amplitude of the fluid's oscillation is then given by

$$X(y) = c_1 e^{-(1+i)\sqrt{\frac{\omega}{2\nu}}y} \tag{2.30}$$

or

$$X(y) = c_1 e^{-\sqrt{\frac{\omega}{2\nu}}y} e^{-i\sqrt{\frac{\omega}{2\nu}}}. \tag{2.31}$$

Substituting back into equation 2.25 gives for the velocity profile

$$u(y,t) = \mathrm{Re}\left[c_1 e^{-\sqrt{\frac{\omega}{2\nu}}y} e^{-i\sqrt{\frac{\omega}{2\nu}}y} e^{i\omega t}\right] \tag{2.32}$$

or

$$u(y,t) = \mathrm{Re}\left[c_1 e^{-\sqrt{\frac{\omega}{2\nu}}y} e^{i\left(\omega t - \sqrt{\frac{\omega}{2\nu}}y\right)}\right]. \tag{2.33}$$

To take only the real part of the expression I use Euler's formula,
$re^{i\theta} = r(cos\theta + isin\theta)$, and so

$$u(y,t) = c_1 e^{-\sqrt{\frac{\omega}{2\nu}}y} cos\left(\omega t - \sqrt{\frac{\omega}{2\nu}}y\right). \tag{2.34}$$

Finally, the last constant is obtained with the boundary condition at the plane,
$u(0,t) = U\ cos\ nt$, which simply gives $c_1 = U$, and so the velocity profile of Stokes 2nd problem is

$$\boxed{u(y,t) = U\ e^{-\sqrt{\frac{\omega}{2\nu}}y} cos\left(\omega t - \sqrt{\frac{\omega}{2\nu}}y\right).} \tag{2.35}$$

This result describes a velocity which oscillates in time just as expected, with an amplitude which is largest at the plane and decays exponentially as y increases. The phase shift between the plane's motion and the fluid is also a function of y and depends on the properties of the fluid and the oscillation frequency.

Again I can ask about the thickness of the layer which is affected by the plane's motion. At a given plane, the maximum motion is when the cosine term is 1, and another definition of the penetration depth is that it is the height at which the velocity is decreased by a factor of $1/e^2$. With these two conditions the velocity profile gives

$$\frac{1}{e^2} = e^{-\sqrt{\frac{\omega}{2\nu}}\delta} \tag{2.36}$$

and so the penetration depth is

$$\delta = 2\sqrt{\frac{2\nu}{\omega}}. \tag{2.37}$$

This result is also proportional to $\sqrt{\nu}$, as in Stokes 1st problem, but offers the additional insight that the layer thickness is inversely proportional to the square root of the plane's oscillation frequency. Thus, when the frequency of a given oscillatory motion is increased the thickness of the layer which is influenced decreases, while increasing the viscosity of the fluid increases the coupling between the fluid and the boundary and increases the penetration depth.

2.5.3 Modified Stokes 2nd problem

Stokes 2nd problem can be modified for the presence of an upper boundary at $y = h$. The differential equation does not change, only the boundary condition. Whereas in the assumed form of the amplitude in the semi-infinite fluid I was able to eliminate the positive exponential, in this case that cannot be done and so the amplitude is given by a hyperbolic sine function. Interestingly, although this is another exact solution

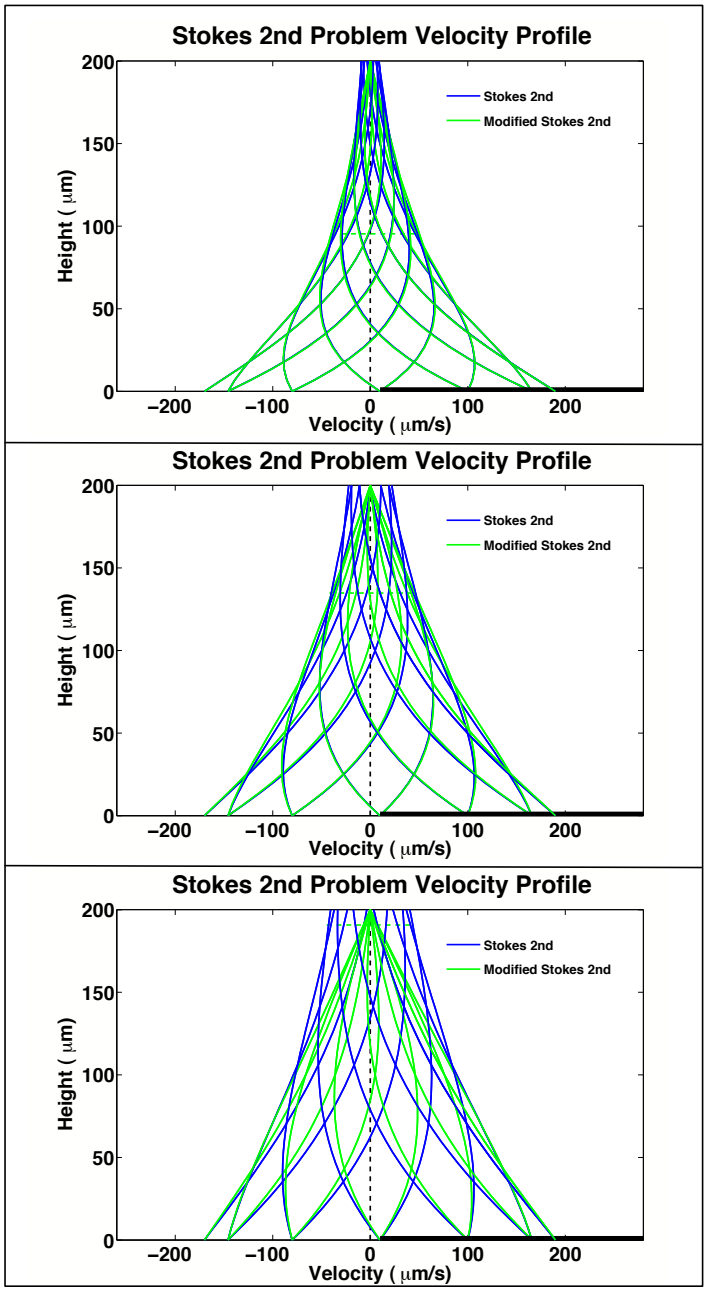

Figure 2.2: Click to Animate. A comparison of Stokes 2nd problem, with no upper boundary (eq. 2.35), and the modified form with an upper boundary (eq. 2.38). In modified Stokes 2nd problem the fluid is fixed at the upper boundary, but the discrepancy between the solutions is only significant if the penetration depth is sufficiently large. In the top panel the viscosity of the fluid is set to some value η, the middle panel is 2η, and the bottom is 4η. This demonstrates the effect of the viscosity, which is to increase the coupling between the fluid and any boundaries, increasing the penetration depth and the discrepancy between the solutions.

of Navier-Stokes and easily derived, the solution appears to only recently have been written down in the literature (Mitran et al., 2008). For the plane which is oscillating with velocity $U\ cos\ \omega t$, the velocity profile is given by

$$u(y,t) = \mathrm{Re}\left[U e^{i\omega t} \frac{sinh\left[\frac{\delta_0}{A}(h-y)\right]}{sinh\left[\frac{\delta_0 h}{A}\right]} \right] \tag{2.38}$$

where I have introduced the parameters $A = {}^{U}/_{\omega}$ and $\delta_0 = (1+i)\sqrt{{}^{\omega}/_{2\nu}}$. For this solution, the real part of δ_0 is related to the penetration depth of the plane's influence.

2.6 Relevant Superpositions of Exact Solutions

Each of the problems derived above share the fact that the differential equations to be solved were linear. As I have mentioned, this is important because it means that the solution to problems which can be deconstructed into two or more of these simple problems is just the sum of the individual solutions. Several such superpositional solutions form simple models which will be of use in describing cilia-driven flows in my system, and so I will briefly mention those here.

2.6.1 Poiseuille-Couette flow

This type of flow is in the same geometry as plane Poiseuille and plane Couette flow, parallel plates with a separation h, and combines the boundary conditions of Couette flow with the pressure gradient of Poiseuille flow. Although I previously derived Couette flow (equation 2.13) with the moving boundary at the top, it will be of more relevance to my discussion to have the moving boundary be at the bottom. This is accomplished with the simple transformation $y \rightarrow h - y$, which leaves Poiseuille flow the same because it is symmetric about the midpoint separation. The solution of the combined flows is

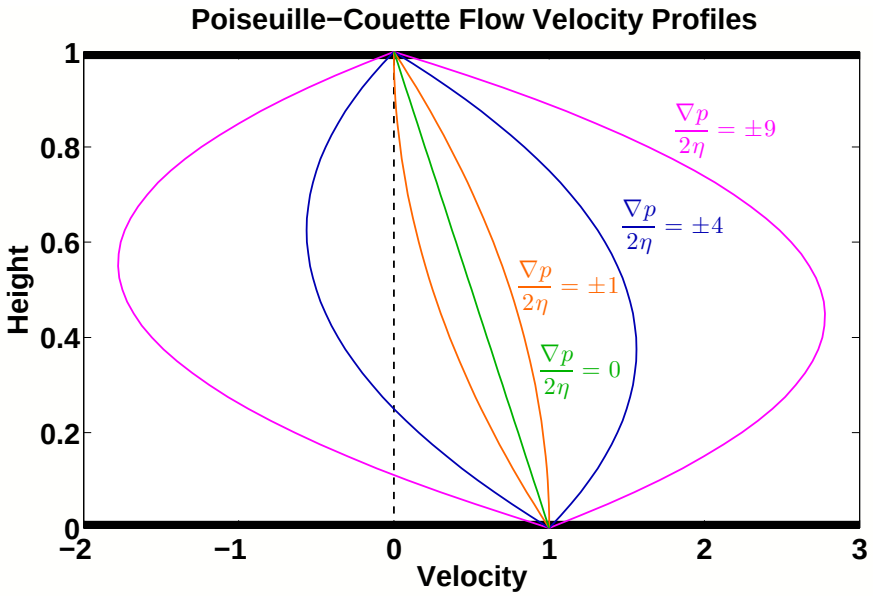

Figure 2.3: Family of velocity profiles of Poiseuille-Couette flow, equation 2.39, with various pressure gradients. The velocity of the sliding plane (the floor) is set to $u_0 = 1$ and the height is $h = 1$.

then called Poiseuille-Couette flow, or also general Couette flow, and given by

$$\boxed{u(y) = \frac{u_0}{h}(h - y) + \frac{\nabla p}{2\eta}\left(y^2 - hy\right).} \tag{2.39}$$

A family of these velocity profiles is shown in Figure 2.3 for a given plane velocity u_0 and a number of different pressure gradients ∇p.

In many situations of relevance the pressure gradient drives flow in the direction opposite of the flow driven by the boundary. In this case, the net flow rate can be in either direction, as suggested by the set of curves plotted in Figure 2.3.

Driven cavity flow

Poiseuille-Couette flow will be of relevance in Chapter 5, but is also applicable to a number of industrial systems as the limiting solution for the flow in a 'driven cavity'. The geometry is a completely enclosed cavity with height h, width w, and length l.

Just as in Couette flow, the top or bottom boundary is translated along the length of the cavity, and the major feature is a large rotational flow. The fluid near the translating boundary is dragged by the plane's motion, then encounters one of the end walls and is forced to recirculate around the boundary opposite the translating boundary. The problem has been widely used as a computational benchmark because, at a well-known Reynolds number, counter vortices begin to develop in the corners of the cavity (Bye, 1966; Koseff and Street, 1984). Of most relevance to the later discussion is that Poiseuille-Couette flow is the velocity profile of a driven cavity in the limiting case where the length and width of the cavity are much larger than its height (Albensoeder et al., 2001).

2.6.2 Modified Stokes 2nd problem plus Couette flow

Another example of a superposition of two exact solutions which will be of use in Chapter 5 is a combination of modified Stokes 2nd problem with Couette flow. This describes a geometry in which the lower boundary is translated at a constant velocity, but with an oscillatory motion superimposed onto the constant velocity motion. Again, the solution is just the sum of equations 2.38 and 2.13. In this case, however, it will be useful to further generalize this problem so that the oscillatory motion is in both dimensions within the plane such that the plane exhibits a circular oscillation. In terms of the coordinates I have been using, the plane translates in x with constant velocity u_0, and oscillates in y and z with a given frequency ω, a maximum velocity U in each direction, and a phase shift between y and z of $\pi/2$. For a velocity given by

$u(y,t) = u_x\hat{x} + u_z\hat{z}$, the solution of Navier-Stokes with these boundary conditions is

$$u_x(y,t) = \text{Re}\left[Ue^{i\omega t}\frac{sinh\left[\frac{\delta_0}{A}(h-y)\right]}{sinh\left[\frac{\delta_0 h}{A}\right]}\right] + \frac{u_0}{h}(h-y),$$
$$u_z(y,t) = \text{Re}\left[Ue^{i(\omega t-\pi/2)}\frac{sinh\left[\frac{\delta_0}{A}(h-y)\right]}{sinh\left[\frac{\delta_0 h}{A}\right]}\right]. \tag{2.40}$$

The fluid motion in this problem is what I will define as 'epicyclic transport' in Chapter 5, the combination of oscillatory movement with an overall constant velocity which is reminiscent of the planetary epicycles hypothesized within the Aristotelian model of the solar system. Such epicycles have also been observed in theoretical and experimental studies of the low Reynolds number flow driven by a single rotating rod (Bouzarth et al., 2007).

The velocity profiles of this superposition are depicted in Figure 2.4. These also serve as good visualizations of the flow in Stokes 2nd problem in general, as it is easy to envision the velocity profile without the offset produced by the Couette model. In addition, the penetration layer derived as equation 2.37 can be visually compared for two frequencies an order of magnitude different.

To foreshadow the epicyclic transport I will present for cilia-driven flow, I present in Figure 2.5 the displacement of a fluid element along the direction of the Couette boundary, at a given height, for the solutions 2.40, as well as the trajectory of the fluid element in the $x-z$ plane.

2.7 Approximation Methods

Although I have introduced the Stokes equations, the form the Navier-Stokes equations take at low Reynolds number, each of the examples I provided in the previous section were exact solutions of the full Navier-Stokes equations. In this section I briefly

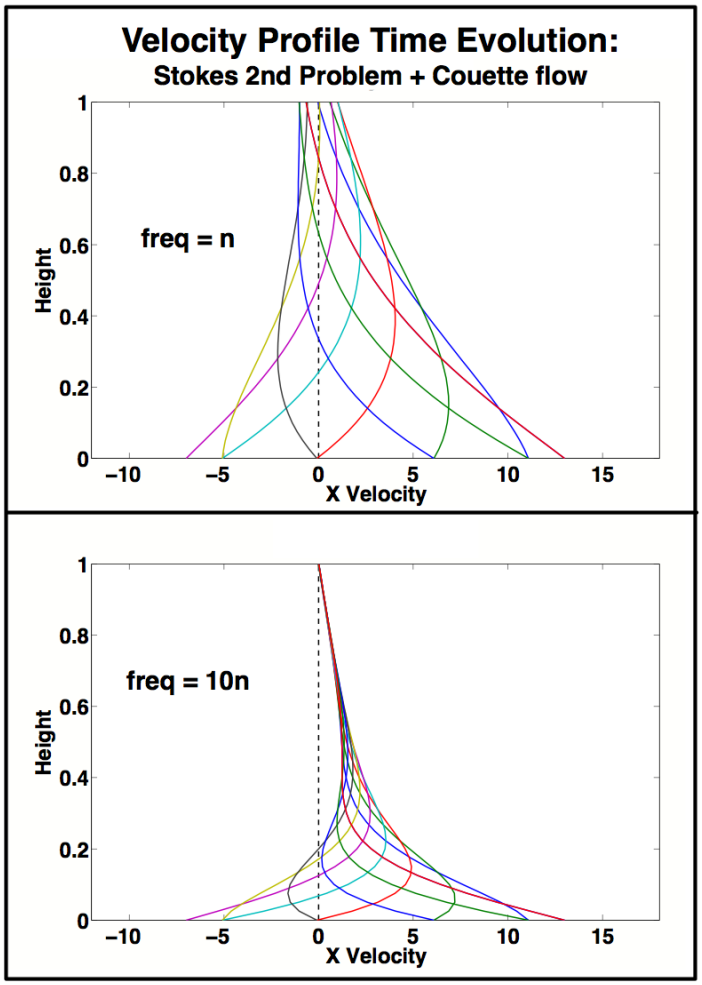

Figure 2.4: Click to Animate. The velocity profile of Stokes 2nd problem superposed with Couette flow. The constant velocity of the sliding plane offsets the oscillatory motion so it is not about zero. The two panels compare oscillations of different frequencies, demonstrating the decreased penetration depth into the fluid as the frequency is increased. Note that, for the animation, the frequency in the bottom panel *is* higher, but the motion is slowed down to correspond to the low frequency oscillation.

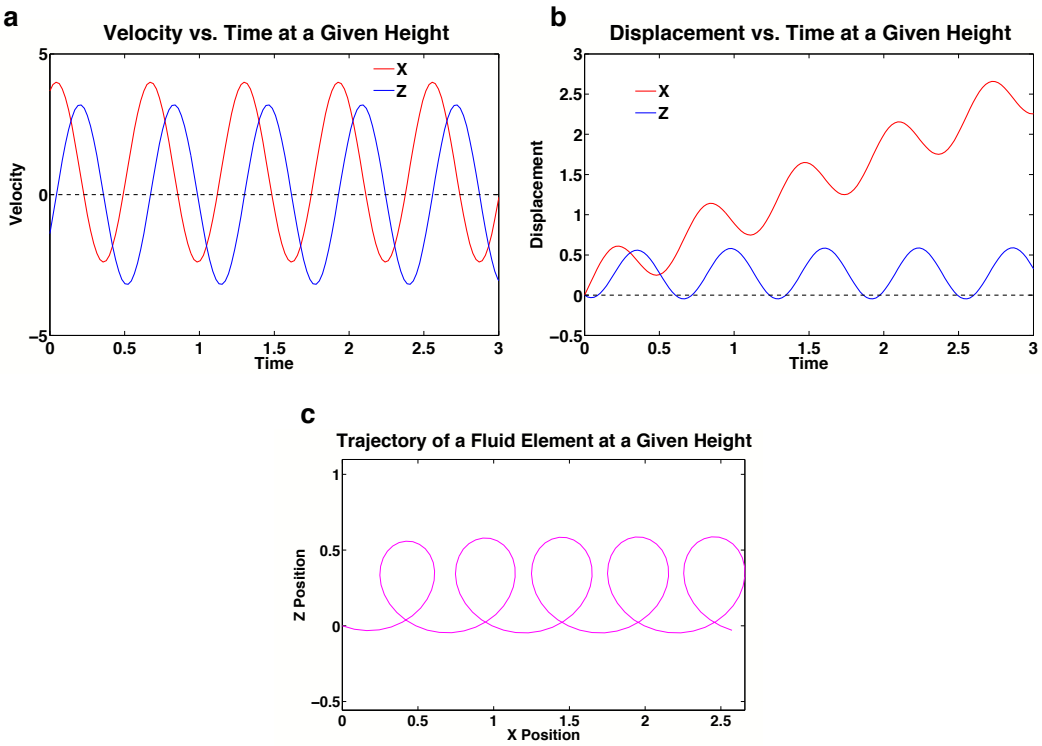

Figure 2.5: Epicyclic transport of a fluid element in a model of the velocity profile of Stokes 2nd problem superposed with Couette flow. The plane oscillates in x and z with the same frequency and amplitude, but a $\pi/2$ phase shift so that the oscillation is circular. The plane also moves with a constant velocity in x as in Couette flow. At a given height y, the time-dependent motion of the fluid is a superposition of the damped oscillation from Stokes 2nd problem with the constant velocity of Couette flow, which I will define in Chapter 5 to be epicyclic transport.

outline methods which do utilize the low Reynolds number assumption to arrive at approximate solutions to Navier-Stokes. More specifically, a reformulation of Navier-Stokes into dimensionless parameters reveals that the Reynolds number naturally arises as a coefficient to the inertial term. Thus, the Stokes equations can be arrived at mathematically by taking the limit as $Re \to 0$.

In the following subsections I will review a few basic solutions which will be of relevance later as they are the building blocks for many theoretical studies of cilia-driven flow. These solutions borrow from ideal-fluid flow, the area of fluid mechanics which considers fluids which do not have a viscous component. If such flows are irrotational, then they can be described by a velocity potential ϕ, an analogous entity to the electric potential in electrostatics. While in two-dimensions potential flows can be easily described by a stream function, in three-dimensions analytical solutions are restricted to axisymmetric geometries. When this is the case, the velocity potential can be found by separation of variables as a solution to Laplace's equation $\nabla^2\phi = 0$. Flow fields for fundamental structures can be found in this manner, such as for sources and sinks, as well as doublets, the fluid mechanical analogue to the electric dipole, which is formed from a source and sink of equal strength with an infinitesimal separation. For the problems presented in this section I will not derive the solutions for the sake of brevity, but I note that they are obtained by borrowing the solutions for the velocity potential by finding a different physical quantity, such as the pressure, which is a scalar field that also satisfies the Laplacian (Happel and Brenner, 1963).

2.7.1 Stokeslets and rotlets

The approximation schemes widely used for cilia models involve the fundamental representations of a point force and a point torque on the fluid. These singularities are referred to, respectively, as a Stokeslet and a rotlet. The Stokeslet is obtained by

considering the scalar pressure field represented by the doublet solution. If the form of the pressure field is taken to be $p = 2c\eta\,({}^{x}/_{r^3})$, then the velocity field produced by a Stokeslet is

$$\vec{u} = c\left(\frac{x}{r^2}\hat{r} + \frac{1}{r}\hat{x}\right). \tag{2.41}$$

While the velocity field has radial components, these decay faster than the velocity in the x direction, and so the far-field flow is a uniform flow along x. In addition, the force on the fluid generated by the Stokeslet is also in x and given by

$$\vec{F} = 8\pi c\eta\hat{x}. \tag{2.42}$$

Whereas the Stokeslet is the fundamental generator of force in a fluid, the solution for a rotlet is a singularity which generates zero net force, but does produce a net torque. It is obtained by considering a rotational flow solution of the form $\vec{u} = \vec{r} \times \nabla\chi$. In this case, χ forms a scalar field which satisfies the three-dimensional Laplacian. Again taking the doublet solution the velocity field for a rotlet is obtained as

$$\vec{u} = B\vec{r}x\left(\frac{1}{r^3}\hat{x} - 3\frac{x}{r^4}\hat{r}\right) \tag{2.43}$$

and the torque exerted on the fluid is

$$\vec{M} = 8\pi B\eta\hat{x}. \tag{2.44}$$

The torque generated on the fluid produces streamlines which form concentric circles on the origin.

2.7.2 Slender body theory

Many of the most widely used modeling strategies for cilia-induced flow utilize slender-body theory. A slender body is defined as one with a large aspect ratio, or $\ell \gg R$. For suitably slender bodies, it is assumed that the influence of the body's motion on the fluid can be described by a line distribution of Stokeslets (equation 2.41). The geometry of the problem is that a slender body of length 2ℓ sits along the x_1-axis such that the Stokeslets are distributed over $-\ell < x < \ell$. Using Batchelor's notation, for a body whose position is given by $\vec{x}'$ and the line density of applied force is $\vec{F}(x')$, the velocity at a point $\vec{x}$ is

$$u_i(\vec{x}) = \frac{1}{8\pi\eta} \int_{-\ell}^{\ell} \left[\frac{F_i(x')}{((x-x')^2 + r^2)^{\frac{1}{2}}} + \frac{(x_i - x_i')(x_j - x_j')F_j(x')}{((x-x')^2 + r^2)^{\frac{3}{2}}} \right] dx' \tag{2.45}$$

where $r^2 = x_2^2 + x_3^2$ (Batchelor, 1970). If the slender body is in motion, and the fluid is constrained by no-slip at the body's surface, then this equation cannot be solved directly. Instead, asymptotic solutions are obtained by taking the limit $R/\ell \to 0$.

For ciliated systems the necessary presence of a boundary (the cell floor) further complicates the theory. Following Batchelor's work, Blake constructed a solution in the presence of a no-slip plane, which used the method of images to to ensure zero velocity at the floor (Blake, 1970). This image system involved the Stokeslets presented above, but also higher-order derivatives which improve the accuracy of the approximation. This slender body theory for a cilium in the presence of a boundary was the foundation for the majority of theoretical cilia studies which continue to this day.

Chapter 3

PREVIOUS WORK

The two fundamental thrusts I defined in the Introduction require that this research be highly interdisciplinary in nature. As I mentioned, although a number of publications have demonstrated the fabrication of competing versions of artificial cilia, typically at larger scales, in all cases the broader context in which the works are presented is entirely technology oriented. Simply put, this is due to the fact that no other artificial cilia system mimics the size and function of biological cilia to any great degree. Many of these competitors have demonstrated amazing technological achievements, but their work cannot be placed into a biological context. This provides a specific example of my earlier claim that biomimetics research has been effectively a one-way street, in which technology is improved by biological inspiration, but biology gains little in return.

In contrast, the development of the biomimetic cilia arrays presented in this work provide an opportunity to significantly address issues of relevance to a broad spectrum of fields. In this chapter I present relevant work from the literature which encompasses technical areas such as nanotechnology and microfluidics, but also delves into cellular and developmental biology. The presentation of this diversity of previous work will hopefully improve the reader's comprehension and appreciation for the results presented in the subsequent chapters.

Biomimetics is the field that unites technology with biology, and so I begin my

survey of previously published work with a few notable examples of biomimicry which share similarities with my biomimetic cilia arrays. These examples also provide a brief context in which to envision some of the other potential applications of responsive microscale structures like artificial cilia. Next I motivate the cilium as a useful biomimic by presenting the structure and functions of biological cilia. I also present an overview of the theoretical and experimental work in regards to cilia-driven fluid flow. Finally, the last section of this chapter discusses the technological work of relevance. This includes the field of microfluidics, which will provide a background for the most likely applications of biomimetic cilia, as well as the previous work in responsive microstructures, of which a number are competing versions of artificial cilia.

3.1 Biomimicry at the Microscale

One of the classic examples of biomimicry, which also exemplifies the fact that many biomimetic projects seek to replicate *structure*, is the invention of Velcro in 1941 by Swiss engineer George de Mestral. He had used a microscope to observe that the burrs stuck to this clothes after a walk in the woods were covered in small hooks which would grab onto loops of fiber in clothing or animal fur. Under small loads the burrs would adhere, while under a large force the burr could be removed, inspiring his creation of the reusable adhesive. This example demonstrates the typical course of development in biomimetics: an interesting natural phenomenon is observed, it is studied in order to reveal the design principles the phenomenon is based upon, and finally a commercial product is developed which replicates the design and function.

3.1.1 Gecko setae

Geckos possess hierarchically structured 'hairs', called setae, on the pads of their feet which are remarkably suited as an adhesive (Ruibal and Ernst, 1965). In contrast to Velcro and more conventional sticky adhesives, the adhesive properties of gecko setae do not stem from a physical interaction. Instead, the ability of the gecko to climb smooth, vertical walls depends on carefully designed structure at the nanoscale. The hierarchical structure of the gecko's setae culminates in spatulae which are 200 nm in width, as shown in Figure 3.1. The tens of thousands of spatulae are small enough to each come into close contact with any surface, and adhere based on the Van der Waals interaction. At the largest scale, gecko foot pad's are covered in overlapping lamella which are visible to the human eye. Much smaller are the seta themselves, which cover these lamella and are 100 μm long and 5 μm wide. Finally, each seta branches at the tip into 100-1,000 of the spatulae.

The gecko's ability is fascinating for a number of other reasons as well. The gecko can move at about 1 $^{m}/_{s}$. If their setae adhere so well, how do they easily remove their feet to move so fast? Following the trajectory of biomimetics research, fairly recent observations revealed that the direction the gecko applies a force against the wall determines whether the setae are strongly attached or can be easily removed. A small force applied tangentially to the surface causes the spatulae to stretch out and flatten against the surface, increasing the area and thus the adhesive force. When the gecko removes this force and pulls normal to the surface the area is decreased and the gecko can remove its foot. Another feature of the setae structure, which I will discuss in more detail below for the lotus leaf, is that the gecko's footpad requires no grooming to be kept clean (Hansen and Autumn, 2005).

The adhesive properties of the gecko setae make them an attractive candidate for a biomimetic product, and a number of groups have demonstrated artificial setae with

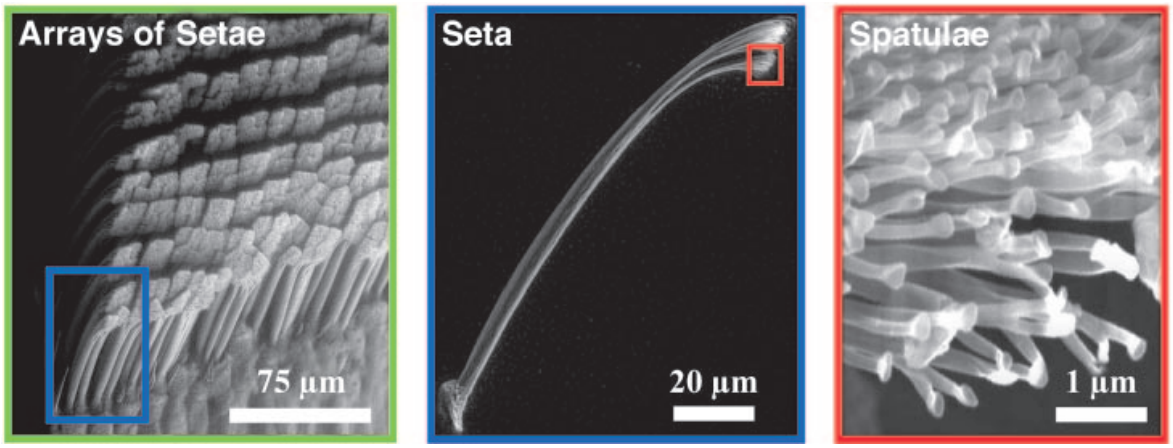

Figure 3.1: From Hansen et al. (2005). The hierarchical structure of the gecko setae provides it with impressive adhesive properties which do not rely on stickiness, and biomimetic versions are being widely pursued.

impressive adhesive properties (Geim et al., 2003). In general, these groups have attempted to replicate the hierarchical structure down to nanorods or nanoparticles of the same size as the spatulae. Many of the fabrication strategies for these types of structures share common features with the fabrication process for biomimetic cilia which I present in Chapter 5 , and some of the difficulties encountered are similar as well. A general problem is that man-made, high aspect-ratio structures are prone to failure by adhesion between neighboring nanorods. Of course it is particularly poignant that, for gecko mimics, this failure mode is via the same Van der Waals interaction which the designs attempt to take advantage of. This also serves as another example of the types of challenges faced when attempting to duplicate biology, because gecko setae do not suffer from this issue. Nor, for that matter, do biological cilia.

3.1.2 Lotus leaf

The lotus leaf shares the gecko's ability to passively maintain a clean surface (Barthlott and Neinhuis, 1997). This self-cleaning mechanism has already been incorporated into a wide range of commercial products, such as stain-repellant fabrics, and improved

methods for producing self-cleaning surfaces are currently under development for use in hospitals and other facilities where sterility is important. The lotus leaf's ability stems from the fact that water droplets bead up and roll off its surface very easily. As the beads of water roll they accumulate dust and dirt, cleaning the surface as they go.

Many types of leaves have a waxy surface which causes water to bead, but the lotus leaf takes it a step further by incorporating microscale structure into the surface of its leaves. This structure produces a rough surface, and this small scale roughness is the key to the lotus leaf's ability. Materials which have such extreme water-repellant abilities are known as superhydrophobic. The affinity of a material for a liquid can be measured via the contact angle, depicted in Figure 3.2, of the droplet on the surface. Typically, the surface chemistry of a solid determines whether it is hydrophilic, water-loving, or hydrophobic, water-fearing. But the discovery of the lotus leaf was one of the first indications that surface topology can play just as important a role. Because of the many potential applications of self-cleaning surfaces, a significant amount of effort in many groups has been put into the fabrication of superhydrophobic surfaces (Lau et al., 2003). As with the gecko, many of the fabrication processes share similarities to the process I use for biomimetic cilia, and I have observed that, as one would expect, the cilia surfaces I develop are also superhydrophobic.

3.2 The Amazing Cilium

Cilia and flagella are the fundamental structures with which cells and microorganisms interact with their fluid environments. Cilia, especially, have been experiencing a profound renaissance over the last decade as new functions performed by these structures continue to be discovered. One of the most surprising realizations is that a common type of cilium plays a critical role in fundamental biochemical signaling pathways. Cilia dysfunction can prevent the correct function of such pathways and can

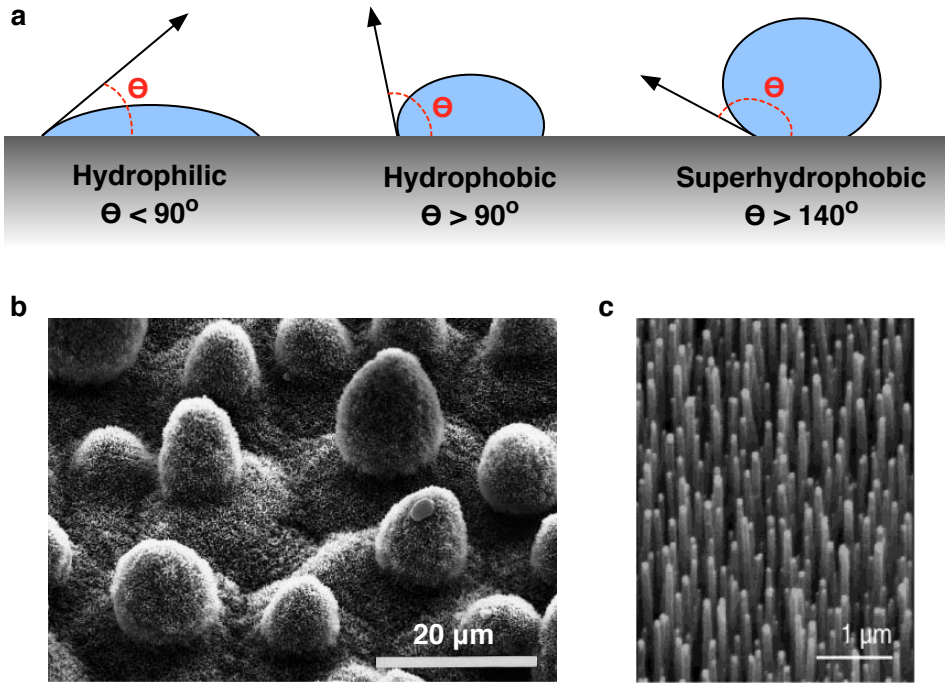

Figure 3.2: The contact angle Θ is a measure of a surface's affinity for water. The surface of the lotus leaf, shown in the SEM in (b) from Barthlott et al. (1996), is rough on multiple length scales, providing it with superhydrophobic properties and the ability to self-clean. This self-cleaning behavior has aroused interest as an appealing feature of a biomimic, and many studies have developed superhydrophobic surfaces by mimicking the lotus leaf's topology, as in the carbon nanotube 'forest' of (c) from Lau et al. (2003).

therefore impact many aspects of human health. In fact, it has become apparent that a wide spectrum of disorders, which were once considered distinct, have cilia dysfunction at their heart. Despite the cilium having been discovered in 1898, in just the last five years recognition of their importance has inspired the term 'ciliopathies' to refer more generally to the broad class of health issues caused when cilia are not present or dysfunctional.

In order to provide an overview of the role of the cilium in biology, in this section I will present various types of cilia and the functions they perform. In the following two sections (3.3 and 3.4), I discuss theoretical and experimental work, respectively, on the fluid flows driven by biological cilia.

To begin this section I will introduce the two main types of cilia, as well as a subtlety of their classification which can sometimes lead to confusion. Generally the most precise classification is based upon the ultrastructure of the ciliary axoneme, of which the large majority of cilia can be broken into two categories, so-called 9+2 cilia and 9+0 cilia. Traditionally 9+2 cilia were motile while 9+0 cilia, also known as primary cilia, were not. Unfortunately, the embryonic nodal cilium was discovered a decade ago and is a primary cilium which is also motile. This often leads to confusion, as the classifications used in the literature are sometimes based purely on motility.

The more precise classification scheme of 9+0 or 9+2 cilia is based on the internal structure of the axoneme. As I have mentioned, in both types of cilia the basic structural supports are paired, or doublet, microtubules which extend along the length of the cilium. Primary cilia contain 9 doublets arranged around the perimeter of the cilium, whereas the second class of cilia have these 9 doublets plus an extra set of two singlet microtubules which run down the center of the cilium. Thus, primary cilia are typically termed 9+0 while the second class of cilia are 9+2. Another difference is that primary cilia are typically found one per cell, while 9+2 cilia are found in patches which can

Figure 3.3: From Marshall et al. (2006). These scanning electron microscope (SEM) images demonstrate a subset of the various systems in which biological cilia have been identified as playing a critical role.

contain up to 100 cilia per cell (Satir and Christensen, 2007).

3.2.1 Ciliary ultrastructure

The textbook description of the cilium is typically that of the motile, mucus-clearing cilia of the airway epithelia. There are a number of other systems in which motile cilia perform important functions, which I will discuss below, but in general 9+2 cilia such as those in the airways perform functions which utilize the cilia beat in order to allow cells and microorganisms to interact with fluids. Most commonly, these interactions

are used for motility of the entire cell or organism and to drive the transport of fluids.

Ciliary motility is generated by the action of the molecular motor axonemal dynein. As I mentioned earlier, cytoplasmic dynein is one of the motors responsible for organelle transport along microtubules in the cell. In order to walk along a microtubule, dynein and other molecular motors typically have two globular heads which alternate binding to the microtubule in order to walk along it and convey the cargo attached to the tail of the motor. Microtubules are polar structures with ends typically termed plus and minus ends. Dynein and another molecular motor, kinesin, form two superfamilies of proteins of which the various types are found in various species. Dynein only moves toward the minus-end of the microtubule, while kinesin is a plus-end directed motor. In addition to transport within the cell, the cargo-carrying function performed by these motors also drives intraflagellar transport (IFT), the process which is responsible for the construction of the cilium as well as trafficking along the cilium (Satir and Christensen, 2007).

As opposed to when it is carrying cargo, to produce cilia bending axonemal dynein walks along one doublet microtubule, while the tail is fixed to an adjacent doublet microtubule. Because the adjacent doublets are fixed at the base of the cilium this walking motion results in a bending deformation of the cilium. Approximately 3,000 dyneins per cilium generate the forces between doublet microtubules that produce bending, but in general the mechanisms by which the action of each dynein are coordinated into a stable, oscillatory motion of the cilium are not known.

Observations of dysfunctional cilia, as well as the example provided by the motile primary cilium in the embryonic node, suggest that the 'natural' beat of a cilium is helical or conical. In contrast, the more typical motile cilium typically beats with a back-and-forth, whiplike motion in what is often called a planar beat. Thus, it is expected that the additional structural elements provided by the two singlet microtubules

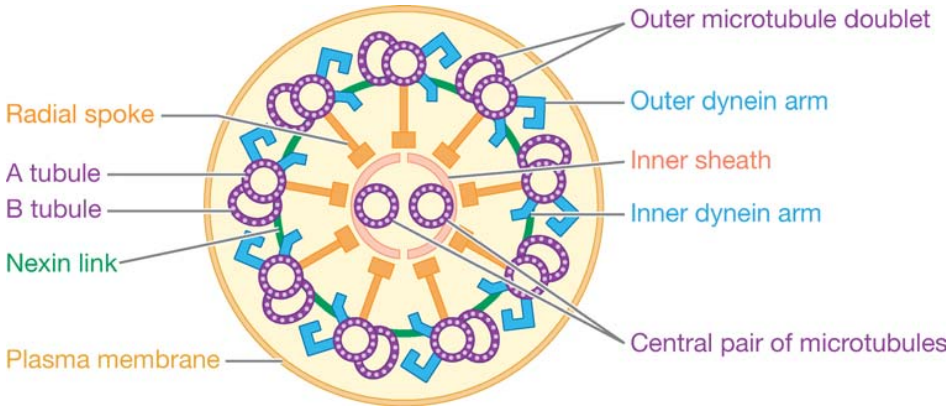

Figure 3.4: From Fauci et al. (2006). The ultrastructure of a 9+2 cilium. The doublet microtubules around the perimeter are connected by the inner and outer dynein arms. Dynein generates forces between the doublets which generate cilia bending. The direction of the planar beat of most motile cilia is the direction perpendicular to the line which joins the centers of the singlet microtubules in the core of the axoneme.

in 9+2 cilia are responsible for this beat type. Structurally, these singlet microtubules are coupled to the ring of doublet microtubules by radial spokes, and there are also nexin links between adjacent doublets as depicted in Figure 3.4 (Satir and Christensen, 2007; Hirokawa, 1998).

The planar beat shape of the airway cilium is the most well-studied. Although over one beat cycle the cilium stays roughly within a single plane, the beat itself can be deconstructed into an 'effective stroke', which is typically in the direction that the cilia drives fluid flow, and a 'recovery stroke' which is opposite the direction of fluid flow (Satir and Christensen, 2007). These two parts of the beat cycle are differentiated by changes in the contour of the cilium. During the effective stroke the cilium is essentially straight, while in the recovery stroke the cilium bends to a larger degree such that its tip is at a lower height than during the effective stroke. This shape change is critical to the success of this type of cilium in driving fluid transport at low Reynolds number, because without inertia a simple change in velocity with no associated shape change will not produce transport.

3.2.2 Functions of 9+2 cilia

Mucociliary clearance

The ability of the 9+2 cilium to drive fluid transport, combined with the ubiquity of fluid environments at the microscale, is a main reason why the motile cilium performs such a vast array of functions. The classic biological ciliated system is the process of mucociliary clearance in the airways of many mammals. The lung itself has no intrinsic defense against infectious and toxic agents, and so protection from these and other contaminants is accomplished by the combined action of the cilia beat and the rheological properties of mucus. Mucus is secreted by goblet cells in the epithelium and forms a thin layer coating the airways which acts much like a fly trap. When contaminants enter the airways they impact the mucus layer and adhere. The ciliary beat then moves mucus up the airways and into the mouth, where it can be swallowed and sterilized by digestive processes. In this way, cilia perform a crucial function by maintaining the cleanliness and sterility of the airways.

The liquid lining the airways, known as the airway surface liquid (ASL), is actually structured into two layers. The periciliary layer (PCL) is the bottom level of the ASL and extends from the epithelium up to, roughly, the height of the cilia tips. The PCL is thought to be a simple, watery liquid, in dramatic contrast to the mucus layer, which sits on top of the PCL (and thus the cilia). The mucus layer is highly viscoelastic and interfaces with air at its top surface. An understanding of how the cilia beat couples to the mucus layer and produces transport is still being developed, but a conventional picture is that during the effective stroke the tip of a cilium extends into the mucus layer, dragging it along, while during the recovery stroke the cilium bends to move below the mucus layer.

When the process of mucociliary clearance goes awry the effects on health can be dramatic and often result in shortened life spans due to chronic infection and other

disorders. One failure route is the rheological properties of the mucus itself, which is of particular importance to the Virtual Lung Project because this is the case in cystic fibrosis. Cystic fibrosis is a disorder characterized by the inability to properly regulate the hydration of the mucus. In patients with cystic fibrosis this results in a thick mucus, causing the PCL to collapse and essentially crushing the cilia such that they can no longer beat. The mucus then ceases to be effectively cleared, leading to chronic infection, structural remodeling of the lung, and life expectancies of 20 or 30 years (Matsui et al., 1998).

Other routes for the breakdown of mucociliary clearance involve dysfunction of the cilia themselves. A number of mutations have been identified which can cause the cilia to beat improperly, often in short, rigid beats which do not effectively clear mucus. Other mutations can cause the cilia to be completely immotile or even absent entirely. When this is the case, the breakdown in mucociliary clearance and associated symptoms are a subset large number of potential health problems. I will return to the broader scope of these disorders below.

Oviductal cilia

Motile, 9+2 cilia also line the epithelia of the mammalian oviduct, the fluid-filled tube which connects the ovaries with the uterus, and along which a fertilized ovum must be transported in order to successfully enter the uterus. The cilia beat in this system is thought to assist ovum transport in two ways. After ovulation, the ovum must first be able to enter the opening to the oviduct called the ostium. The oviduct can be thought of as a tapered tube, with the ostium opening up into the narrower end, the ampula, while the end nearest the uterus, the isthmus, is the widest end. In order to enter the ostium, it is believed that the cilia tips actually adhere to a layer of cumulus cells in an elastic matrix which surrounds the ovum. The cilia tips help 'churn' the ovum until

its elliptical orientation allows it to enter the ostium (Talbot et al., 1999). Once in the oviduct, cilia-driven fluid transport also assists muscular contractions in moving the ovum further down the oviduct. In this case, cilia dysfunction can make fertilization difficult or impossible.

Ependymal cilia

Cerebrospinal fluid (CSF) is the clear liquid which fills the ventricular spaces of the brain and spinal cord. Two of the main functions of CSF do not require that it flow. Namely, CSF provides buoyancy, so the brain can be heavy and soft without crushing itself under its own weight, and protection against head impacts. However, a third function of the fluid is that it flows through the intracranial spaces and is absorbed back into the bloodstream, taking with it any accumulated metabolic waste from the ventricles. The flow of CSF is driven by motile cilia which project from the ependymal cells which line these ventricles. When CSF flow is impaired, pressure within the head builds, potentially resulting in cerebral ischemia (deprived flow of blood to the brain) as well as hydrocephalus (swelling of the brain), both of which can lead to a number of cognitive impairments and death.

These traditional functions were long considered all that cilia were believed responsible for in the brain. In 2006, however, it was reported that cell migration in the ventricles follows the flow of CSF (Sawamoto et al., 2006). This was the first indication that the vectorial information conveyed by the beat of cilia could control cellular migration. It had been previously known that newly born neurons migrated from the walls of the lateral ventricles to the olfactory bulb. The ventricular spaces have a complex geometry, and this migration distance is relatively long-range, so it was not known how this migration direction was controlled. Chemorepulsion had been speculated upon, but the study by Sawamoto et al. demonstrated with an immotile cilia mutant that

the migration of these new neurons was disoriented. They further demonstrated that a chemorepellant does, in fact, play a role, but that cilia-driven CSF flow must generate a gradient of the chemorepellant across the sub-ventricular zone. This chemical gradient is then the directional signal leading the neurons out of this zone and towards the olfactory bulb.

Chemosensation

As I will discuss in the next subsection, many of the main functions of primary cilia are sensory in nature. In contrast, the traditional view was that motile cilia did not perform sensory functions. However, in 2009 the first evidence of chemosensation in motile airway cilia was reported (Shah et al., 2009). It was observed that epithelial cells expressed bitter taste receptors, and that these receptors were localized to cilia. Shah et al. presented bitter compounds to the system and observed an increased concentration of Ca^{2+} and a stimulated ciliary beat frequency. This suggested that the cilia not only sensed the bitter compounds but mounted an increased defense mechanism to more rapidly remove the potential threat.

3.2.3 Functions of 9+0 cilia

The 9+0, primary cilium is an immotile version (except in the case of nodal cilia) and the ancient evolutionary structure from which motile cilia evolved. Virtually all eukaryotic cells possess a single primary cilium, which was widely considered a vestigial apparatus in the not-so-distant past. In actuality, the renaissance in cilia research has been partly due to the revelation that primary cilia are integral parts of biochemical signaling pathways which are critical to health. Another surprising result is that primary cilia in the kidney have been discovered to perform a flow-sensing function.

Ciliopathies

While motile cilia effect a physical change which can be analyzed, in many cases studies of primary cilia must resort to the use of genetic mutants combined with research into genetic disorders which stem from cilia dysfunction. The fact that genotypic cilia mutations can have diverse and seemingly unrelated effects on phenotype is partly to blame for the relatively long time it took researchers to recognize the importance of cilia in human health. Historically, Kartagener's syndrome, now known as primary cilia dyskinesia (PCD), was one of the first hints of this fact. Patients with PCD often suffered from impaired mucociliary clearance, which can lead to chronic sinusitus and bronchiectasis, as well as infertility. Finally, another common symptom was that approximately 50% of those with PCD had *situs inversus*, a condition where the left/right asymmetries in the human body plan were reversed from the normal body plan (e.g. the heart tilts slightly to the left, the right lung has two lobes instead of three, the liver is on the right, etc.).

Studies of Kartagener's syndrome soon revealed that the cilia of those with the disorder had either too few or no axonemal dynein. This meant that the cilia could either not beat at all, or beat dykinetically, which resulted in renaming the syndrome as PCD. To a degree this was not surprising considering that the chronic infections of the respiratory system could be explained by a breakdown in mucociliary clearance. However, it was initially difficult to explain the connection with these symptoms and *situs inversus*.

This difficulty inspired a new look at the embryological process of symmetry breaking. I will outline this system in detail below, but this research revealed the existence of a fluid flow driven by the embryonic nodal cilia. Thus, the last symptom of PCD was incorporated into a model of cilia dysfunction, because without dynein these nodal cilia are also immotile and the mechanism for determining left/right vertebrate body

asymmetry is randomized.

This surprising link between embryo development and the action of a primary cilium was partly established with studies of cilia mutants. After identifying this link, further studies of cilia mutants revealed distinct phenotypic effects depending on the mutation. Further inquiry demonstrated that some of these phenotypes were caused by disruption of the hedgehog (Hh) signaling pathway, which is a widely conserved pathway responsible for many aspects of development. Disruption of this pathway can cause improper development of the brain, skeleton, musculature, and other systems, as well as various cancers (Pazour and Witman, 2003; Eley et al., 2005).

In parallel with these genetic studies, medical research began to link other rare recessive human disorders to mutations in proteins which were localized to cilia. This confluence of evidence resulted in the creation of the term ciliopathies to refer to this broad class of health issues which stem from ciliary defects (Badano et al., 2006). In addition to the afflictions already mentioned, these ciliopathies can result in cystic kidneys, obesity, mental retardation, blindness, and many developmental malformations. For more information, such ciliopathies were reviewed by Sharma et al. (Sharma et al., 2008).

Primary cilia sense fluid flow in the kidney

While the biochemical signaling performed by primary cilia plays many important roles, some of which are of relevance for the discussion in Chapter 6, the two types of primary cilia which are of most relevance to my thesis are those which interact with fluids. One of these is the primary cilium found on MDCK cells, a widely used cultured cell line from the canine kidney. In 2001 it was observed that these cells increased intracellular calcium levels if their primary cilia were deflected, either in a fluid flow or with the tip of a pipette needle (Praetorius and Spring, 2001). This

provided the first evidence that fluid flow based bending of a primary cilium might activate mechanosensitive channels which cause a detectable response in the cell. When these cilia are dysfunctional the result is polycystic kidney disease (PKD), a ciliopathy characterized by the growth of cysts throughout the kidney which leads to swelling, abdominal pain, and eventually kidney failure.

Embryonic nodal cilia

The primary cilia system of the most relevance to this work is that of the embryonic node. In 1994, it was reported that motile cilia had been observed in the node of a mouse embryo (Sulik et al., 1994). The node is a fluid-filled, recessed pit with a membranous covering which appears in various forms on the ventral surface of all vertebrate embryos (Essner et al., 2002). Because this report was of motile, primary cilia it was initially met with some controversy (Bellomo et al., 1996). However, further studies of mouse embryos performed in 1998 by Nonaka et al. confirmed the motility of the cilia, and also reported that the cilia generated a directional fluid flow across the node, which was consistently pointed towards what would soon develop to be the left side of the embryo. However, this fluid flow existed before any other detectable asymmetries, either anatomical or chemical. Thus, for the first time biologists began to wonder if the physical mechanism of a cilia-driven fluid flow might be somehow transduced into the left-side chemical signaling cascade which was, up to that point, the earliest example of an asymmetric event. In this section I present an overview of the embryonic nodal system.

Further confirmation that the cilia-driven fluid flow controlled left/right asymmetry was demonstrated by the controllable patterning of the murine body plan with the external application of fluid flow, after removal of the membranous covering of the node (Nonaka et al., 2002). The next question was to determine how the fluid flow

was transduced into a chemical signal. The 'morphogen transport' model was first proposed, which suggested that the leftward flow establishes a chemical gradient across the node which triggers the cascade. However, mutant studies had again revealed several phenotypes which were not easily explained by this model. Thus, a competing framework called the 'two-cilia' model was postulated (Tabin and Vogan, 2003), which was based on the recent discovery of a second class of immotile cilia which were localized to the periphery of the node (McGrath et al., 2003). It was suggested that these immotile cilia might be mechanosensitive, as in the kidney, and produce an asymmetric response on the left side of the node.

However, considerations of the symmetry of the flow led others to conclude that mechanosensitive cilia on either side would feel the same force, and thus this model has fallen out of favor to some degree (Cartwright et al., 2004). In addition, more recent observations have bolstered the morphogen transport model, albeit in a modified form. Specifically, a fascinating system has been observed within the node whereby lipid vesicles are dynamically extended away from the cell surface by microvilli, released into the leftward fluid flow, and subsequently rupture on the left side of the node (Tanaka et al., 2005). These vesicles are loaded with morphogens such as retinoic acid (RA) and sonic hedgehog (SHH) during formation, and the vesicles release these morphogens upon rupture. Thus, this novel mechanism allows these 'nodal vesicular parcels' (NVPs), which are roughly 500 nm to 3 μm in diameter, to establish the initial chemical gradient on the left.

Based on this evidence, it is likely that some version of the morphogen transport model is likely correct. However, a number of questions remain unanswered. A key issue is how this initial gradient is sensed, and how the gradient evolves in time in the cilia-driven fluid flow of the node. It is known that the main leftward flow drives a counter-flow along the ceiling of the node, which occurs because the node is a completely

enclosed structure and the net flow rate must be zero. Thus, the morphogens released upon vesicle rupture must eventually be transported back to the right, and additionally these small molecules diffuse relatively rapidly. It is expected that the morphogens may have an inactivation time which allows the gradient of functional morphogens to be maintained, however this has not been shown to be the case. If the morphogens do become inactive after some time, then a stable gradient can only persist if the vesicles are released repeatedly in order to replenish the supply of morphogen on the left. Indeed, the discoverers of the NVPs reported the observation of released vesicles being transported across the node every 5 to 15 seconds.

As I have discussed, primary cilia have been shown to be one of the cell's fundamental sensing units, and so it has been proposed that the second population of immotile cilia, originally posited to be mechanosensitive, may in fact be one of the primary locations for chemoreception of the gradient. However, at present the location of the receptors has not been established (Hirokawa et al., 2009).

Another open question is the mechanism by which the NVPs are ruptured. Tanaka et al. reported that the rupture occurred most often on the left side of the node, and speculated that impacts with the beating cilia and/or the walls of the node caused rupture (Tanaka et al., 2005). However, a simple argument made by Cartwright et al. in a followup to their 2004 paper demonstrated that the impact force is not likely to be larger than the Stokes drag which the vesicle was subjected to before release from the microvillum (Cartwright et al., 2004), and so chemo-induced NVP rupture is now thought to be likely.

The same study to observe the NVPs further reported that a separate signaling pathway which requires the presence of fibroblast growth factor (FGF) is also needed in order for the system to function (Tanaka et al., 2005). In a mutant unable to produce FGF these vesicles were never successfully formed and embryos had randomized *situs*.

A separate issue which has been largely resolved is how the nodal cilia beat generates fluid transport. As I mentioned, the nodal cilia beat is very different from the planar beat of the typical motile cilium. Early observations of nodal cilia showed that they beat in a 'conical', or rotational beat, meaning that over each beat cycle the cilium sweeps out the lateral surface of a cone (Nonaka et al., 2002). For reasons which will become more clear in Chapter 5, in general this type of beat should not produce any net transport of fluid. Furthermore, the dyskinetic beats of motile cilia can sometimes be roughly of this shape, and such cilia are dysfunctional in these systems.

In 2004, a theoretical model was presented by Cartwright et al. which predicted that in order to generate fluid transport this conical beat must rotate around an axis which is tilted away from vertical (Cartwright et al., 2004). In the model, rotation around a vertical axis only produced locally vortical motion, as would be expected from symmetry, but the tilting of the cilia away from vertical generated directional transport above the rotlets. This model was limited, as it did not include any boundaries and the modeled elements were simply rotlets. But despite these limitations, the following year two publications presented observational evidence of a conical beat which was tilted (Okada et al., 2005; Nonaka et al., 2005), confirming Cartwright et al.'s prediction.

It has since been appreciated that this 'tilted conical beat' generates fluid transport because of the fluid's interaction with the floor. The movement of a fluid is increasingly constrained as it nears the floor because of the 'no-slip' boundary condition, which specifies that the local fluid must not move relative to a boundary it is directly in contact with. Due to the tilted rotational axis, over one half of the beat cycle the cilium is closer to the surface than during the other half of the beat. Thus, the cilium's motion nearer to the floor generates less fluid motion than when the cilium passes farther from the floor. The net result of a single beat cycle is fluid transport roughly in the direction of the motion of the cilium tip at the point when it is farthest from the

floor.

3.3 Theoretical Work on Biological Cilia-Driven Fluid Flows

There is quite a vast literature of theoretical treatments of biological cilia, extending back to the original work of G.I. Taylor in 1951 (Taylor, 1951). His work initiated what could be thought of as the first period of theoretical cilia research, which lasted through the early 1980s. The renaissance in cilia research has now ignited a second period of study which is expanding and refining the results of the earlier research. The models developed in the early work on cilia can be broadly put into two groups, the envelope model and the sublayer model. The envelope models considered a two-dimensional sheet with transverse waves propagating through it. The sublayer models utilize the singularity methods of slender body theory which I discussed in Chapter 2. In general, the goals of these early researchers were twofold. First, they sought out explanations for the general propulsive ability of cilia and flagella. Secondly, the synchronization of flagella beating in close proximity to each other had been observed as far back as 1928, and Taylor's 1951 paper first highlighted the possibility that this synchronization is due to hydrodynamic forces.

The second period of cilia research began in the last decade and continues today. The impetus for this is partly the realization of the diverse functions cilia play, but also simply the increased availability of the computational power needed to explore more accurate approximations of cilia-driven flow. Interestingly, the synchronization between flagella and cilia is still an area of much research (Mitran, 2007). The basic principles which underly cilia-driven fluid propulsion were explored in the first period of research, but today the rising popularity of systems biology and computational medicine provide

motivation for understanding cilia systems at a more sophisticated level.

For the purposes of this thesis, it is easiest to generalize these two periods of research in relation to my own results. Because the early researchers were seeking to predict swimming and fluid propulsion velocities, there results were often focused on the far-field velocity predicted from their models. This far-field velocity was taken to be the swimming/propulsive steady-state velocity the cilia could generate. Thus, the earlier literature has the most relevance to the results I present in Chapter 5 , because in that chapter I focus on the fluid flow driven by my biomimetic cilia above their tips. Thus, I first present a few more details on the models which make similar predictions to the results I present for this flow regime. I will follow this with a more specific discussion of recent work which, in contrast to the earlier period, has just begun to focus on particle motion in closer proximity to cilia. Thus, these later works are of more relevance to the discussion in Chapter 6, where I present results on the fluid flows below the cilia tips in my system.

Taylor's initial development of the envelope model considered the fluid flow around the waving sheet as a model of the propulsive ability of the flagellum. Later work by Blake used the same model but considered the sheet as an approximation of the flow driven by densely packed arrays of cilia. This was motivated by the metachronism observed in cilia arrays, which was modeled by the transverse wave traveling through the sheet (Blake, 1970). Such a model has some obvious shortcomings however, such as the requirement of small amplitude oscillations in the sheet and the no-slip boundary condition at the cilia tips. The sublayer models were developed in order to surmount both of these disadvantages.

The sublayer models can be further broken down into two categories, the original distribution of Stokeslets work pioneered by Blake et al. and an approach by Keller et al. which he called the traction layer model. The traction layer model simplified the

cilia by assuming the force generation was uniformly distributed in the layer below the cilia tips, which allowed the model to incorporate unsteady effects such as metachronism (Keller et al., 1975). For this reason, the singularity methods Blake developed are also sometimes referred to as discrete techniques to contrast with the traction layer model. Both methods had considerable success in explaining the ability of cilia to generate fluid transport (or, conversely, microorganism motility), and were able to match experimental observations within an order of magnitude or better. This early period of research is comprehensively reviewed by Brennen and Winet (Brennen and Winet, 1977).

The aspect of this early period which is of most relevance is the work by Liron in the late 1970s. He extended the image system developed by Blake to a model of transport between parallel plates. The biological system of interest was the oviduct. As the entire duct is filled with a Newtonian liquid it is much more amenable to theoretical work than the viscoelasticity and air-liquid interface of the mucus above airway cilia. Most interesting was Liron's comparison of the effect of a Stokeslet above a single plane with the effect of the same Stokeslet between two plates. Blake's earlier work had demonstrated that the Stokeslet image system did produce a net flux, which partly justified the singularity methods as a model of cilia-driven transport. In contrast, Liron showed that when a top boundary is added, this flux necessarily becomes zero. However, because of the addition of the top plate, Liron was able to superpose a plane Poiseuille flow onto the flow generated by the Stokeslets, which had not been possible in the earlier semi-infinite models. His work demonstrated that, with the top boundary in place, in order to achieve a net flow the addition of such a Poiseuille flow was required to counteract the return flow generated in the far-field by the Stokeslets. This work was the first theoretical prediction of a velocity profile for cilia-driven flow in a system bounded on top and bottom. The flow velocity just above the cilia tips initially decayed

linearly with distance, but the final shape of the velocity profile over the entire height depended on the strength of the added Poiseuille flow (Liron and Meyer, 1980; Liron, 1978).

3.3.1 Near-field theoretical predictions

More pertinent to my thesis work is the more recent period of research, which has only just begun to present models which can predict the fluid flow in closer proximity to the beating cilia. As such, this is the most likely arena in which a biomimetic cilia model can contribute to the understanding of biological systems. Below I present the theoretical results from several publications which describe fluid flow features which are similar to those I have observed.

Bouzarth et al. 2007

Even among models which have worked to predict flows near cilia, not all have contained a time-dependence. While the majority of the results in proximity to cilia are presented in Chapter 6, in Chapter 5 I describe the small scale oscillations of cilia-driven tracer particles which I call epicycles. To my knowledge, these epicycles have not been reported in any experimental work with biological cilia. However, they were a primary topic of a recent work which compared theoretical and experimental fluid flows around a single precessing rod (Bouzarth et al., 2007). Bouzarth et al. also compared macroscale and microscale versions of the experiment to probe the accuracy of their model as diffusion became significant. This highlights another important shortcoming of most cilia modeling: the difficulties associated with incorporating diffusion, which at the microscale is a ubiquitous phenomena which may have distinct effects on cilia-driven flows. I will discuss this issue in more depth below in reference to the work of Smith et al. (2007).

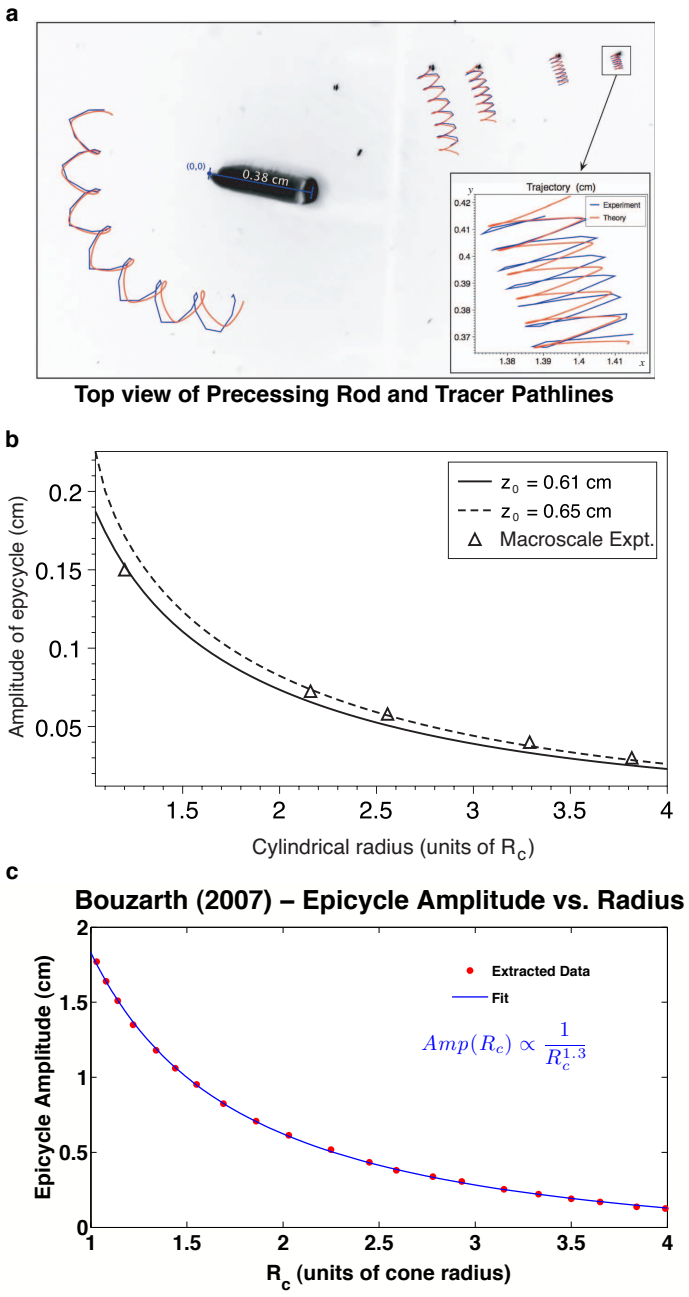

Figure 3.5: From Bouzarth et al. (2007). (a) A top-view of a precessing pin in a table-top experiment. Pathlines of video-tracked tracers are overlaid with theoretical predictions of the motion. It is clear that the epicycle amplitude and mean velocity decrease with distance from the pin, as shown in (b). The cylindrical units are normalized by the radius of the circle traced out by the pin's tip. (c) I have extracted the solid curve prediction from (b) and fit it to a power law in order to determine that the functional form of the decay with radial distance is as shown.

As expected, the model presented by Bouzarth et al. did suffer from diffusive effects which grew worse as the system evolved in time. However, their work demonstrated an impressive match between the epicycles seen in both experiment and theory over short times, as shown in Figure 3.5. As the single rod precessed around a vertical axis (essentially performing the upright conical beat I mentioned earlier), tracer particles performed slow orbits around the rod. These slow orbits were essentially a rotational vortex around the rod. In addition, the tracers also exhibited an additional oscillation at a much smaller scale, but which was at the frequency of the rod's beat. These small scale oscillations are the epicycles which I have also observed in my system. Bouzarth et al. did not report a theoretical form for the epicycle amplitude, but in Figure 3.5 I display their results for the epicycle amplitude as a function of the radius of the particle from the rod's precessional axis. In order to compare my data to this result in Chapter 5, in the same Figure I also display the data I have extracted from their plot of the theoretical model and fit the functional form of a power law to the curve in order to determine the decay of the amplitude with distance predicted by their numerical computation. The result of this fit is displayed in the plot, that the epicycle amplitude decays proportionally to $1/r^{1.3}$. The presentation of my own results with regards to the tracer epicycles can be found in section 5.2.2.

Cartwright et al. 2004, 2007, and 2008

I have already mentioned that the work of Cartwright et al. predicted the beat shape of embryonic nodal cilia based on an array of rotlets (equation 2.43). In addition to the prediction that a tilted conical beat would generate a net transport, the 2004 work was another theoretical work which predicted vortical flow around a nodal cilium, although this is of little surprise for a rotlet model. The theory was further simplified in that it was not time-dependent, ignored diffusion, and did not include any boundaries.

However, the 2004 work was still significant for other reasons than the prediction of the cilia's tilt. Despite the fact that the model did not include diffusion, this work was the first to point out the importance of the Péclet number in the system. The Péclet number is another dimensionless ratio which will be critical throughout the thesis, because it is a measure of the relative rates of diffusive and advective transport, or

$$Pe = \frac{\text{advection}}{\text{diffusion}} = \frac{uL}{D_0} \tag{3.1}$$

where u and L are characteristic velocity and length scales, respectively, and D_0 is the particle diffusivity. At large Péclet numbers advection dominates and diffusive motion can be safely ignored. On the other hand, for small Péclet numbers any advective motion is too slow to matter, and diffusion dominates. Cartwright noted for the first time that the morphogen transport in the node was an advection-diffusion system, and so the Péclet number would be important for determining how morphogen gradients would be produced. Cartwright further speculated that such an advection-diffusion system would require an inactivation time of the morphogens in order to avoid a homogenized steady-state concentration due to diffusion.

In addition, as Cartwright was the first hydrodynamicist to weigh in on the nodal cilia system, the 2004 work also cleared up some confusion as to the nature of the vortical flows which had been qualitatively described by experimentalists (Okada et al., 2005; Nonaka et al., 1998). These experimentalists had described complicated, vortical paths around cilia as turbulent flow. As the reader learned in Chapter 2, turbulence depends upon inertial effects and cannot be supported by low Reynolds number fluids, and Cartwright pointed out that these complicated paths were not turbulence. Instead, their work suggested for the first time that these particle pathlines were potential evidence of chaotic advection, a dynamical systems phenomenon which can result in chaotic particle trajectories even at low Reynolds number. I will present some

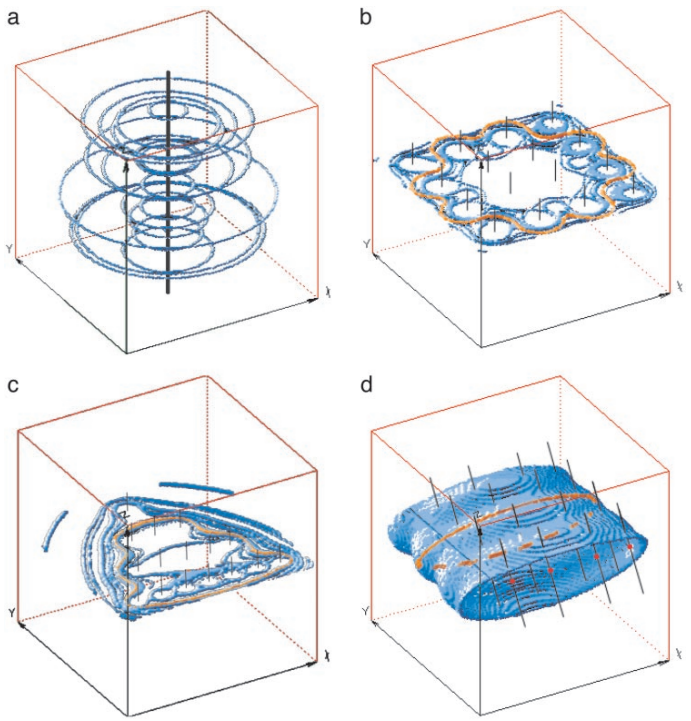

Figure 3.6: From Cartwright et al. (2004). (a) The vortical streamlines around a single rotlet are displayed. The vertical black line represents the rotational axis of the rotlet, which itself is represented by a small sphere at the midpoint of the black line. (b) An array of rotlets rotating around a vertical axis produce local vortices. In addition, some particles move around the array, but always return. (c) Demonstration that the shape of the array, which is more triangular in this case, does not change the overall effects of the flow. (d) This represents Cartwright's prediction that a tilt of the cilium's rotation axis away from vertical would result in a net transport of fluid above the cilia tips. In this model, which did not include any boundaries, there was an equal and opposite flow below the rotlets.

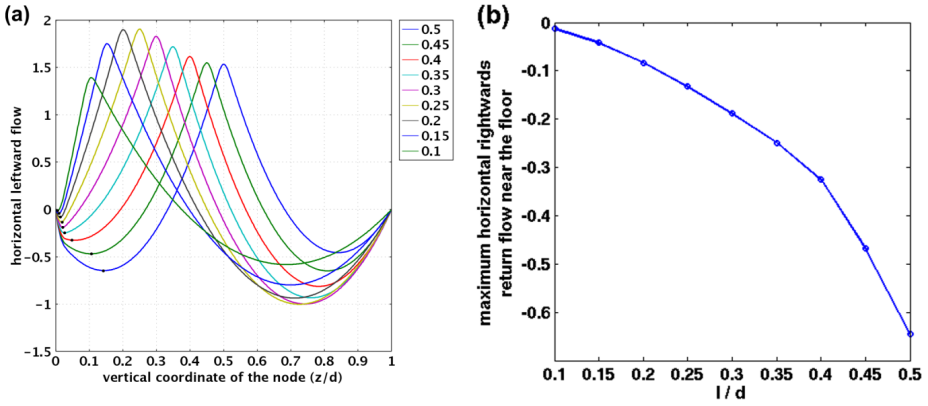

Figure 3.7: From Cartwright et al. (2008). (a) A family of velocity profiles for different values of the relative height of the upper boundary and the cilia tips, showing that the return flow only becomes pronounced when the cilia height is within a few factors of the boundary height. (b) The strength of the return flow as a function of the relative heights.

preliminary evidence for limited chaotic advection in my biomimetic cilia samples in section 6.3.2, and I will more thoroughly explain the phenomenon in that section. But it is important to note that Cartwright's speculation as to the existence of chaos around nodal cilia will be echoed by other theoretical works below. However, as of yet there has been no theoretical or experimental demonstration in the literature that cilia can generate chaotic advection.

The 2007 work of Cartwright et al. was mentioned earlier, as it published the argument that NVP rupture could not be caused by direct impact with a cilium. The other main topic of this work was a theoretical comparison of the expected *in vivo* flow with the experimental work, which for accessibility had required the removal of the membranous covering of the node. Specifically, in this work a more elaborate model included an upper boundary. This allowed Cartwright to address the existence of a recirculatory flow along the ceiling of the node, which must be present *in vivo* and should be dramatically reduced after removal of the membrane during experimentation. As I will show, the results in Chapter 5 demonstrate a recirculatory flow driven by biomimetic cilia which matches well the *in vivo* analysis of Cartwright.

The final work I will discuss by Cartwright et al. is the 2008 review of the fluid dynamics of the nodal system. Despite being a review, it did present a small amount of new theoretical work which followed up on a minor controversy which Cartwright's earlier work had ignited. The time-independent models used in these earlier works had predicted that a second recirculatory flow should exist along the floor of the node. Work I will outline below by Smith et al. used time-dependent singularity methods which did not show a floor recirculation. This work suggested that Cartwright's prediction was due to the time-independence of his model. However, Smith et al. did not have an upper boundary in their model. Thus, Cartwright addressed this issue in his 2008 work by claiming that the upper boundary dictated that this floor recirculation be present regardless of any time-dependence in the model. Figure 3.7 displays a family of velocity profiles from Cartwright (2008), demonstrating their prediction that the strength of the floor recirculation was a function of the height of the node relative to the height of the cilia tips. While this velocity profile shares features with results I present in Chapter 5, in neither my system or any other biological experiment to date has there been a report of the observation of the floor recirculation. My data suggests that Smith et al. are correct that the complex trajectories of particles below the cilia tips will overwhelm any average recirculatory flow and make it difficult or impossible to discern, if it is actually present.

Smith, Blake, and Gaffney 2007 and 2008

John Blake, who first solved Batchelor's slender body theory for a cilium and a boundary via the method of images in 1971, has recently extended some of the early period of research with further reports of relevance to the airway and the nodal flow (Smith et al., 2007; Smith et al., 2008). The recent work concerning the airway has been an attempt to resolve a discrepancy between experiment and theoretical work. This discrep-

ancy will be important to the discussion of the results in Chapter 6 and the biological implications of my work. For that reason I will take this opportunity to introduce one of the fundamental questions which I will address: what is the nature of any potential mixing flows which would be driven by beating cilia?

The discrepancy which I have alluded to began with experimental reports (by colleagues in the Virtual Lung Project) which showed that fluid flow tracers, in the form of patches of fluorescent dye, were transported equally in both the PCL below the cilia tips and the mucus layer above (Matsui et al., 1998). This 'co-transport' phenomenon was very different from the velocity profiles which had been typically predicted by theoretical results, as shown in Figure 3.8 from Smith et al. (2007). The work by Smith et al., as well as an unpublished computation performed by Sorin Mitran of the Virtual Lung project (which can be found here), were some of the first models to include diffusive effects. These models suggested that the tracers used in the experiment were not faithfully following the velocity field due to diffusion, causing at least some part of the discrepancy with theory.

However, the detailed work by Smith et al. in 2007 required a series of further modifications in order to fully bring the theoretical predictions into alignment with the co-transport observations. First, diffusive enhancements between the mucus and PCL were assumed. Matsui et al. had reported that the dextran dyes used their experiments had diffusivities of 160 $\mu m^2/s$ in the PCL and 3.6 $\mu m^2/s$ in the mucus layer. Thus, the initial proposal was that once dye diffused from the faster-moving mucus into the PCL, it more rapidly spread out and made it appear that the PCL had been co-transported.

This first proposal decreased, but did not eliminate the discrepancy. Further improvements were made by combining features of discrete methods and the traction layer model. The discrete methods were shown to predict that, in the upper portion of the PCL, shear-flow driven by the transport of the overlying mucus dominated any back-

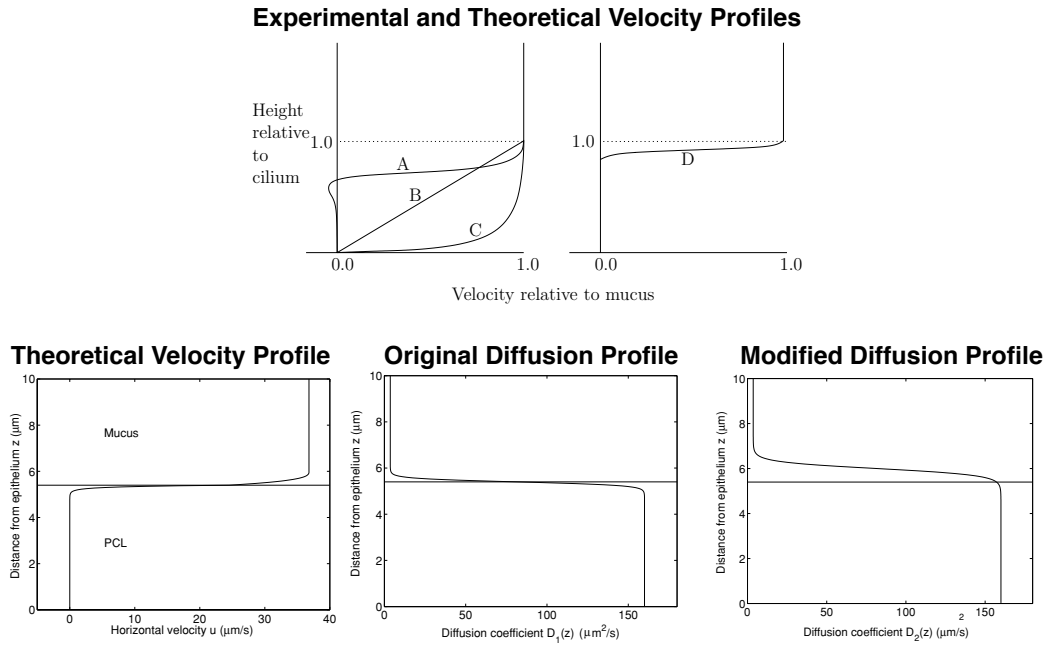

Figure 3.8: From Smith et al. (2007). Top row - Possible airway cilia-driven velocity profiles: A is typical of that predicted by theory, B is expected if the mucus drives Couette flow in the PCL, and C is that observed in experimental work by Matsui et al. D is the velocity profile from Smith et al.'s own work. Bottom row - The original theoretical profile is partly reconciled with the experimental profile by including enhanced vertical diffusion between the PCL and the mucus, which is assumed to occur because of the interaction of the cilia tips with the mucus layer.

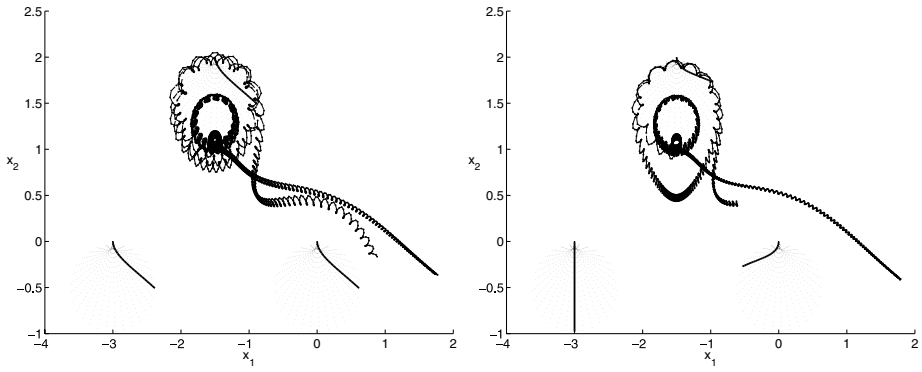

Figure 3.9: From Smith et al. (2007). Their model incorporated time-dependence and diffusion. These tracks depict the trapping-and-escape behavior discussed in the text, in which particles are temporarily confined to the local vortex around a cilium before escaping.

wards flow a cilium would generate during its recovery stroke. This was combined with a feature of the traction layer, which was the ability to predict the effect of oscillations in the fluid due to the cilia beat. These two effects were enough to bring the theoretical predictions within a few percent of the experimental observations. Thus, Smith et al. reported that the mean transport in the PCL need only be 50% of that in the mucus, and that these additional effects would make it appear in experiments as though the PCL was being co-transported.

These theoretical works highlight the fact that the detailed motion of the fluid generated in close proximity to the cilia can be important for the basic transport phenomena in a ciliated system. However, the effects predicted by Smith et al. have not been described in an experimental cilia system. This highlights the importance of the results I will present in Chapter 6, which will speak to the notion of an enhanced diffusivity below the cilia tips.

Smith et al.'s work in 2007 in the Bulletin of Mathematical Biology also presented results on the embryonic nodal system using the same singularity methods which had been applied to the airway. In particular, this was the first work to calculate individual tracer pathlines in the fluid flows near the nodal cilia beat. These pathlines exhibited

the epicycles reported by Bouzarth et al., and also showed vortical features in the immediate vicinity of a cilium. More specifically, this was the first theoretical description of the circling-and-escape behavior Nonaka et al. had described for experimental particle trajectories (Nonaka et al., 1998). Such trajectories were characterized by initially vortical motion in which the tracer was essentially 'trapped' by the cilium. After a few orbits around the vortex particles escaped, typically entering the leftward flow above the tips. The theoretical trajectories which demonstrate such behavior are displayed in Figure 3.9.

3.4 Experimental work on fluid flows within the embryonic node

I have mentioned the experimental work on ciliated systems in a number of places above. Here I focus in more detail on the data presented for nodal cilia systems, where appropriate, in order to emphasize the lack of thorough characterization of cilia driven flows in the experimental literature. This lack is especially pronounced in close proximity to beating cilia. I have mentioned that early reports qualitatively described vortical flow around single cilium. In addition, these early works quoted mean flow speeds of 10 $^{\mu m}/_{s}$ or greater, which have been refined downward in more recent work.

Beyond these numbers, the experimental data on the nodal flow comes from two other sources. In Okada et al. (Okada et al., 2005), a comparison between species was made and the average cilia beat frequencies and flow velocities were reported for embryos of the mouse, rabbit, and medakafish. In addition, Okada et al. published a velocity profile for the mouse nodal flow which consisted of three data points. All of these values are displayed in Table 3.1, and will appear again in Chapter 5 when I compare this data to my own results.

Nodal Flow Data from Okada et al. (2005)			
Species	Height (μm)	Velocity ($^{\mu m}/_{s}$)	Beat Frequency (Hz)
Mouse	4	4 ± 2	11 ± 3
	11	0 ± 1	
	19	-2 ± 1	
Rabbit	4	1.3 ± 0.4	7 ± 2
Medakafish	4	7 ± 3	43 ± 3

Table 3.1: Nodal flow velocity data from Okada et al. (2005). The three data points from the mouse are the only experimental results for a velocity profile in the node. The comparison between species also reveals a clear correlation between beat frequency and flow velocity at the cilia tips.

The most recent experimental work to present data on the nodal flow was performed by Supatto et al. in 2008. In order to track the nodal flow with minimal disturbance to the *in vivo* condition, they demonstrated a novel technique whereby a small number of cells on the nodal wall were laser ablated. These cells, which had previously been fluorescent labeled, were lysed by a femtosecond laser pulse and fluorescent debris from the ablated cells entered into the node and could be used as tracers of the flow.

The data presented by Supatto et al. is displayed in its entirety in Figure 3.10. Although their method for *in vivo* imaging is impressive, it is unfortunate that the claims made in the text of the paper are not well supported by the presented data. The properties of the global flow are indicated by several hundred particle tracks which orbit around the node. The next displayed data set is one of the few presentations of fluid flow data in close proximity to a cilium, again indicating with vector fields the vortical flow which had been observed by previous experimentalists. It is clear, however, that the limited duration and spatial extent of these paths limits the ability to fully characterize the fluid flow.

Finally, Supatto et al. claimed in the text of their paper that their observations had revealed the presence of chaotic advection, and that this report was the first report of such a flow driven by cilia. However, I emphasize that the only data presented for

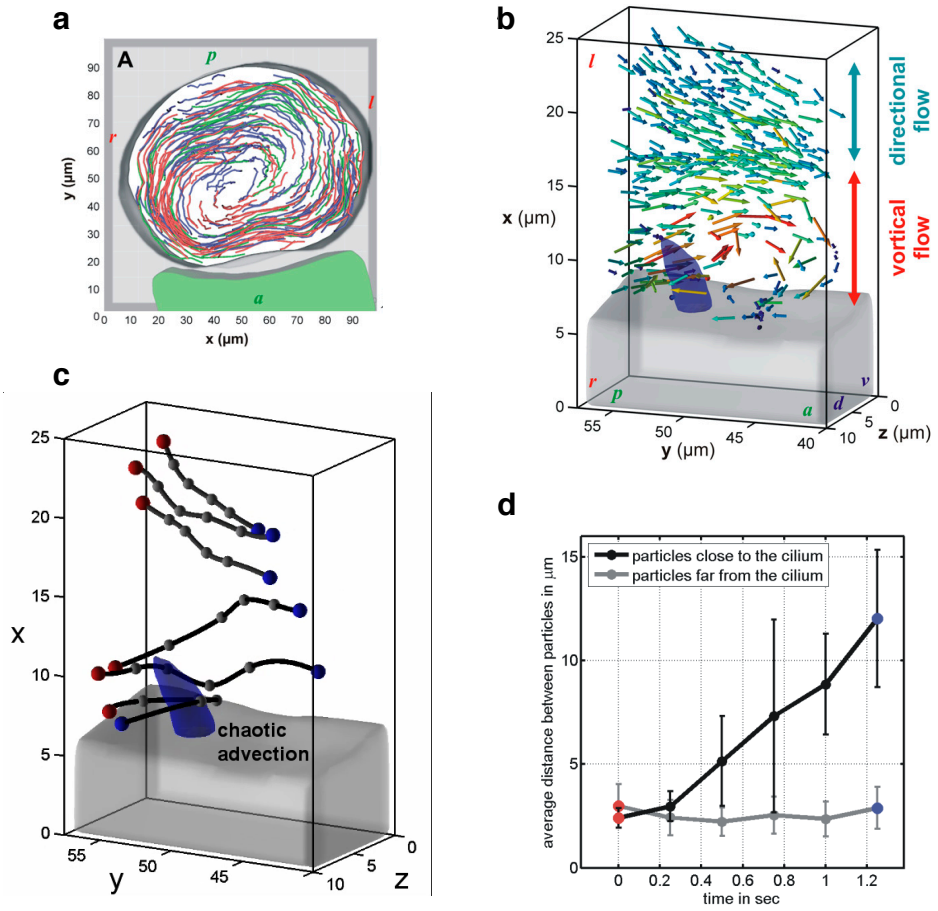

Figure 3.10: From Supatto et al. (2008). These panels display the best data currently in the literature for fluid flows in close proximity to a cilium. (a) Particle tracks in the entire node. (b) The velocity field around a single cilium (the shaded blue region). This identification of the vortical flow matches previous observations, and the transition to directional flow was noted, but it is again data limited to an area by just one cilium. (c) and (d) The entirety of the data in support of the claim that they had observed chaotic advection. In (c), the pathlines of two sets of three particles (one set near the cilium and one far from the cilium) are displayed, with the initial positions represented by the red dots and final positions by the blue. They claim that the average divergence in time shown in (d) of the three tracers near the cilium reveals the chaotic nature of the flow, but there they did not perform any characterization of chaotic advection with a metric such as the Lyapunov exponent.

such a claim is shown in Figure 3.10, some of which was only published within the supplemental information of their work. The figure shows that their observations were of three particles below the cilia tips which separated in time, with a control set of three above the cilia tips which did not separate. As I will discuss in Chapter 6, the characterization of chaotic advection is complicated and depends, at a minimum, on the *rate* at which nearby objects are separated in a flow, and so the evidence presented is clearly insufficient grounds for such a claim.

3.5 Microfluidics

As I have mentioned, a number of the potential applications of a functional biomimetic cilia system lie within the field of microfluidics, a technology based on the flow of liquids through microscopic channels (Gravesen et al., 1993; Squires and Quake, 2005). The overarching goal of this field is to do for chemistry and biology what the integrated circuit did for computing, that is, to build a 'lab-on-a-chip'. Such devices, sometimes more formally called micro-total analytical systems, would seek to miniaturize many aspects of bench-top lab work in diverse areas of biology and chemistry. Specifically, the multiplexed analysis of biological specimens and rapid, easily tunable chemical synthesis are broad goals in the field. The motivation for such devices are many, but two obvious reasons are that they are cheap to mass produce, due to the small amount of materials required to fabricate them, and the volumes of analytes are small due to the microscopic channels.

In addition, a variety of fluidic phenomena which exist at the microscale, some of which I have already introduced, provide means for performing tasks which cannot be easily accomplished at the macroscale. For instance, the surface tension of liquids can dominate fluid forces to such an extent that fluids will wick into microscopic channels, allowing surface chemistry to dictate fluid flow. Another use of surface tension which

has rapidly increased in popularity in the last 5 years is droplet-based microfluidics, in which individual droplets are generated and segregated within the channel (He et al., 2005).

However, one universal aspect of microfluidic channels is the small scales and characteristic velocities, which means that these systems must operate within the low Reynolds number regime. While this provides some benefits, it also imposes constraints which require novel solutions to perform many types of common tasks. Specifically, I have discussed how fluid transport cannot be generated through many intuitive means, and the turbulent flow which often causes rapid macroscale mixing is absent. A large number of strategies for mixing within microfluidic channels have been proposed, based on passive and active schemes which each use various phenomena to generate mixing (Pamme, 2006). Furthermore, controllable pumping over short distances and in arbitrary directions may be an advantage of microfluidic pumping systems. As cilia are the design which natural has developed for the task of manipulating fluids at the microscale, an artificial structure which mimics cilia has been widely envisioned as an appealing device for producing these sorts of fluid motions.

3.6 Artificial Cilia On the Rise

The rapid development of microfluidic technology demands creative methods for manipulating fluids at the microscale, and the cilium is a nearly universal method with which biology performs such tasks. In addition, micro- and nanoscale sensors and actuators of many kinds have potential applications throughout nanotechnology. As such, just the last few years has seen a dramatic rise in the number of researchers investigating both experimental and theoretical aspects of artificial cilia and cilia-driven fluid flow. In this section I present brief overviews of alternative strategies for generating artificial cilia which have been recently demonstrated in the literature. Briefly, however,

I reference a few advantages and important differences which the biomimetic cilia arrays I have developed have with these other works, which will be discussed in more detail in Chapter 4.

There are assuredly more efficient ways to rapidly move fluids if the required dimensions of a pumping apparatus are not small. Many of the systems I describe below have at least one dimension which is in the hundreds of microns, and a few of these have demonstrated such pumping and mixing which is more rapid than that I will demonstrate. Of course, this is largely a matter of scale. Structures with larger characteristic lengths will, in general, produce larger characteristic velocities for a similarly scaled motion of the actuator. Several of these systems have been branded as artificial cilia, and that term has essentially come to mean a structure which manipulates fluids, more or less regardless of scale and shape.

This question of scale may have implications in the other direction as well. I have mentioned that diffusive motion can dominate driven advection if the advection is slow enough, as determined by the Péclet number. Thus, for an actuator to produce advective transport it must be large enough (or move rapidly enough) in order for its actuation to produce characteristic velocities large enough to dominate diffusion. I point this out in order to mention the possibility that the scale of biological cilia approaches the minimum size at which it is feasible to have advective transport dominate diffusion, a notion which I do not believe has been discussed in the literature. If this were indeed the case, then an artificial cilium at the size of its biological analogue may be, in some sense, as small as a mechanical pump (one which works from within the fluid and operates at reasonable frequencies) can be.

Based on these issues of scale, I emphasize the fact that I refer to my own system as *biomimetic*, rather than just artificial, cilia. This important distinction represents the fact that these biomimetic cilia arrays are the only demonstrated example of responsive

structures at the dimensions of biological cilia, in arbitrarily large arrays of cilia as seen in biological systems. Furthermore, of the publications mentioned below, the minority have actually demonstrated the controlled ability to manipulate fluids, as most of the papers are only reports of fabrication processes. It is the combination of these facts which allows me the unique opportunity to discuss experimental results in my biomimetic cilia systems within the context of biology, one of the fundamental thrusts I defined in the Introduction.

Aside from scale, the fabrication process I present in Chapter 4 has a number of other advantages over the other works I will describe below. The template based process I use does not require photolithography, a multi-step process which defines structures at the microscale based on the masked exposure of a photoresponsive material. Photolithographic processes, especially as the size of patterned features approaches 1 μm, can require expensive equipment and materials and is time-consuming, as often one must continually generate new devices either from a master which gradually wears out, or from scratch. In contrast, the template based approach can be done with inexpensive, commercially available components and requires several days to make the polymer composite, but only an afternoon to make a handful of samples. Secondly, the templates themselves are commercially available and so the ability to adjust parameters such as cilia diameter, length, and average density is straightforward. Lastly, the flexible magnetic/polymer composite used for biomimetic cilia is relatively easy to produce, and magnetic actuation in general is appealing for a number of reasons. These issues will be discussed in greater detail in Chapter 4, and so for now I turn to brief descriptions of a number of relevant works in the literature.

The following are presented in chronological order in order to portray the development of the field over time, as essentially all the work I will describe occurred in the last decade. It is worth noting that, upon the publication of the fabrication and magnetic

actuation of our biomimetic cilia in Nano Letters in 2007, approximately three publications had produced engineered structures which could be classified as artificial cilia. In contrast, in the most recent count a total of around 8-9 publications have presented artificial cilia or engineered structures derived for the same purpose. I present more details below, but Table 3.2 lists the most relevant of these processes and the critical dimensions and actuation strategies for a more direct comparison with my system.

Actuators and Artificial Cilia

Author	Year	Structure	Actuation	Dimensions (μm)	Fluid flow?
Tabata	2002	Gel pillars	BZ oscillation	150×100	no
Singh	2005	linked-bead	magnetic	$0.8 \times 25 - 75$	no
Darnton	2004, 2008	bacterial	ATP	0.2×15	mixing/pumping
Evans	2007	biomimetic	magnetic	$0.2 - 1 \times 10, 25$	no
Toonder	2008	paddles	electrostatic	$100 \times 20 \times 1$	mixing/pumping
Sidorenko	2008	hydrogel	swelling	$0.2 \times 5 - 8$	no
Fahrni	2009	paddles	magnetic	$300 \times 100 \times 15$	vortical
Oh	2009	paddles	stage oscillation	$400 \times 75 \times 10$	oscillatory
van Oosten	2009	liq. crystal	optical	$1,000 \times 200$	no
Vilfan	2009	linked-bead	magnetic	30×5	pumping

Table 3.2: Artificial cilia and related actuators which have been presented in the literature. Note that Evans et al. is the Nano Letters publication in which the biomimetic cilia fabrication and actuation methods presented in this thesis were reported.

3.6.1 Tabata et al. 2002

This work was based on the ability of some gels to spontaneously self-oscillate based on a chemical process known as the Belousov-Zhabotinsky reaction. This reaction causes alternating swelling and deswelling of the material which propagates through the gel in a wave. Low-aspect ratio pillars were molded at a height of around 150 μm, and as the wave propagated through the gel it induced small deflections in the pillars (Tabata et al., 2002).

3.6.2 Singh et al. 2005

This work exemplifies a class of publications which have developed various types of microdevices based on linking magnetic microbeads together into chains. In the presence of a magnetizing field, the dipole induced in each magnetic bead is aligned with the magnetic field direction. Nearby beads begin to attract each other, and because nearby dipoles have a preference for aligning head-to-tail, the beads are formed into chains. These chains are also aligned with the field, and so in solution the rotation of the magnetic field causes the rotation of the chains. Typically the beads are small enough to be superparamagnetic, and so removal of the magnetic field allows thermal effects to break apart the chain.

In the work of Singh et al., they demonstrated the ability to covalently link the beads to each other to form permanent chains, and then the chains were tethered to a glass slide within a microfluidics channel. The average length of the chains, which can be difficult to control when free in solution, was determined in this case by the the height of the channel. Once linked, changes in the external magnetic field causes deflections of the tethered chains (Singh et al., 2005).

3.6.3 Darton et al. 2004 and Breuer et al. 2008

Darnton and Breuer et al. demonstrated the development of 'bacterial carpets'. Flagellated bacteria were introduced into a channel and bonded to a glass slide, with their flagella sticking up into the fluid. In their 2004 work the group demonstrated that these beating flagella induced flows which appeared as an effective diffusivity, and showed that the effect decayed with distance above the flagella. The 2008 follow-up demonstrated that, by reducing the height of the channel to less than the length of the flagella, the flagella would be forced to beat in a direction which caused pumping down the length of the channel. One difficulty with each of these types of devices is that the

performance of the bacteria decreased over time as the replenishment of nutrients and removal of metabolic waste were not fast enough to keep the specimens viable (Darnton et al., 2004; Kim and Breuer, 2008).

3.6.4 Sidorenko et al. 2008

This novel actuator was based on the deflection of silicon nanorod arrays by the reversible swelling of a hydrogel layer at the base of the rods. Hydrogels are loosely cross-linked materials which can be mostly composed of water. They demonstrated actuation with two processes, one in which the nanorods were cantilevered and a second in which the tips of loose rods were embedded in the hydrogel. In both cases, sequences of dehydration and rehydration of the gel caused swelling and deswelling, which in turn caused deflections of the rods into striking, repeatable patterns (Sidorenko et al., 2007).

3.6.5 den Toonder 2008 and Fahrni 2009

These two publications represent a competing version of artificial cilia which is based on paddles $100-200\ \mu m$ wide and about $1\ \mu m$ thick. Den Toonder et al. demonstrated pumping and mixing in a microfluidics channel with arrays of bilayered paddles produced with photolithography. A thin conducting chromium layer was deposited onto a polymer paddle, and mechanical stress between the two layers caused the paddles to curl up. Once curled, an electrostatic potential was applied between the paddles and a backgate, inducing a charge in the thin chromium layer and forcing the paddle to unroll. The oscillatory motion of these paddles generated fast pumping and mixing because of their large size and rapid oscillation frequencies. However, it was noted that the underlying reason for the fluid flow was that the paddle motion was actually rapid enough for inertial forces to play a role, as the paddle motion would not generate flow at low Reynolds number. Because the unrolling of the paddle was slightly faster

than the rolling motion, the extra inertia generated net transport (Toonder et al., 2008; Baltussen et al., 2009).

Fahrni et al. (2009) demonstrated an analogous device at a slightly larger scale, but which was based on a magnetic/polymer composite. Paddle deflections were generated with external magnetic fields, and torsional motion of the paddles could be generated because the paddles were large enough to retain a remanent magnetization. It was demonstrated that this torsional motion could be used to produce vortical fluid motion around the paddle (Fahrni et al., 2009).

3.6.6 Oh et al. 2009

This device consisted of an array of polymeric rods which were each 400 μm in length. When placed onto a piezo-electric stage and within a fluid, the oscillatory motion of the stage generated a small amplitude oscillation of the tips of the rods. Near the body of the rods the fluid motion was oscillatory, but closer to the tips where the amplitude of the rod's motion was larger a slow upward fluid motion was observed (Oh et al., 2009).

3.6.7 van Oosten et al. 2009

This work was the first to demonstrate an artificial cilia system based on optical actuation. The device was built from liquid crystalline materials which could be inkjet printed at dimensions of about 200 μm wide and 1 mm long. Liquid crystals are polymers which can flow like a liquid but retain some degree of molecular orientation like a crystalline solid. The inclusion of an azobenzene unit into the polymer allows it to respond to irradiation by light. The light induces a change in the azobenzene which decreases the order of the liquid crystal, and the material responds by a shape deformation. In addition, they demonstrated cilia composed of multiple stacked polymeric

layers with photoresponsiveness at different wavelengths, allowing them to produce more complex bend shapes with multiple light sources operating independently (van Oosten et al., 2009).

3.6.8 Vilfan et al. 2009

Using an optical trap to assemble linked bead structures, Vilfan et al. demonstrated the bead-by-bead production of an array of nine cilia which were 30 μm in length by 5 μm in diameter. An external magnetic field was applied which caused the cilia to perform a beat similar to the tilted conical beat of nodal cilia, and they reported on the transport of four tracer particles in the flow. The extent of the flow was only over the roughly 60 μm width of the array. Although it was not discussed in the text, the four tracer pathlines, which I have displayed in Figure 3.11, also exhibited epicyclical motion similar to that I observe. In addition, the velocity profile above the cilia tips was reported for several different beat shapes and is also displayed in Figure 3.11. I note that this velocity profile will turn out to be quite different from that I will report on in Chapter 5, which I expect is a result of the small overall dimensions of their array (Vilfan et al., 2009).

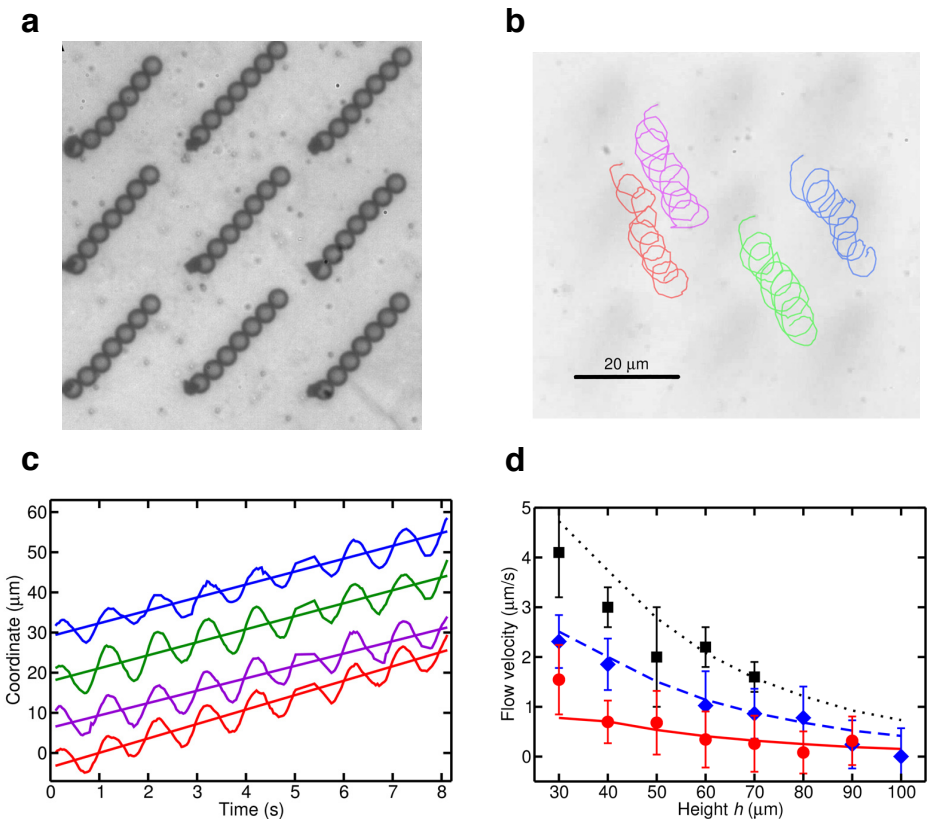

Figure 3.11: From Vilfan et al. (2009). Through the directed assembly of an array of nine linked-bead cilia, Vilfan et al. demonstrated short-range transport of four tracers over the width of the array, as shown in (b). (c) The radial displacement of the four tracers as a function of time, clearly showing small oscillations as well as an overall constant velocity represented by the linear fits. (d) Velocity profiles for several different beat shapes. The curvature in these velocity profiles does not match the results I will present later for long-range flow over large arrays of cilia.

Chapter 4

FABRICATION AND MAGNETIC ACTUATION

"Among those whom I could never persuade to rank themselves with idlers, and who speak with indignation of my morning sleeps and nocturnal rambles, one passes the day in catching spiders, that he may count their eyes with a microscope; another exhibits the dust of a marigold separated from the flower with a dexterity worthy of Leuwenhoweck himself. Some turn the wheel of electricity; some suspend rings to a lodestone, and find that what they did yesterday they can do again today. Some register the changes of the wind, and die fully convinced that the wind is changeable. There are men yet more profound, who have heard that two colorless liquors may produce a color by union, and that two cold bodies will grow hot if they are mingled: they mingle them, and produce the effect expected, say it is strange, and mingle them again."

- Samuel Johnson
From *A Dictionary of Thoughts*,
Tryon Edwards, (1908), pg. 243.

Many scientists will recognize the mentality, possibly with a cringe, which Samuel Johnson describes in this quote. It is understandable how an outside observer would find mundane the repetitious nature of science (as often even scientists do), yet the repeatability of experimental work is so fundamental that science would cease to be

science without it. However, in the world of nanotechnology the reproducibility of an experiment is not to be taken for granted. Repeating experiments at these scales can often be difficult, largely for the obvious reason that researchers are building and characterizing systems at scales many orders of magnitude smaller than the tools humans have traditionally been accustomed to.

For these reasons, the bulk of my work in the early stages of this thesis research focused on the development of robust, reliable methods for producing biomimetic cilia. Two desirable properties of such fragile microscale samples are, to an unfortunate degree, mutually exclusive. In order to be a responsive structure, the cilia must be flexible enough to be deformable under a reasonable application of force. Robust fabrication methods, on the other hand, are much easier to develop for structures with low deformability. Thus, the development of these methods was initially a great challenge. In the first part of this chapter I will describe the fabrication procedure which I have developed for producing biomimetic cilia arrays, as well as a number of issues which I have encountered and solved which are of use to the broader community as fundamental technologies for producing responsive microscale structures.

In the second part of this chapter I turn to the magnetic actuation of biomimetic cilia arrays with external permanent magnets. As structures engineered to be biomimetic cilia, a primary goal of this research was to mimic the beat shapes of biological cilia. Accurate mimicry of these beats requires magnetic geometries which maximize the applied force on a cilium in order to generate comparable deflections. However, the primary experiments of interest with these samples requires high magnification microscopy, in order to perform video-tracking of tracer particles in the flow. Thus, the actuation strategies I needed to devise must combine high magnetic forces with accessibility, another challenge which I will describe in this chapter.

Finally, controlled experiments in a well-defined magnetic field allowed for my work to confirm the accuracy of a novel energy minimization model developed by a colleague. This model predicts cilium bending in a prescribed magnetic field, and predicted for the first time the effect of a magnetic gradient on a cantilevered, flexible magnetic rod. One of the experiments I will describe in detail in this chapter confirmed the accuracy of this description, and also served as the first experimental demonstration of the actuation of such structures due to a magnetic gradient.

4.1 Magnetic Composite Materials

In the early years of the development of biomimetic cilia arrays within our lab, the primary role I played was to take a magnetic composite material and fabricate arrays of flexible rods which could be actuated with permanent magnets. As I discussed in the previous chapter, our successful demonstration of these structures at the scale of biological cilia would prove to be the first report of a true biomimetic cilium in the literature (Evans et al., 2007). However, the production of the magnetic composite and the basic idea on how to fabricate the cilia were developed by Lloyd Carroll, a post-doc in the lab, and Ben Evans, a fellow graduate student. The material they developed, which we refer to as FFPDMS, is the material which has formed the biomimetic cilia with which the rest of the results in this thesis were taken and which I will describe below. The full description of this material as well as a great deal of work on means for the surface functionalization of such materials can be found in Ben Evans' thesis (Evans, 2008). I briefly note, however, that the graduate student who succeeded Ben, Briana Fiser, has also worked on alternative materials with advantages over FFPDMS. One of these is the first development of a core-shell cilia actuator, which are arrays of flexible rods with some portion of the top of the rods encased in a shell of nickel. This type of biomimetic cilium contains a greater volume of magnetic material and

can thus be actuated with larger forces and deflection amplitudes. Such improvements may be critical to future biomimetic cilia research with viscoelastic fluids which mimic the airway mucus, but are much more viscous and thus impose increased drag on the motion of an actuator.

In all cases, a successful biomimetic cilium requires a combination of flexibility and the ability to respond to a an external stimulus with a deformation. The degree to which these two properties are found in a structure determines its responsiveness. A high degree of response is difficult to find in a homogeneous material. As such, nearly all the examples of cilia-like actuators in the literature involve composite materials. For example, even the linked-magnetic beads depend on the length of the covalent linkers between them to determine their flexibility (Singh et al., 2005), and the liquid crystal artificial cilia are severely limited in the types of motion they can exhibit without being formed into composites of two polymers (van Oosten et al., 2009).

The composite which has been primarily pursued in our lab is a dispersion of magnetic nanoparticles into a flexible polymer. Many types of nanoparticle-based composites have been demonstrated in the literature, and in nearly all cases a major difficulty is to prevent the formation of large aggregates of particles. To produce a material which is homogenous at nanometric length scales requires even more care. The magnetic composite paddles of Fahrni et al. are large enough that aggregates were not a major problem, although they do report that their technology is not currently scalable due to this issue. In the case of a biomimetic cilium, relatively homogenous composites are a prerequisite because the final structures will be smaller than 1 μm in diameter.

These issues have been overcome in our lab by the development of a composite of iron oxide nanoparticles dispersed into polydimethylsiloxane (PDMS), a silicone elastomer which is widely used in the microfluidics community. The iron oxide nanoparticles were produced by the co-precipitation of ferric chloride ($FeCl_3$) and ferrous chloride ($FeCl_2$)

into a ferrofluid, a stable aqueous suspension of the nanoparticles with fascinating liquid and magnetic properties. In order to mix this with the PDMS pre-polymer, which is hydrophobic, requires that the ferrofluid be converted to an organic solution. This is done by transferring the nanoparticles to an oil phase, repeated sedimentation with a magnet and rinsing with ethanol, and then resuspending the nanoparticles into an organic solvent.

The dispersal of the ferrofluid into PDMS results in the composite material we call FFPDMS. To properly disperse the particles, the ferrofluid and pre-polymer are each diluted in toluene and a small amount of hexadecane, then combined over an hour or more under ultrasonication. The excess toluene, which is more volatile than the hexadecane, is evaporated away to leave behind a dark, pasty suspension of the nanoparticles in the PDMS pre-polymer. The small amount of hexadecane remains to keep the suspension stabilized and prevent it from drying out. This method has successfully produced a nicely homogenous, composite material with a magnetic loading of up to 5% by weight. For the full details of the development and characterization of FFPDMS and other alternative magnetic-polymer composites I again refer the reader to Ben Evans' thesis (Evans, 2008).

4.2 Template Fabrication

The basic template fabrication process for biomimetic cilia proceeds as depicted in Figure 4.1. The templates which I use are purchased commercially from it4ip, a Belgian company which produces custom orders of polycarbonate track-etched (PCTE) membranes. PCTE membranes are conventionally used as filters in purification systems. As such, most commerciallly available filters seek to provide a constant flow rate in filters with varying pore diameters. For this reason, other PCTE suppliers, such as Whatman, maintain roughly equal flow rates by increasing the density of pores as the

pore diameter is decreased. For sub-micron pores, this density increase results in a meshwork of pores which are interconnected in many places, which would produce a network of fibers if templated. In addition, the pores in many PCTE membranes are oriented haphazardly. In contrast, a good template for my purposes should be at a density which minimizes the number of pores which intersect with each other, and with pores which are oriented perpendicularly to the membrane surface. These conditions are met by another commonly used type of nanorod template, anodized alumina oxide (AAO) templates, but it is only possible to produce pores in AAO at higher pore densities than I have had success with in PCTE membranes.

One of the key developments in the fabrication process for biomimetic cilia was when our lab became aware of the PCTE membranes which could be custom ordered from Belgium. Prior to this, our method had been restricted to pores at a low density to avoid interconnected pores, which from Whatman necessarily meant pore diameters of 2 μm or larger. The resulting fat, stubby structures were poorly responsive, although I was able to actuate these structures by driving an external fluid flow across the array. The PCTE templates from it4ip could be ordered with custom pore diameter, custom membrane thickness (which translates to cilium length), average pore density, and nicely parallel pores oriented at any angle relative to the membrane surface.

I briefly note that I will refer to the average cilia density of my samples throughout this thesis. The manufacturing process for track-etched membranes is to expose the solid membrane to a source of ionized atoms. As the ions pass through the membrane, they leave a very narrow track behind in which the membrane material has been degraded by the passage of the ion. In the conventional manufacturing method (used by Whatman and others), this irradiation is by a nondirectional source and so the particle tracks are randomly positioned and randomly oriented. In the custom membranes, the tracks are generated by placing a solid polycarbonate membrane in the path of

a particle accelerator's beamline, and so the source is highly directional. This means the tracks can be oriented as desired relative to the surface of the membrane. The pores are then parallel to each other, but the position of the pores is still randomly distributed, and so the average density is all that can be defined. While there are numerous practical reasons why a regular array of cilia would be useful, I note that the random array likely makes for a more appropriate comparison with biological systems. However, adhesion issues between nearby cilia have thus far prevented me from even approaching the nominal density of cilia in the airway. Nodal cilia, as they are primary cilia, are found one per cell and are thus at a much lower density which roughly matches the average density in my biomimetic samples.

Another important period in the development of the fabrication process was my discovery that the pore diameters could be further customized after receiving the membranes from the manufacturer, allowing me to easily tune the diameter of the cilia in my arrays. This parameter space was important to explore because the robustness of the process and the fragility of each cilium is highly dependent on its flexural rigidity, which goes as the diameter to the fourth power. As I discussed, the inverse of this relationship also determines the responsiveness, and so smaller diameter rods are more susceptible to destructive forces, but will be more responsive to a magnetic force if they can be successfully fabricated at that diameter. Thus, it was important to determine an optimal parameter space which would provide the necessary responsiveness while maximizing the robustness of the process.

The pores are originally formed from the ion tracks when the manufacturer exposes the membrane to a mild etchant, typically 4M sodium hydroxide. The ion's track is etched at a significantly larger rate than the bulk, and so when placed into the etchant, the pores are etched to larger diameters with little change in the membrane thickness. This process is how the original pore diameters are defined by the manufacturer, but

in our lab I demonstrated that the diameters could be predictably enlarged by further etching after being purchased. Thus, I typically ordered PCTE membranes with pores of 200 nm diameter, and etched the pores further to make larger cilia.

Once a template has been selected, impregnation of the pores with FFPDMS is accomplished simply by dipping the membrane into the FFPDMS. Although the material is quite homogenous, to avoid any potential aggregates I typically ground a small amount of the FFPDMS with a mortar-and-pestle prior to dipping the membrane into the composite solution. After filling the membrane a critical step is to gently, but thoroughly clean any excess FFPDMS from the surfaces of the membrane. Without this key step, the cilia are unlikely to be well bound to the substrate layer, and microscope optics are severely deteriorated by any thin film of the dark FFPDMS. Finally, excess FFPDMS chunks can float around in the liquid in which the cilia are beating, and the actuating magnet can move these chunks in ways which move the fluid dramatically, overcoming any effect of the cilia. Furthermore these chunks can actually collide with the cilia and flatten them or shear them off the surface.

Another important note is that the FFPDMS solution does not contain the platinum-based catalyst required for PDMS crosslinking. Before placing the membrane within the well, the membrane is therefore dipped into a small amount of regular PDMS pre-polymer which has been already been mixed with the catalyst. It has been my assumption that the catalyst can then diffuse into each cilium to allow for crosslinking, and I have seen no evidence that this is not the case.

The membrane, encased in the regular PDMS, is then placed into a well which is also formed from PDMS, and which will later allow the fluidic chamber to be enclosed. This seals the sample to ensure that the cilia do not dry out, as well as to minimize fluid flow due to other sources besides the cilia beat, such as evaporative drift. The entire sample is then placed into a convection oven at 80° in order to crosslink the PDMS

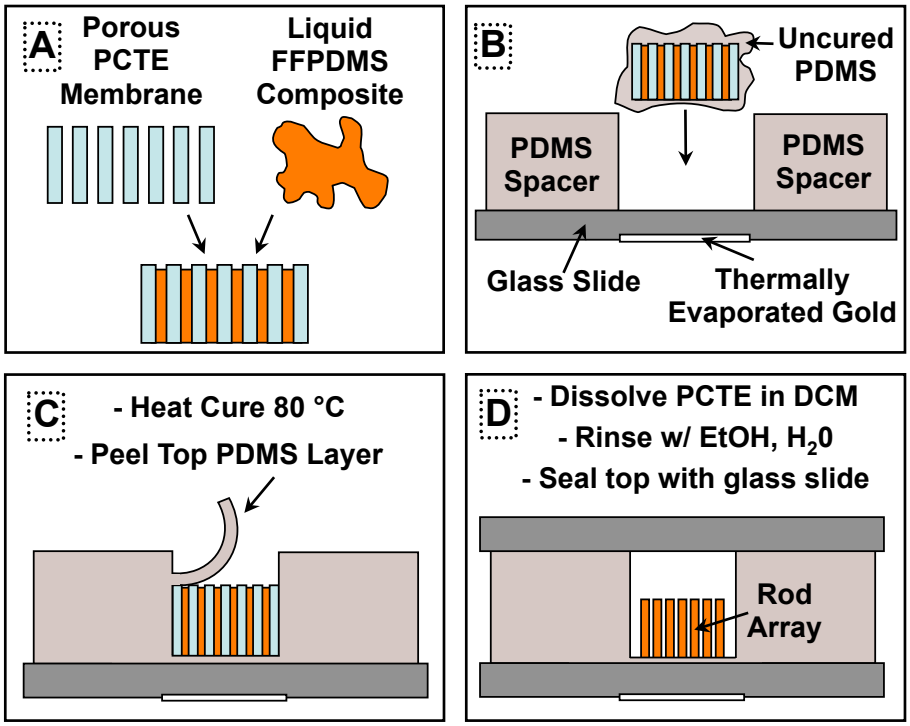

Figure 4.1: The basic procedural steps for the template fabrication method I use to generate biomimetic cilia. The FFPDMS composite is introduced into the pores of a polycarbonate track-etched membrane, the membrane is placed onto a substrate within a PDMS well, and the PDMS is heat cured in a convection oven. After curing, peeling the top layer of PDMS exposes the polycarbonate membrane, which is dissolved with dichloromethane to release the array. The thermally evaporated gold in panel (B) provides a reflective surface, one which is integrated into the sample, and which allows for imaging with a reflectance microscope. The ability to generate large magnetic forces, and thus large cilia deflections, requires magnets in close proximity to the array, and the integration of the reflective surface into the sample is one of the means by which the total sample thickness was minimized to facilitate both large magnetic forces and close approach of a microscope objective from opposing sides of the sample.

into an elastomer. Although PDMS by itself will cure within one hour, in a few cases I have seen evidence that the composite may take longer to cure, and so I typically leave samples in the oven overnight to ensure full crosslinking.

The crosslinked cilia samples are then ready to be freed from the membrane, which is done by dissolution in dichloromethane (DCM). This step is conceptually simple as the polycarbonate is susceptible to dissolution by a number of organic solvents. In truth, the ability to dissolve the membrane without significantly damaging the sample required months of iterations of the fabrication process, and while there were early indications that sub-micron diameter cilia would, in fact, be possible to actuate, the experimental repeatability disdained by Samuel Johnson was initially a major problem. For that reason, I momentarily digress with some specifics of the development of a robust fabrication process.

4.2.1 The key to a robust fabrication process

In collaboration with Ben Evans, I pursued multiple routes for dissolving the polycarbonate membrane in order to release the cilia array, which I will describe momentarily. First I note what eventually became the simple key to reproducibly fabricating biomimetic cilia. Our early thoughts had been that, because the cilia were so fragile, we needed to dissolve the membrane in a manner as gentle as possible. As it turns out, this approach is, in some sense, precisely wrong. As the membrane begins to dissolve it becomes like wet toilet paper. It loses its structural integrity, breaks apart into chunks, and eventually is washed away and completely dissolved. What became the key to fabricating cilia was to make this process happen *as quickly as possible*.

The first artificial cilia which I generated were fabricated within a microfluidics channel. These were, as I have mentioned, cilia fabricated within Whatman templates which were restricted to diameters of 2 μm. These structures were truly pillars and not

cilia, and it was relatively straightforward to dissolve the membrane simply by flowing a solvent through the channel (at that time I used toluene). The microfluidics channel also allowed me to easily observe the sample under the microscope while the membrane was being dissolved, and the pillars could be deflected by application of a fast fluid flow. I note that this is a proof-of-concept of the idea that artificial cilia could act as a flow sensor which provides highly local information about fluid velocity, without the need to add tracer particles into the fluid. It was at this same time that it was becoming clear that renal cilia were performing a critical flow sensing function in the kidney. However, on only a very few occasions did we observe actuation of a pillar in an applied magnetic field, and those few cilia were typically suspected of being loosely bound to the substrate.

The issue of responsiveness to a magnetic field was resolved with the discovery of the custom polycarbonate membranes. I had observed that the 2 μm pillars were indeed magnetic when they were loose in solution, and the smaller diameters would affect the stiffness of the cilia much more than the reduction in volume and corresponding reduction in applied magnetic force. However, upon receiving the new templates it was quickly realized that these smaller cilia were much more susceptible to collapse and shearing off of the surface by the forces generated as the membrane was dissolved.

An alternative to fabrication within a microfluidics channel is the procedure which I have already described and is depicted in Figure 4.1. The cilia are built within a well, and the membrane is dissolved in a vial of DCM heated near to its boiling point. This method causes the membrane to be rapidly dissolved for two reasons, most obviously because of the added thermal energy of the heated solution. However, the other reason is implied by the Reynolds number. In the microfluidics channel the Reynolds number is very small, and so the flow of fluid which is dissolving the membrane is laminar. This dramatically increases the time it takes for the membrane to dissolve, giving any

sloshing of the partially dissolved membrane all the more time to wreak havoc on the cilia. In contrast, the vial is easily large enough to support turbulence if the solution is gently mixed. This leads to faster dissolution times, and, when proper care is taken, correspondingly more reliable sample fabrication.

The successful development of this fabrication scheme allowed me to produce arrays of biomimetic cilia which were the first cantilevered nanorod arrays in the literature to approach the size of biological cilia with a material flexible enough to be actuated. A number of electron micrographs of these structures are shown in Figure 4.2, along with a single image of biological cilia for comparison.

4.2.2 Minimizing sample thickness

With practice, this fabrication procedure is a fairly straightforward means for producing biomimetic cilia. Another challenge which I have alluded to was the need to make the samples as thin as possible. This was necessary for two different accessibility reasons. First, I must be able to apply large magnetic forces to the cilia, which generally means that I want to place a magnet as close as possible to the array. Second, I must simultaneously be able to image the array with a microscope objective of at least 50x magnification. Without specialized objectives, such magnifications typically require that the desired focal plane be within a few hundred microns of the top of the objective. Thus, I needed to be able to get close to the cilia array from both directions simultaneously, which requires that the entire sample thickness be minimized.

The first approach for doing this is simply to utilize reflectance microscopy, in which the optical path passes through the sample as normal, but is then reflected, traverses the sample again, and is guided to the camera/eyepiece. This allows a magnet to be placed directly on the opposite side of the sample from the objective, blocking what would be the optical path of a transmission microscope.

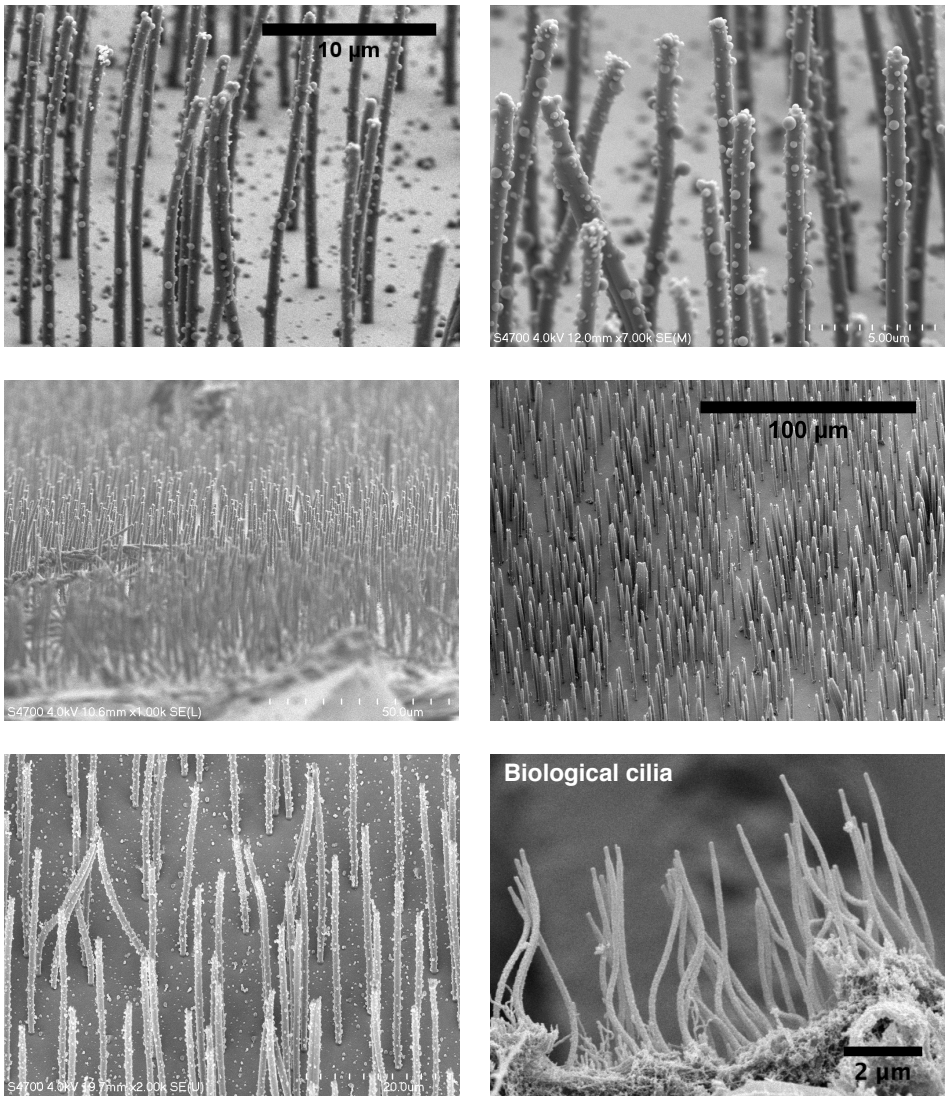

Figure 4.2: A collection of scanning electron micrographs of biomimetic cilia, except in the lower right, which shows biological cilia from the airway for comparison (courtesy of Jerome Carpenter). The biomimetic cilia are each in the range of 700 $nm - 1$ μm. I have fabricated and actuated cilia down to 200 nm in diameter, but smaller diameter cilia are much less likely to survive the critical point drying process required to dry the sample before imaging.

The second primary development of relevance to this issue was the realization of how to minimize the thickness of the substrate layer of PDMS below the cilia. I have not described it, but in my early efforts I took advantage of a useful property of PDMS in order to build the cilia on a substrate. This property is simply that when PDMS cures in contact with another already-cured block of PDMS, the two form a monolith with no discernible boundary. Thus, the first samples were made by dipping the membrane into uncured PDMS and placing this onto a previously cured thin film of PDMS, which is itself bound to a glass slide. The PCTE membrane and uncured PDMS surrounding it would then bond to the thin film as the cilia array was cured. The entire sample would then be placed into a larger well, which was sealed after dissolving the membrane.

A simple improvement to this original strategy was made by cutting out the center of the thin film of PDMS, and to actually use the cut-out region of this substrate layer as the fluidic chamber. In this case, when the PDMS-dipped membrane is placed into the well, it is placed directly on the glass slide in the center of the well. I then carefully ensure that the uncured PDMS spreads across the floor of the well until it contacts the walls of the well, so that this extremely thin layer will bond to the well and hold the entire sample down onto the glass. If this is not done then the membrane will release from the glass when it is dissolved. This key step means that the entire sample thickness is equivalent to the thickness of the well plus two glass coverslips, which allowed me to fabricate samples with a total thickness of about half a millimeter.

4.2.3 Ground and lateral collapse of high-aspect ratio structures

As I have mentioned, the fragility of the cilia is one of the main difficulties in reliably fabricating arrays. Nearly all microscale, high-aspect ratio structures suffer from such difficulties, and so several models for the collapse of high-aspect ratio structures have

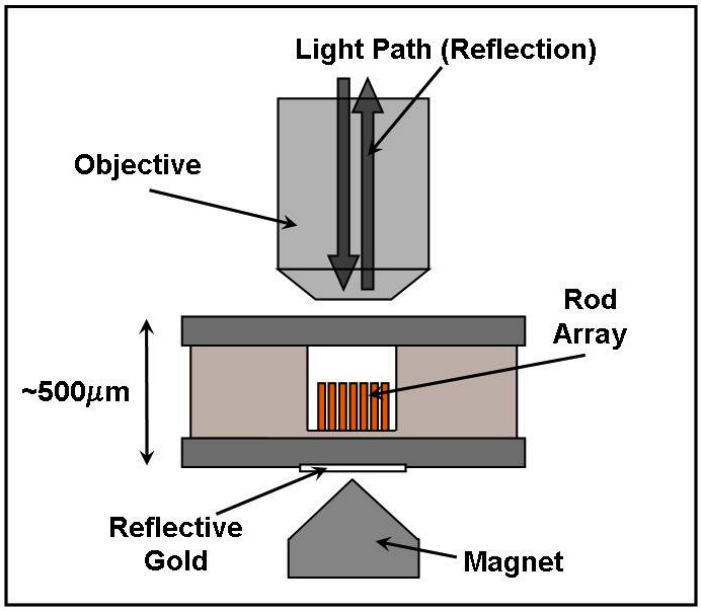

Figure 4.3: The actuation setup used to simultaneously image in reflection mode and apply large magnetic forces.

been published to better understand the mechanisms of collapse. When such structures collapse they can do so through one of two means. Ground collapse is, as it sounds, the collapse of a structure until it contacts and sticks to the substrate. Similarly, lateral collapse is the term used for the adhesion between neighboring structures which are not completely ground collapsed. The reason for both types of collapse is that the elastic forces which would try to upright a bent rod are dominated by surface adhesive forces. The strength of these adhesive forces depends on the surface energy of the material and its affinity for the liquid environment. PDMS is somewhat hydrophobic, and so when placed into water the PDMS surface energy can be minimized if it is in contact with another PDMS surface, rather than with water. Thus, when two cilia touch or one cilium touches the ground, these adhesive forces can be stronger than the elastic forces within the cilium, and so the collapsed state is thus stable.

These models can be made quantitative by balancing the two forces as demonstrated by Roca-Cusachs et al. (Roca-Cusachs et al., 2005). The models are described in

terms of the critical aspect ratio at which structures become unstable and are prone to collapse. For lateral collapse the critical aspect ratio is

$$\frac{L}{d} = \left[\frac{3^3\pi^4}{2^{11}\left(1-\nu^2\right)}\right]^{1/12}\sqrt{\frac{s}{d}}\left(\frac{Ed}{W}\right)^{1/3} \tag{4.1}$$

and for ground collapse it is

$$\frac{L}{d} = \frac{\pi^{5/3}}{2^{11/3}3^{1/2}}\left(1-\nu^2\right)^{-1/6}\left(\frac{Ed}{W}\right)^{2/3} \tag{4.2}$$

where L is the cilium length, d is diameter, ν is Poisson's ratio, s is the lateral distance between structures, E is the Young's modulus, and W is the work of adhesion of the material to itself. Using approximate values for the material properties of PDMS reveals that the critical aspect ratio for lateral collapse, the collapse which occurs most easily, is on the order of $L/d = 10$ (Evans, 2008). The fabrication method I discussed allows for structures to be produced and actuated with aspect ratios of up to 125. This points out the reason for the care needed during fabrication, as it means that the cilia I typically fabricate are not stable. If they come into contact with each other they are likely to stick, and so the fabrication process must avoid contact between cilia. The lower left panel of Figure 4.2 portrays an excellent example of the type of lateral collapse which is typical. In Figure 4.4 I display several more SEM images which feature more spectacular versions of cilia collapse, and which also emphasize the flexibility and corresponding fragility of these structures.

4.2.4 Fabrication of cilia within a fluidic cell

The fluidic experiments which I discuss in Chapters 5 and 6 require a well-controlled fluidic cell with a known geometry in order to properly interpret the results. In all experiments I completely enclosed the fluidic cell by placing a glass coverslip over the

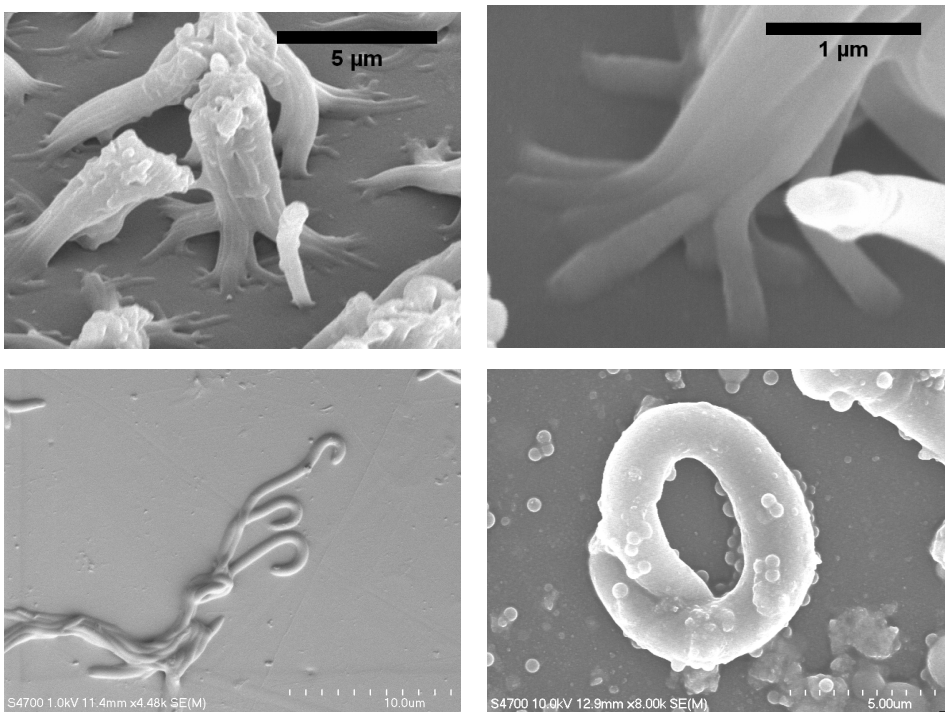

Figure 4.4: Examples of extreme collapse events. In the top row, the 200 nm diameter cilia have collapse into bundles which collapsed into larger bundles, demonstrating an interesting hierarchical structure. In the bottom row the cilia are essentially ground collapsed, but these two images also emphasize the flexibility of these structures.

well and sealing it with an optical adhesive, mainly to prevent any evaporative drift of the tracer particles in the fluid. In addition, care was always taken to prevent bubbles within the fluidic cell, since these also allow fluid to evaporate into the bubble, as well as changing the nature of the cell's geometry due to the presence of an air-liquid interface.

The shape of the well was carefully designed into a rectangular prism. The width of the well was typically on the order of 1 mm, and the height of the fluidic cell was typically $200 - 300$ μm. This means that the width is significantly larger than the height, and so cilia-driven fluid flows could be measured at distances from the lateral walls which were larger than the height. This ensures that wall effects are minimized, and my observations have been that the flow field is largely constant over the width of the flow cell.

4.3 Magnetic Actuation

In this section I turn to the magnetic actuation of biomimetic cilia arrays. As I described in the last section, the development of the fabrication process required a large number of iterations. In the early days of the struggle there were many times that only a single cilium, or maybe a few, would respond to a magnetic field with a slight twitch. While these were initially exciting successes, it took some time before the combination of robust fabrication and effective actuation schemes produced actuation of respectable arrays of cilia. A prime example of cilia actuation is animated in Figure 4.5. The poster image for this animation introduces the method I will use several times in this thesis to display cilia motion in a still image, which is to generate a minimum intensity projection of a single beat cycle from the video. This projection is a single image which superimposes the cilia positions at multiple time steps onto a single frame, revealing the shape of the beat.

To outline this section, I begin with an overview of the types of magnetic forces

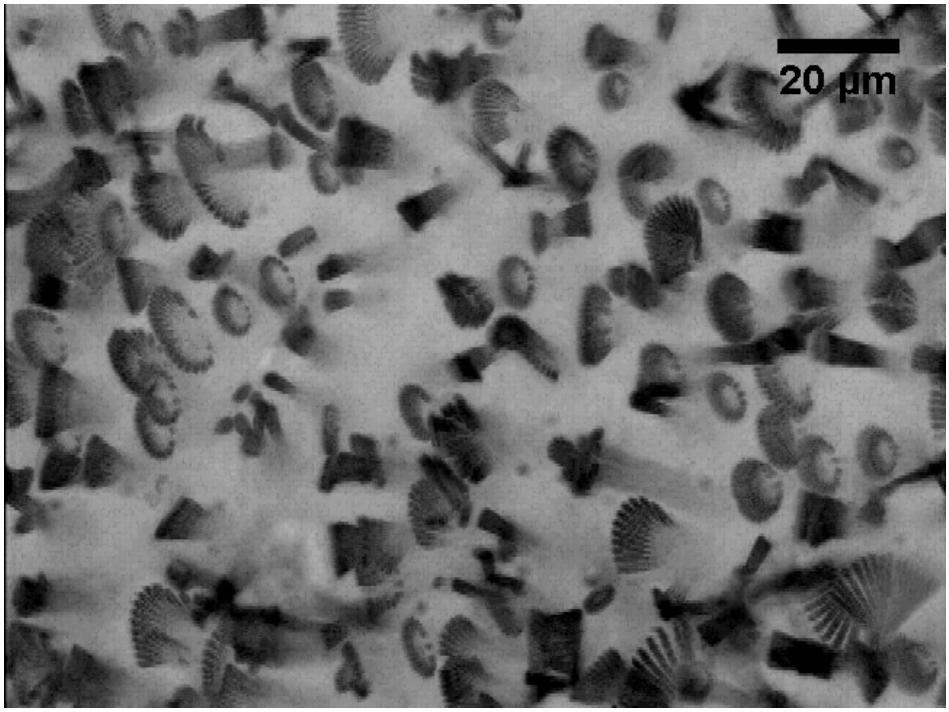

Figure 4.5: Click to Animate. The magnetic actuation of a typical biomimetic cilia array mimicking the tilted conical beat of embryonic nodal cilia (the cilia in the image are tilted towards the left). The poster image is a minimum intensity projection over a single beat cycle, revealing the position of each cilium as a function of time in a single composite image.

which can be applied to a magnetic rod, and summarize an energy minimization model which Ben Evans developed to predict cilia bending in a known magnetic field and field gradient. Next I turn to a description of an experiment I devised in order to test the predictions of the model. Finally, I will describe strategies for mimicking the beat shape of various types of biological cilia.

4.3.1 Magnetic forces and an energy minimization model

Magnetic forces are appealing for actuation at the microscale because they are easy to generate via electromagnets or permanent magnets, which are especially advantageous as they require no power to generate the field. In addition, magnets are cheap and easily available, and the effects are long range so that the magnet need not be integrated into the sample. Magnetic forces also offer a level of complexity which can give rise to novel and useful types of movement based on the fact that there are two basic mechanisms by which magnetic fields generate force. This is because, as opposed to scalar fields like the gravitational force, magnetic fields are vector fields and have both a direction and a magnitude.

The magnetic force which we are most intuitively familiar with is the attraction and repulsion of two ferromagnets based on whether the magnets are lined north pole to south or vice versa. This force is actually an effect of the way the magnetic field changes through space, or the gradient of the magnetic field. At the microscale it is difficult for objects to retain a magnetization due to the randomization of magnetic dipoles caused by thermal effects. Thus, at these scales objects are not typically ferromagnetic and a repulsive force is rare. Instead, superparamagnetic objects are magnetized by an external field, and the magnetic field can then induce both a torque and force on a magnetic dipole.

The torque on the dipole is given by

$$\vec{N} = \vec{m} \times \vec{B} \tag{4.3}$$

where $\vec{m}$ is the induced dipole moment and $\vec{B}$ is the magnetic field. This equation implies that the torque acts to align the dipole with the field, since the cross product gives zero if the two vectors are parallel. Thus, induced dipoles will align with field lines in the absence of another force. However, the dipole also experiences a force which is determined by the gradient of the magnetic field, not its direction, as I just described. This force is given by

$$\vec{F} = \nabla(\vec{m} \cdot \vec{B}), \tag{4.4}$$

and the dipole will thus move to a local maximum in the magnetic gradient. As the gradient is typically maximized near the edges of a permanent magnet (or more specifically, places where the magnetic field direction changes rapidly), the effect of the gradient on an induced dipole is nearly always to attract it towards the magnet. Thus, the magnetic field induces the dipole moment, but once induced, the field can only work to rotate the dipole, while the magnetic gradient can pull on it.

Thus far I have limited the discussion to a single dipole. In the case of rod-like structures like cilia there are additional effects which must be considered. Specifically, when two induced dipoles are nearby each other the dipoles can interact with each other as well. As each creates its own magnetic field, the torque and force are minimized when the dipoles are aligned head-to-tail with each other. In an object with some aspect ratio, the interactions between dipoles are minimized if the dipoles try to line up head-to-tail along the long axis of the rod. Thus, a torque on the rod is induced if there is a discrepancy between the long-axis of the rod and the direction of the local magnetic field. The dipoles will attempt to align head-to-tail, but also try to align with

the magnetic field, and the combination produces a torque on the rod which results in a deflection. This deflection reduces the misalignment between the long-axis of the rod and the magnetic field direction.

I have considered only magnetic effects which would seek to actuate a cilium. Elastic forces within the cilium would then work to minimize the deformations caused by the magnetic forces. Based on these effects, Ben Evans developed a quasi-static energy minimization model which can predict the amplitude of deflection of a cilium in a known field and field gradient (Evans, 2008). Prior to the publication of this model in the literature, a number of other magnetic actuators had inspired early models which only incorporated the effect of the magnetic field to deflect a magnetic rod. Generally this is because the effects of a gradient to pull on a dipole are relatively small unless in an area of exceptionally large gradient, and so no experimental systems had demonstrated gradient bending and it was not necessary in the models.

As the fabrication process I developed was successful in producing some of the most responsive microscale structures in the literature, it was conceivable that our system could respond to the gradient and so Ben developed a new model which took this effect into account for the first time. To summarize this model, it broke the internal energy of a cilium into three parts: the elastic energy, a 'field energy', and a 'gradient energy'. The field energy is the component of the internal energy which is generated by application of a field, and refers to the competition between the internal dipole's desire to line up with both the field direction and the long axis of the rod. The gradient energy is the effect of the magnetic gradient which pulls the center-of-mass of the object towards the magnet. Using the angle definitions shown in Figure 4.6, Ben showed that the total energy of the rod is given by

$$U_T = \frac{\pi}{2}\frac{Er^4}{L}\phi^2 - \frac{\mu_0}{4}\frac{m^2}{V}cos^2\left(\psi - \phi\right) - \frac{1}{2}m\nabla BLcos\left(\psi' - \phi\right) \tag{4.5}$$

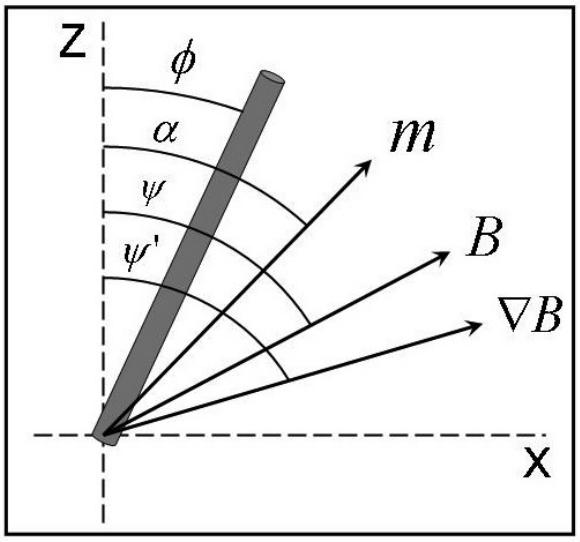

Figure 4.6: The definitions of the angles used in the energy minimization model of equation 4.5 between the rod, the magnetic moment m, the magnetic field direction B, and the magnetic gradient ∇B.

where V is the volume and the magnetic moment m is generally a function of the applied field strength B. The first term here is the elastic energy, the second is the field energy, and the third is the gradient energy. The rod position ϕ which minimizes U_T is the predicted deflection of the rod based on the properties of the material, the dimensions of the rod, and the magnetic field and field gradient.

As the third term, the gradient energy, is only dependent on the magnitude of the gradient and the properties of the cilium, it is the effect described by this term which has not been included in any previous models. In order to test the effect of the gradient it is necessary to prescribe a magnetic field which has an area of large magnetic gradient in which to place the cilia array. Furthermore, as the field bending cannot be separated from the gradient bending, the geometry of the field must be such that the field bending and gradient bending drive the cilium in opposite directions so as to be able to discern the two effects.

Fortunately, a magnetic field with this shape is trivial to generate as it is precisely the field which emanates from the pole of a magnet, as depicted in Figure 4.8a. At

points sufficiently close to the pole of such a magnet, the magnetic field direction always points away from the pole, while the direction of the gradient is always pointed towards the pole. Passing this type of magnet below a cilia sample should then allow me to determine which effect dominates, based on the direction the cilium is deflected. Of course, it is also important that the magnitude of the gradient be large enough to dominate. As I mentioned, magnetic gradients are typically large near edges, and so the conventional way to generate large gradients is to make sharp points towards which the field lines rapidly converge. It is for this reason that I chose to use the sharp-tipped magnet in Figure 4.8a, which was built from a machined piece of of iron placed onto a cylindrical magnet. All the permanent magnets used in this and other experiments were rare-earth, neodymium-iron-boride magnets obtained from K&J Magnetics.

The results of this experiment to test the effects of a gradient are displayed in the animation in Figure 4.7 and quantified in Figure 4.8. The agreement between the predictions of the model and the measured cilia deflections is confirmation that the model accounts for the effect of the magnetic gradient which had not been previously considered. In addition, the experimental demonstration of gradient-induced bending of a cantilevered microstructure was the first in the literature. The rapid switching of the cilia caused by the sudden dominance of the gradient over the field could be a means for using the cilia as a type of magnetic switch or gradient sensor. Finally, I note that while this model can account for novel features which have not been previously predicted, it is not able to predict the shape of a bent cilium in a magnetic field as it assumes the rod remains straight. For a more precise model which discretizes a cilium into sections, each of which can independently attempt to minimize its total energy, see Ben's thesis (Evans, 2008).

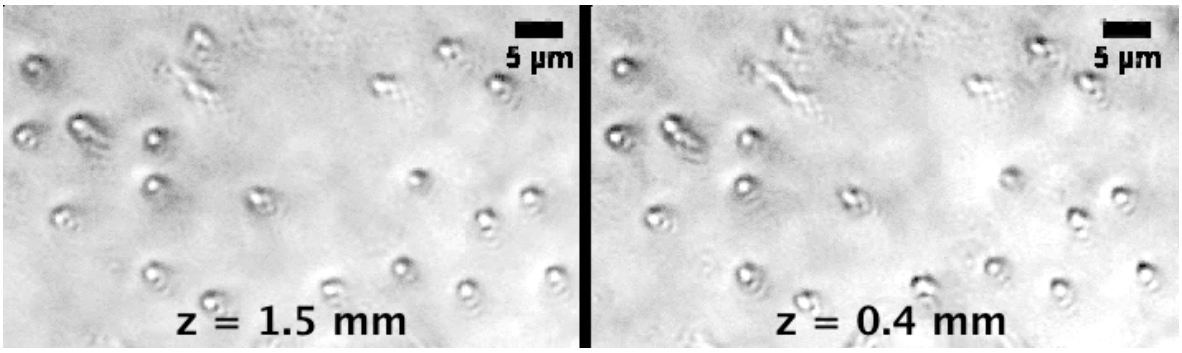

Figure 4.7: Click to Animate. A magnet which induces gradient and field bending in opposite directions is passed below a cilia sample at two constant heights (also see Fig. 4.8). At left, when the magnet is held at a constant distance of 1.5 mm below the cilia the deflection is a smooth, monotonic change in deflection angle (open circles below). In contrast, moving the magnet closer (to 0.4 mm separation) places the array in a magnetic gradient strong enough to overcome the field bending effect, which results in a rapid switching of the actuation direction. This was the first experimental demonstration of the gradient-induced bending of a cantilevered microscale structure in the literature.

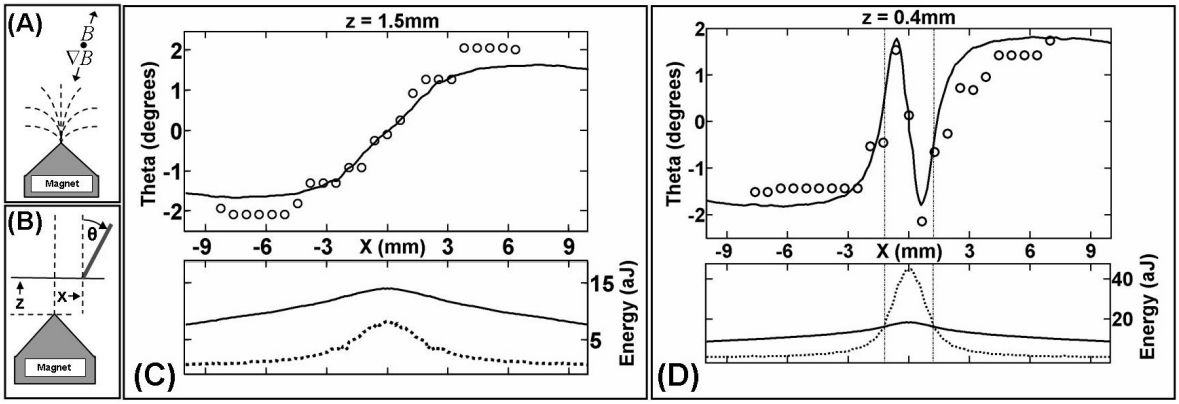

Figure 4.8: The experimental data demonstrating gradient-induced cilia bending. The magnet depicted in (A) is passed below the sample at a constant separation z, and the field geometry means that gradient bending and field bending are in opposite directions. (C) When the magnet is far from the sample the bending is purely field bending and the cilium always points away from the magnet. (D) In contrast, when the magnet is moved much closer the gradient energy grows larger than the field energy, and the cilia deflection rapidly switches towards pointing at the magnet. When the magnet moves past the sample the deflection reverts to the same behavior as field bending. In (C) and (D) the solid curves are predictions from the model (equation 4.5) and the open circles are measured deflections from the animations shown in Figure 4.7. This phenomenon could be used as a rapid means of switching the cilia beat with a small change in magnet configuration and positioning.

4.3.2 Mimicking the beat of biological cilia

While the previous section demonstrated a novel bending mechanism, the magnetic field geometry used for that experiment is poorly suited for most practical circumstances. Gradient bending requires very large gradients, which in general can only be found very close to a magnet edge. Thus, with permanent magnets it is difficult to produce stable, predictable beat shapes with a gradient. On a related note, the field bending produced by this same magnet is also non-ideal. For field bending, the field energy term in equation 4.5 is a function of the magnetic moment of the cilium (which is a function of field strength) and of the relative orientation of the field direction and the long axis of the cilium. As this orientational relationship is a cosine, the field-bending energy is minimized when the cilium aligns with the field. Inversely, then, the maximum force is applied when the two orientations are perpendicular. Thus, to maximize deflections a general design principle is that the field strength should be large enough to saturate the magnetization of the cilium while simultaneously the field direction should point perpendicular to the cilia (or parallel to the sample floor).

The magnetic field direction near a magnet's pole is essentially normal to the magnet's surface, and so in general to get the pole of a magnet very close to the array (large field strengths) means that the force generated will be zero, because the field direction is parallel to the undeflected cilium. Thus, I typically configure actuating magnets such that the dipole is oriented parallel to the sample floor in order to maximize cilia bending.

With this in mind, I outline the strategies I have developed for mimicking the two main classes of motile cilia. I remind the reader that airway epithelia cilia, and most other motile, $9 + 2$ cilia, are believed to oscillate largely within a single plane and therefore execute a planar beat. Nodal cilia, in contrast, perform a rotational beat around a tilted axis.

The planar nature of the airway cilia beat is easily duplicated. While one way to generate this beat is with a simple one-dimensional oscillation of a magnet, in principle this is slightly more difficult to generate than a rotational motion, which is easily generated by connecting magnets to the pivot of a variable frequency motor. To get a planar beat, then, a magnet must be placed onto a radial arm which extends out from the axis of rotation of the motor. When this is the case, even though the magnet path is circular, in the vicinity of the cilia sample (which is only about 1 mm on a side) the magnet path looks approximately linear. By placing a set of magnets onto radial arms a significant cilia beat frequency can be generated with a relatively slow motor speed. In addition, this type of actuation can also produce what Ben Evans referred to as a 'snap-beat'. In this configuration, even for a constant rate of rotation of the magnet, the cilia beat cycle is two phased and consists of a fast stroke (the snap-beat) and a slow stroke. To some degree this biphasic behavior mimics the effective and recovery strokes of biological cilia. However, as I have mentioned the two phase beat of airway cilia is accompanied by significant differences in the contour of the cilium, as well as a velocity difference.

Furthermore, as I discussed in Chapter 2, any variations in the rate of motion of a biomimetic cilium over its beat cycle will have no effect on transport at low Reynolds number because of the lack of inertia. The fast stroke moves the fluid faster, but it does not move it any farther than the slower recovery stroke moves the fluid in the opposite direction. Thus, even though this beat is an approximation of the airway beat, it will not produce fluid transport, only oscillations of the fluid. However, this may not be true in a viscoelastic fluid. The elasticity of such a complex fluid introduces characteristic time scales to the problem which are not present in a Newtonian fluid. Thus, future work with biomimetic cilia could focus on whether a biphasic beat which is spatially symmetric can produce fluid flow when the elasticity of the fluid plays a role.

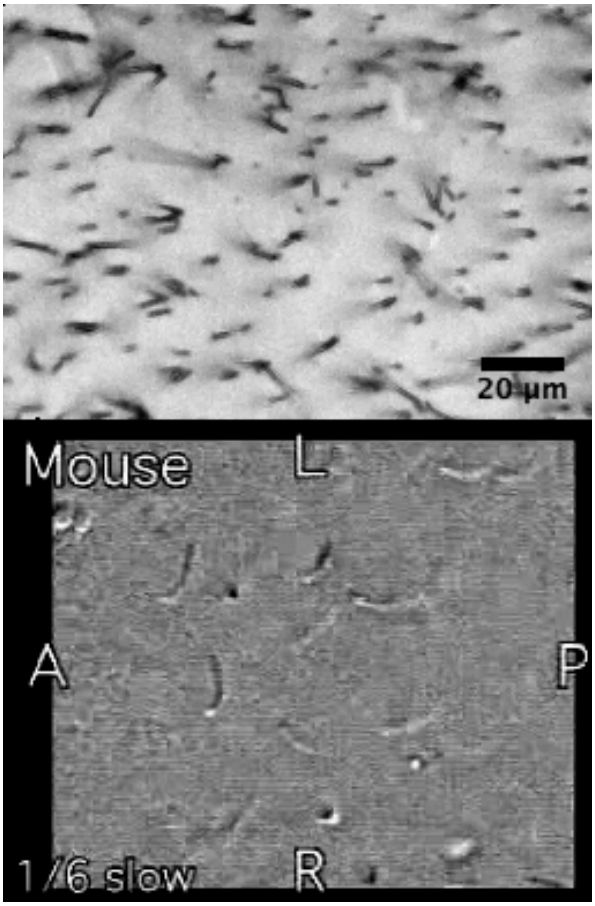

Figure 4.9: Click to Animate. A comparison of the beat of nodal cilia (at bottom, from Okada et al. 2005) with the tilted conical beat of biomimetic cilia (at top). The tilt away from vertical is evidenced by the fact that each cilium's tip moves in an ellipse which is offset from the base of the cilium.

With this in mind, the question becomes: how can I generate fluid transport with a cilium which cannot change its shape over a beat cycle? The answer, of course, is in the beat of embryonic nodal cilia. As I have explained, these cilia are able to generate a net transport of fluid with a rotational motion which does not require shape changes. More specifically, the nodal cilium takes advantage of the presence of the lower boundary in order to generate an asymmetric flow with a spatially symmetric motion. A rotational beat of the biomimetic cilia is relatively easy to generate, as it can be done simply by placing a magnet, in the configuration I have specified (where the dipole is parallel to the surface), directly above the cilia array and rotating the

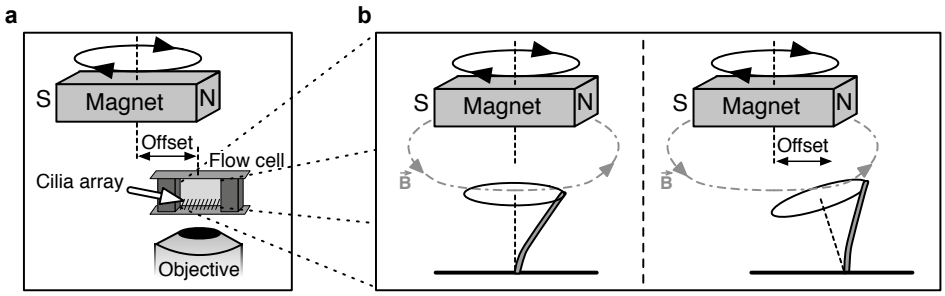

Figure 4.10: In order to mimic the tilted conical beat of nodal cilia I rotate a magnet above the sample. A rotation of the magnet around an axis which is directly above a cilium generates rotational actuation around a vertical axis, while a small offset of the magnet's rotational axis causes the cilium to tilt away from vertical.

magnet. If the rotational axis of the magnet were perfectly aligned with a cilium, all other things being constant the cilium will perform a rotational beat which precesses around a vertical axis. As Cartwright demonstrated, this beat will only produce vortical motion and no transport (Cartwright et al., 2004). However, a tilt of the rotational axis can be generated in my biomimetic samples by a subtle lateral offset of the rotational axis of the motor from the cilium. If the offset is too large the cilia will not execute a clean rotational beat, but if the offset is small enough the beat remains rotational but is tilted away from vertical. In Chapter 5 I will address the effect of this tilt on fluid transport.

4.3.3 Characterizing the tilted conical beat

To conclude this chapter I present some details on the characterization of the tilted conical beat which I will use to compare the fluid transport in my system with the transport driven by nodal cilia in the next chapter. For the parameterization of the tilted conical beat I use the same notation as in the biological system (Okada et al., 2005). As seen in Figure 4.11, the angle between the vertical and the axis of rotation of the cilium is the tilt angle Θ, and the amplitude of the cilium's motion is determined by the half cone angle Ψ. A third parameter is Φ, an azimuthal angle which determines

the direction of tilt, and thus the direction of fluid transport. As the tilt direction in my system is controlled by the direction the magnet is offset from the sample, Φ can be controlled arbitrarily in my system.

In both my system and the embryonic node, the video data obtained by microscopy of a cilium's movement is a two-dimensional projection of its true three-dimensional motion. In the biological system it has been assumed that the nodal cilia tips sweep out a circle, which appears as an ellipse in the projected image, as shown in Figure 4.11a. With this assumption, and measurements of the average nodal cilium length by SEM, the motion is fit to an equation which describes the surface of a cone and the beat parameters are extracted.

In the case of biomimetic cilia, it is highly likely that the cilia tips sweep out an actual ellipse, rather than a circle, and so I have not made this same assumption of circularity. Instead I have calculated the beat parameters based on the method I display in Figure 4.11b-d. I begin by generating a minimum intensity projection of a single beat cycle of the array. From this image I choose a representative selection of cilia performing a recognizable tilted conical beat in order to measure the parameters of each and average the results. Next I select the tip of each cilium in each frame of the projection and fit an ellipse to these points. I trace the length of the cilium from multiple frames and identify the location of the cilium's base, and define the tilt direction as the vector which points from the base through the minor axis of the ellipse. Along this vector, I then measure the projected distance from the base to the nearest and furthest extent of the ellipse. These two distances are labeled d_1 and d_2 in Figure 4.11d.

The measurement of those distances then easily gives the angles Θ_1 and Θ_2 by $\Theta_n = sin^{-1}\left({}^{d_n}/_{L}\right)$ where L is the cilium length. The tilt angle is simply the average of

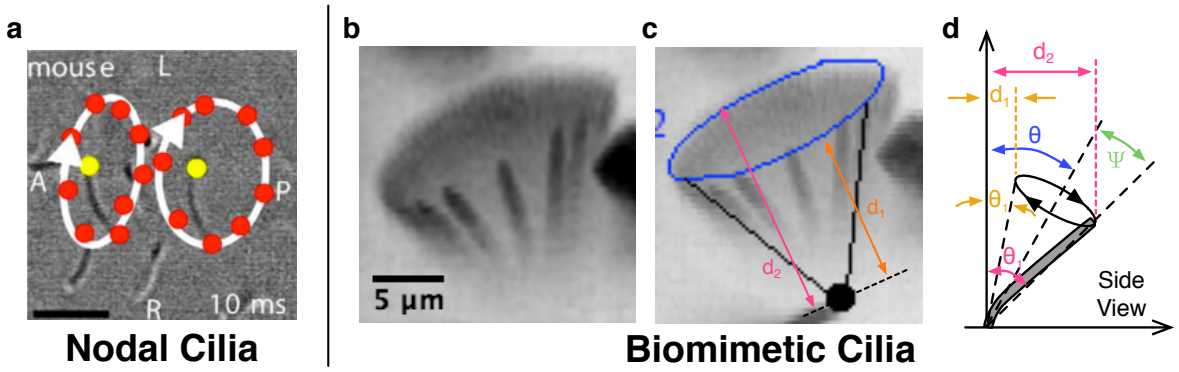

Figure 4.11: At left is an image from Okada et al. (2005) showing their measurement of the tip position of two nodal cilia. The three images at right demonstrate the method I used for finding the tilted conical beat parameters, the tilt angle Θ and half-cone angle Ψ. A minimum intensity projection of a single beat cycle is generated, and the position of the tip at each time point is recorded, along with the inferred position of the cilium's base. Defining the tilt direction as the direction which is parallel to the minor-axis of the ellipse, then d_1 and d_2 are the nearest and farthest distance, respectively, from the base to the ellipse along the tilt direction. From d_1 and d_2 the beat parameters are calculated as shown in equation 4.6.

these two angles, and the half cone angle is half their difference. In other words, I have

$$\begin{aligned}\Theta &= \frac{\Theta_1 + \Theta_2}{2} = \frac{1}{2}\left[sin^{-1}\left(\frac{d_1}{L}\right) + sin^{-1}\left(\frac{d_2}{L}\right)\right], \\ \Psi &= \frac{\Theta_2 - \Theta_1}{2} = \frac{1}{2}\left[sin^{-1}\left(\frac{d_2}{L}\right) - sin^{-1}\left(\frac{d_1}{L}\right)\right].\end{aligned} \tag{4.6}$$

Chapter 5

DIRECTED FLUID TRANSPORT

"One special kind of swimming motion is what I call a reciprocal motion. That is to say, I change my body into a certain shape and then I go back to the original shape by going through the sequence in reverse. At low Reynolds number, everything reverses just fine. Time, in fact, makes no difference – only configuration."

- E.M. Purcell, "Life at Low Reynolds Number"

As Purcell says, to properly imagine yourself as a swimming organism in the microscopic world you must enter a configuration space. At the root of our own world is time, so thoroughly ingrained in ourselves that we do things quickly when they need to be done quickly, and move slowly when we must move slowly. We swim by moving our arms back and forth or kicking our feet, and wave a foul smell away simply by oscillating our hands in front of our faces. For microscopic things, which typically live in fluids and operate at a low Reynolds number, such strange movements are futile. They live in a configuration space, where only the sequence of your motions matters, not their speed. Time makes no difference.

The scallop is in trouble at low Reynolds number, Purcell quips, because to swim he just opens his shell slowly and closes it fast to rapidly expel water, with the extra momentum imparted to the fluid during the fast motion resulting in a thrust on the scallop. But at low Reynolds number there is no momentum, and only the sequence

matters. Because the scallop only has one hinge, one degree of freedom in configuration space, it will forever perform a 'reciprocal motion', never going anywhere. This is the world inhabited by cilia, both biomimetic and biological. To 'swim', or rather, since they are attached to a surface, propel a net transport of fluid, they *must* perform a non-reciprocal motion. As I have discussed, different varieties of biological cilia do this in different ways, and I will mimic the beat of embryonic nodal cilia in order to propel fluid transport with my biomimetic arrays.

I begin this chapter with a brief overview of the fluid flows driven by my biomimetic cilia arrays, the detailed discussion of which forms the bulk of the remaining results presented in this thesis. I have succeeded in demonstrating the first realization of long-range fluid flow with an artificial cilia system by mimicking the beat pattern of embryonic nodal cilia. The form of this long-range transport of tracer particles is what I refer to as 'epicyclic transport', a superposition of a small-scale oscillatory motion, at the frequency of the cilia beat, and a roughly constant velocity, unidirectional motion. In my fluidic cell, this primary transport occurs in a layer extending from the cilia tips to some height, at which point the transport slows and eventually turns in the opposite direction of the main transport. This upper layer of opposing flow extends to the upper boundary of the sample, and is an expected recirculation of fluid due to the main transport layer and the enclosed nature of the flow cell.

Most significantly, I have observed that this transport layer, which is above the cilia tips, exists simultaneously with a layer of fluid flow below the cilia tips whose motion is drastically different. These regimes are depicted schematically in Fig. 5.1 and videos of the particle motion are shown in Fig. 5.2. Below the cilia tips, particle motion is more rapid, on average, but with significantly more heterogeneity. Furthermore, as opposed to the transport layer, below the tips particle motion is essentially non-directional. Thus, the overall flow in the system contains two distinct regimes with a separation

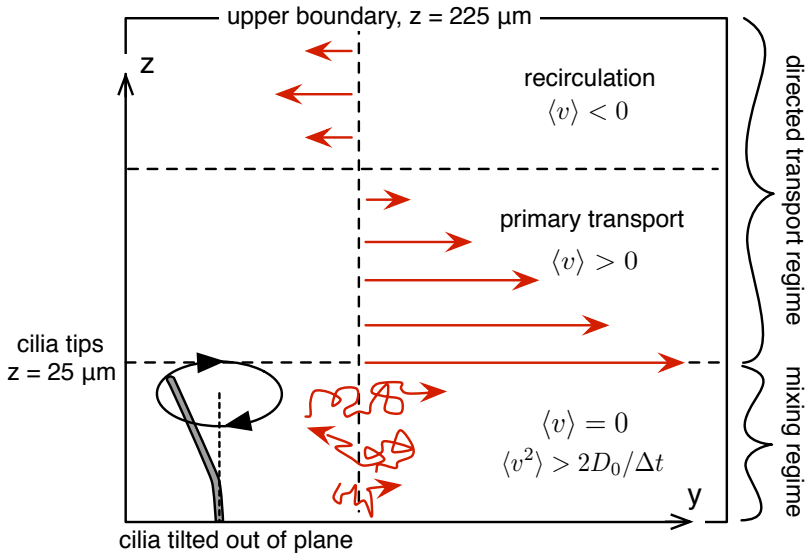

Figure 5.1: Schematic of fluid flow regimes in biomimetic-cilia driven transport. The tilted conical beat of nodal cilia drives simultaneous, spatially segregated flow regimes of unidirectional transport, above the cilia tips, and non-directional, heterogeneous flow below the tips.

at the height of the cilia tips, a unidirectional transport regime and a heterogeneous, non-directional regime.

In the remainder of this chapter I will discuss and analyze the directed transport regime above the cilia tips, including the recirculatory flow. The characterization of the fluid flow regime below the cilia tips is the focus of Chapter 6.

5.1 Transport at Low Reynolds Number

As discussed earlier, the lack of inertial motion in low Reynolds number fluids imposes non-intuitive constraints on the types of motions that will produce a net transport of fluid. Oscillatory motions that are, as Purcell says, purely reciprocal in space, or following the same path forward and backward along the same path in configuration space, will not produce net fluid transport no matter a difference in speed between the forward and backward motion. This notion of a configuration space is a way of

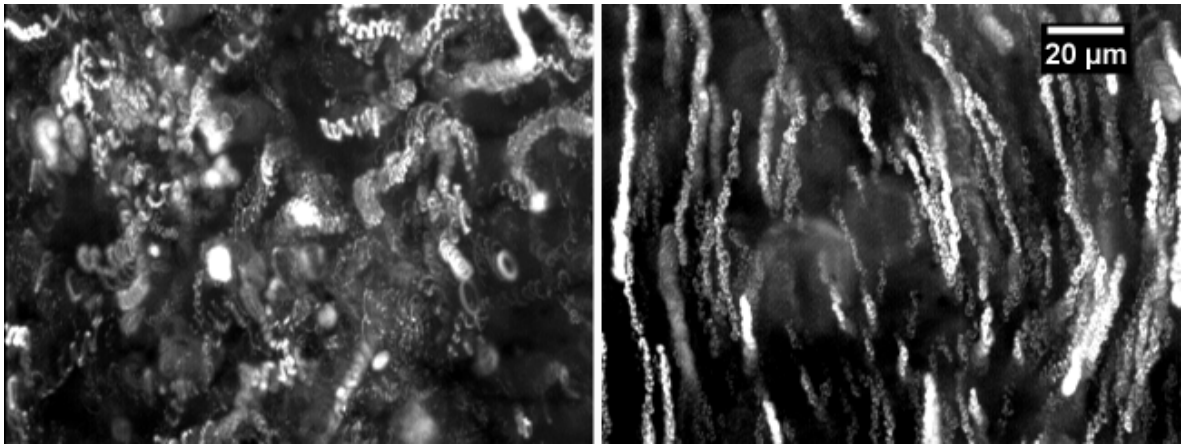

Figure 5.2: Click to Animate. Motion of fluorescent tracers in the fluid flow regimes below the cilia tips (left) and above (right), represented in the poster image by maximum intensity projections of the tracer motion.

thinking about the sequence of motions rather than the speed at which they happen, which is more intuitive for us. A reciprocal motion is one in which the sequence of motions is the same forward and backward. Note the difference between this and time reversibility. For a process reversible in time, a movie played of the process looks the same whether the movie is run in forward or reverse. If the speed of the object changes in time, then the movie does not look the same run backwards. However, the *sequence* of the motions is the same forward and backward, and just a change in speed is not enough to make for a non-reciprocal motion.

As an example, Purcell points out with his 'Scallop Theorem' that at low Reynolds number the scallop is in big trouble. It normally swims by opening its shell slowly and closing it fast. In normal fluids this change in speed means that the scallop gains more thrust, or imparts more momentum to the fluid, in one direction (from closing his shell quickly), than the thrust generated in the opposing direction by opening his shell slowly. The scallop's problem is that it only has one hinge, or one degree of freedom in configuration space. So the scallop can never produce a non-reciprocal motion.

Flagella overcome this problem by simply turning in a single direction like a corkscrew,

so that they never have to go backward in configuration space. Their configuration space is one-dimensional (the angle the flagellum has swept through) but because it never goes backwards it does not perform a reciprocal motion. Motile, 9+2 cilia perform an oscillatory beat pattern with motion that is essentially confined to a single plane. As I have mentioned, this planar beat pattern will only produce low Reynolds number transport if the shape or contour of the cilium changes over the beat, as otherwise it is a reciprocal motion and will only result in oscillatory motion of the fluid. Biological cilia produce the necessary deformation in the axoneme with internal machinery in the form of axonemal dynein, the approximately 3,000 molecular motors per cilium which somehow coordinate their motion to produce drastic shape changes between the power and recovery strokes of a cilium.

It is clear that with my biomimetic cilia, which of course lack this internal machinery, that I will be unable to generate a complex shape change. I demonstrated a planar beat in the previous chapter, but without the ability to change shape this motion does not produce transport, only an oscillation of the fluid. I note that, even if the planar beat is adjusted so that the oscillation is about an axis away from vertical (as with nodal cilia, but still in a plane), the sequence of motions is the same in forward or reverse, and in this case the plane does not break any symmetry which would allow the motion to produce transport.

However, it is possible that such a motion can induce flow by taking into account drag on the cilium, as differential drag forces due to a change in speed can cause differences in shape which could result in flow. This is based on another dimensionless ratio known as the sperm number, a ratio of the stiffness of a body to the drag it experiences. Interestingly, recent work suggests that over a specific range of sperm numbers, a tilted planar beat should be able to generate directional transport at one end of this range, while at the other end of the range the same motion will produce

transport in the opposing direction (Alexeev et al., 2008). One way to change the sperm number is simply by adjusting the beat frequency of a cilium. Thus, the tilted planar beat would be an interesting avenue for further pursuit, as it might be a means of controlling the flow direction simply by adjusting the beat frequency of the biomimetic cilia.

The discovery twelve years ago of a new class of primary, 9+0 cilia, which were the first discovery of motile primary cilia, has served as an inspiration for producing fluid transport with my artificial system with a beat that can be easily generated. As discussed in Chapter 3, these 9+0, nodal cilia were discovered on the ventral surface of a mouse embry within a fluid-filled cavity known as the embryonic node (Sulik et al., 1994). In free space, a rotational beat will not produce low Reynolds number transport as it is, like the planar beat, a reciprocal motion. However, in 2004 Cartwright et al. predicted that the nodal cilia were beating such that the cone swept out during a rotation is tilted away from vertical, with respect to the cell floor. The interaction of the fluid with the floor allows this 'tilted conical beat', depicted in Figure 5.3, to produce net fluid transport. Most importantly for my system, this directed transport does not depend on any type of structural deformation of the cilium.

5.2 Directed Transport with the Tilted Conical Beat

In order to obtain cilia-driven fluid flow data, the cilia array was integrated into a fluid cell with known boundary conditions as I described in the last chapter. Before sealing the fluidic cell a solution of fluorescent tracer particles was introduced in order to serve as passive tracers of the fluid motion. These tracers were typically 500 nm or 1 μm in diameter, and were diluted into a solution of buffer at concentrations of approximately 1:500 of the stock solution.

After sealing the fluidic cell, the sample was placed onto the microscope stage and

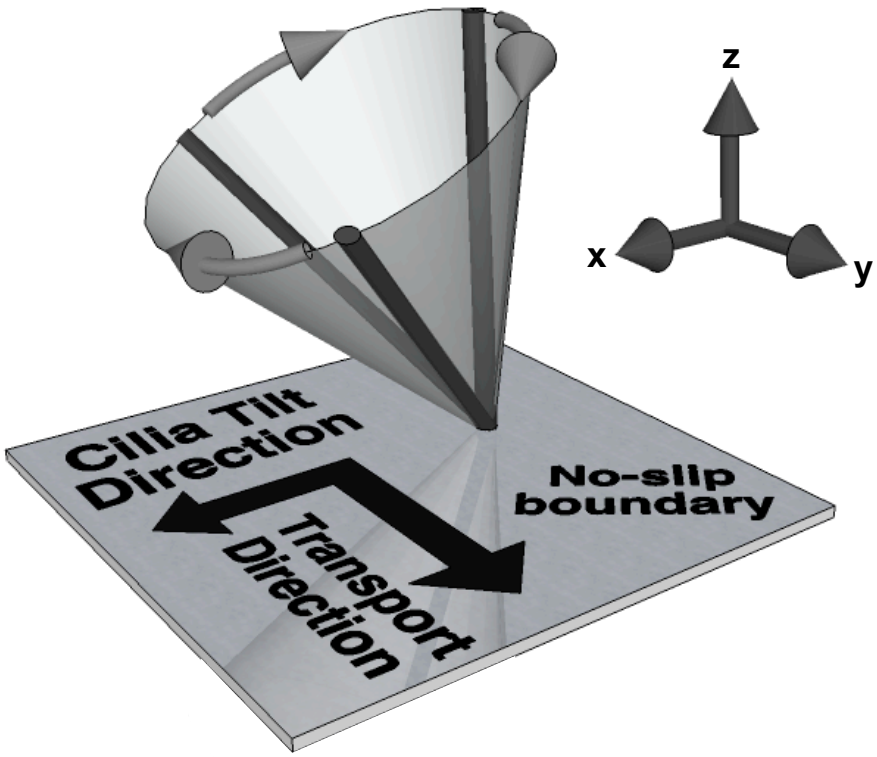

Figure 5.3: The tilted conical beat and corresponding direction of fluid transport due to the fluid's interaction with the floor. The cilium is tilted along the x-axis. When the cilium is nearer the boundary, the volume of fluid entrained by the cilium is decreased relative to the 'power stroke', when the cilium tip is farthest from the floor. Thus, the net effect on the fluid is a unidirectional transport at an angle 90° from the tilt direction.

subjected to magnetic fields rotating at frequencies of $1 - 30\ Hz$. Video data was obtained using a Pulnix TM6710 camera operated at 30 or 120 frames per second. The particle trajectories were then tracked with either Video Spot Tracker, freely available software developed by computer science colleagues in our lab, or with ImageJ's Manual Tracking plugin.

5.2.1 Generating a tilted conical beat

In Chapter 4 I described the production of a conical beat with a simple actuating magnet geometry, consisting of a single bar magnet positioned above the cilia sample with the magnet's dipole oriented perpendicular to the upright cilia. Rotating the magnet such that its rotation axis is directly above the cilia sample produces a conical cilia beat. In order to tilt this conical beat away from vertical the actuating magnet is adjusted such that the rotational axis of the magnet is offset from the cilia sample by a few millimeters (Figure 5.4). The magnitude of the beat, parameterized by the half-cone angle Ψ, is controlled by the strength of the magnetic force, which in my system is equivalent to the separation distance between the sample and the magnet.

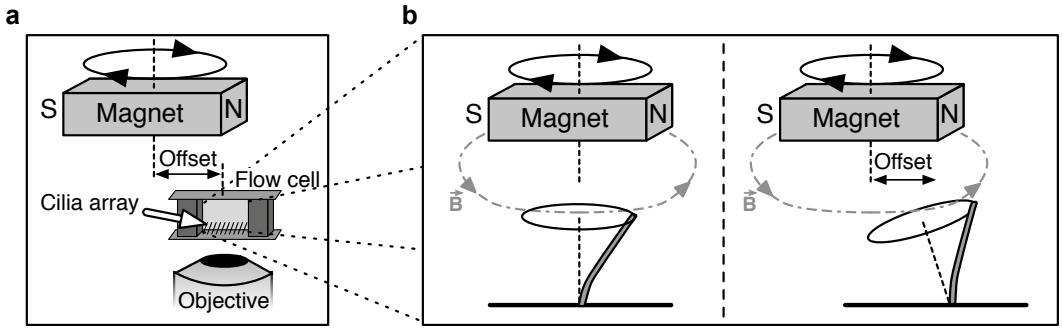

Figure 5.4: An offset of the magnet's rotational axis from the cilia array produces a tilted conical beat, as I also described in Chapter 4.

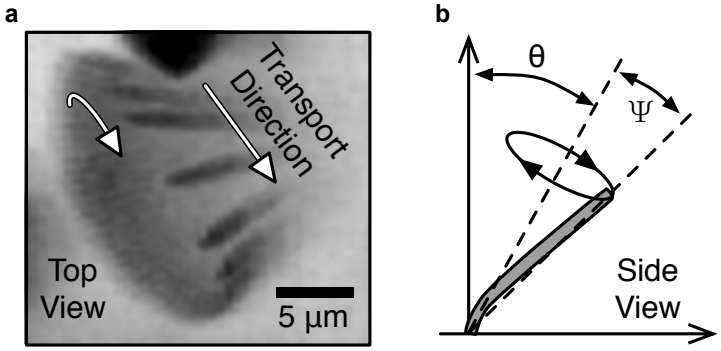

Figure 5.5: (a) A minimum intensity time lapse projection of one beat of a single cilium executing the tilted conical beat. The direction of the magnet's offset controls the tilt direction, and thus the fluid transport direction. (b) The tilted conical beat is parameterized by a tilt angle Θ and half-cone angle Ψ. The magnitude of the magnet's offset controls Θ and the applied magnetic force determines Ψ.

5.2.2 Mimicking the nodal beat produces epicyclic transport

By mimicking this nodal cilia beat pattern, my system has achieved the first demonstration of long-range fluid transport with an artificial cilia system. The tracer motion due to the tilted conical beat has two characteristic time scales. At the frequency of the cilia beat, each tracer performs an epicycle due to the coupling between the fluid and the cilia surfaces, as I discussed for the work of Bouzarth et al. in Chapter 3 (Bouzarth et al., 2007). As the cilia beat patterns are forced into synchrony by the magnetic field lines (as opposed to airway cilia, which exhibit coordinated, but not synchronous, beats), the tracers consistently exhibit these epicycles even at heights many multiples of the cilia length. Some form of these epicycles exist for any beat, planar or rotational, regardless of tilt. However, due to the tilted conical beat the epicycles are superimposed on a longer time scale motion, which is unidirectional transport. Figure 5.6(a-b) displays the pathline and radial displacement of a single tracer particle exhibiting epicyclic transport. In (a), each epicycle is differently colored to make them clearly distinguishable, while the net displacement of approximately 5 μm in (a) and (b) reflects the directed transport due to the tilted conical beat. In 5.6(c), two pathlines display a

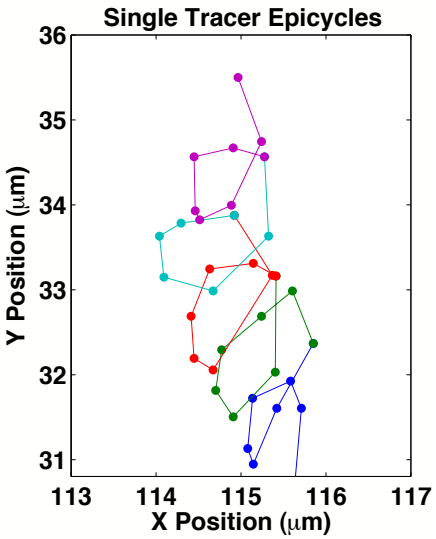

(a) Tracer motion is epicyclic transport. Each epicycle of the tracer is represented by a different color. Every epicycle reflects a single beat of the cilia array, and the overall transport (in the vertical direction) is due to the tilted conical beat.

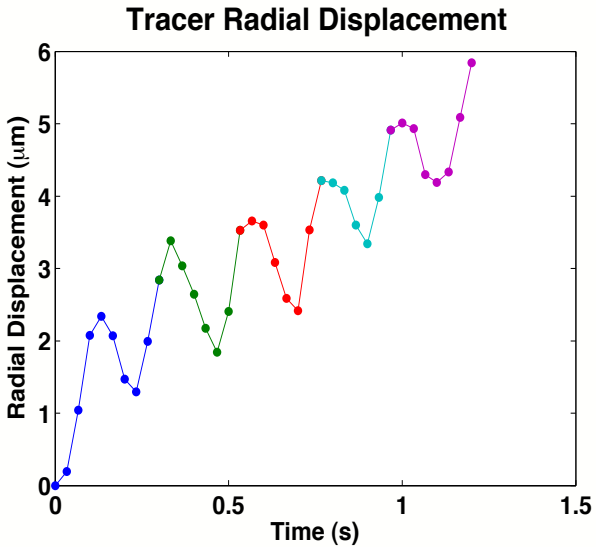

(b) Radial displacement of the tracer in (a) vs. time, demonstrating that the oscillatory, epicyclic tracer motion is superimposed on directional transport at roughly constant velocity. The colors correspond to each epicycle in (a).

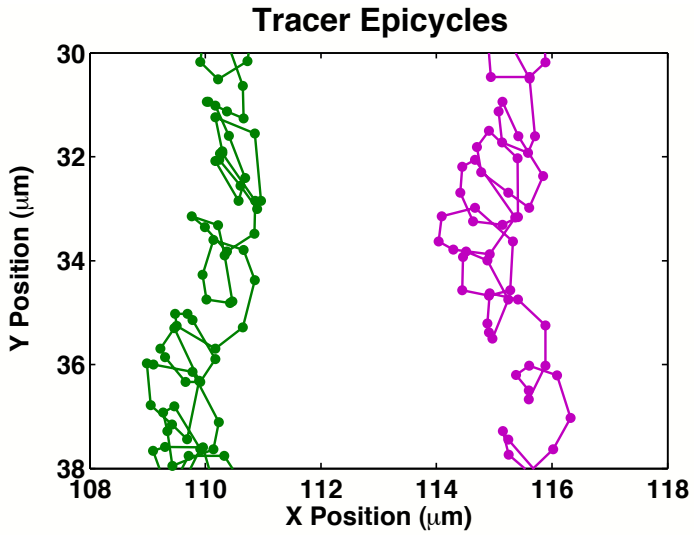

(c) Pathlines over 2 seconds of two nearby tracers exhibiting epicyclic transport. The tracer path pictured in (a) is a portion of the trajectory on the right.

Figure 5.6: Displays of the biomimetic cilia-driven epicyclic transport of a single tracer (a-b), and a broader view of the transport of two nearby tracers (c).

wider view of the epicyclic transport.

Epicycle amplitudes and velocities vs. height

Based upon my description of Stokes 2nd problem in Chapter 2, it would be interesting to inquire as to whether the oscillatory nature of these epicycles can be understood within the context of the oscillatory motion of a continuous boundary. A group of researchers within the Virtual Lung Project have constructed a device for measuring the rheological properties of a viscoelastic material which is based upon the idea of Stokes 2nd problem, and the authors appreciated that the oscillatory nature of cilia might have a similar type of effect on mucus (Mitran et al., 2008). However, to my knowledge no theoretical or experimental work has shown that cilia actually generate fluid motion which can be explained within Stokes 2nd problem.

In the case of my data, the oscillatory motion of a tracer is superposed onto the directional transport. It is for this reason that I gave the solution for the superposition of the modified form of Stokes 2nd problem with Couette flow in Chapter 2. To repeat, the velocity profile of such a flow, when the boundary oscillates as $u(t) = U\ cos\ \omega t$ and simultaneously translates at speed u_0, would be given by

$$u(y,t) = \mathrm{Re}\left[Ue^{i\omega t}\frac{sinh\left[\frac{\delta_0}{A}(h-y)\right]}{sinh\left[\frac{\delta_0 h}{A}\right]}\right] + \frac{u_0}{h}(h-y) \tag{5.1}$$

where $A = {}^{U}\!/_{\omega}$, $\delta_0 = (1+i)\sqrt{{}^{\omega}\!/_{2\nu}}$, h is the distance between boundaries, and u_0 is the velocity of the translating plane which drives Couette flow.

There are two behaviors I would like to match with the Stokes 2nd problem model. The first is the radial displacement of a tracer, which in the model is a combination of the effects from the boundaries oscillatory and translational motion. To compare the model with an experimental tracer's motion, I first measured the velocity of a tracer at the height of the cilia tips and defined this velocity as the Couette flow velocity u_0.

I must also obtain the cilia beat frequency. This can done, among other ways, by measuring the average epicycle amplitude of an ensemble of tracers, and calculating the frequency of the cilia beat/tracer oscillation based on the frame rate and epicycle amplitude. I momentarily digress to describe the method I use to measure epicycle amplitudes, which is shown in Figure 5.7. I define the epicycle amplitude as the distance between adjacent extrema in the radial displacement. Due to the net transport, the displacement from minima to maxima is, on average, slightly larger than vice versa. The mean epicycle amplitude is then the average of the amplitudes of each tracer at a given height.

Finally, I must measure the height of the experimental fluidic cell, which is straightforward using a micrometer on the focus knob of the microscope, and I must have a measure of the maximum oscillatory velocity of the plane U. As a first estimate, I might assume that this is the same as the tip speed of the cilium, which is easily obtained from the beat parameter measurements I described in Chapter 4. In this case, I do assume the tip beats out a circular path, and so the tip speed is only a function of the half-cone angle Ψ and is $u_{tip} = Lsin\Psi$ where L is the cilium length.

This provides all the information necessary to compare the model with an experimental track. However, in order to get a good match between the epicycle amplitude at the height of the cilia tips and the epicycle amplitude in Stokes 2nd problem, I must make one assumption. I must assume that the interaction of the cilia with the fluid at the height of their tips is, on average, reduced by about a factor of 2 with what would be expected at the no-slip surface of the cilium. This assumption is supported by evidence from cilia on the surface of protozoans, where it has been observed that particle velocities near to cilia are about 2-3 times decreased from the velocity of the cilium (Sleigh and Aiello, 1972).

I have assumed that U, the maximum oscillatory velocity, is equal to $u_{tip}/1.5$, where

the factor of 1.5 is chosen to give an approximate match with the experimental tracer epicycle. The particle path which is described by the velocity time course of equation 5.1 can then be calculated. In Figure 5.7b I compare the radial displacement from the model with that of a single experimental tracer. It is clear that the frequencies are slightly mismatched, but the basic motion is well-described. Of course, I have somewhat arbitrarily reduced U to match the epicycle amplitude, but this factor is close to that reported in the literature, and even without it the predicted epicycle amplitude is just 50% larger than measured in the experiment. This suggests that a version of modified Stokes 2nd problem in which the oscillatory velocity of the plane is reduced by an *ad hoc* factor is a good model for tracer motion above a field of cilia executing the tilted conical beat.

The second behavior which should be considered within modified Stokes 2nd problem is the decay of the epicycle amplitude with height. By integrating the velocity profile in equation 5.1 with respect to time the displacement is easily obtained The epicycle amplitude itself is not a function of time, and so the amplitude of the oscillatory motion which Stokes 2nd problem predicts is

$$|x(y)| = \mathrm{Re}\left[\frac{U}{\omega}\frac{sinh\left[\frac{\delta_0}{A}(h-y)\right]}{sinh\left[\frac{\delta_0 h}{A}\right]}\right]. \tag{5.2}$$

Again, however, a quick comparison with the experimental data make it clear that this prediction does not decay fast enough to match. I must introduce another *ad hoc* factor which somehow conveys the fact that the 'plane' is not as well coupled to the fluid as would be expected in Stokes 2nd problem. Of course, in my experiment there is no plane at all. At the height of the cilia tips, each cilium rotates and sweeps out some area, but the sum of all of these areas still does not equal the area of the entire plane. Thus, I argue that, conceptually, the fluid can be thought of as having been decoupled from the plane by a factor approximately equal to the fraction of the plane which the

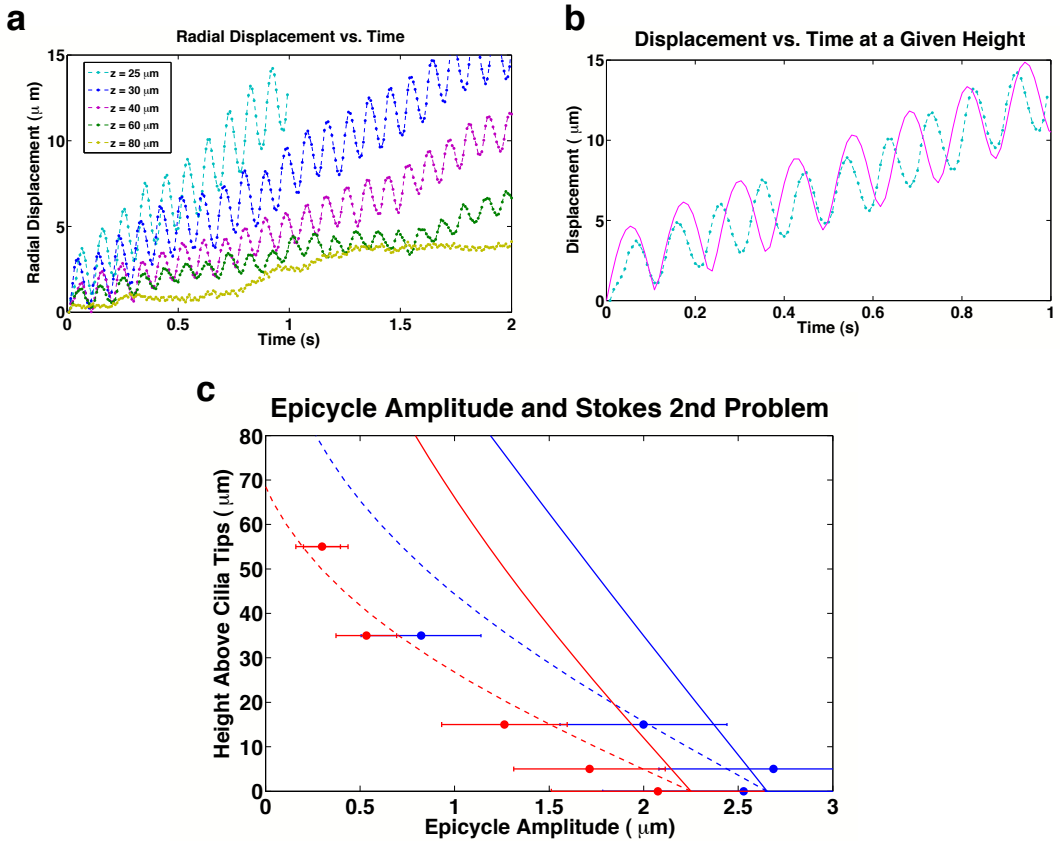

Figure 5.7: (a) To measure the amplitude of cilia-driven epicycles I plot the radial displacements over time, identify the local maxima and minima, and define the epicycle amplitude as the average displacement between adjacent extrema. In (b) I have taken the radial displacement of a tracer at $z = 25\ \mu m$ and plotted the radial displacement of a simulated track from the Stokes 2nd problem velocity profile. As described in the text, to achieve a decent match with the epicycle amplitude required me to assume that the interaction with the cilia has dropped off by a factor of 1.5 even at the same height as the cilia tips. (c) Finally, by assuming that a similar decrease in effective viscosity can account for the fact that the cilia do not form a continuous plane, I plot the amplitude epicycle vs. height and compare it to the amplitude from Stokes 2nd problem for two different cilia beat frequencies (red, 12 Hz and blue, 33 Hz). The solid curves are the predictions from equation 5.2 with the actual viscosity, and the dotted lines are from assuming a decreased effective viscosity. This behavior suggests that the cilia-driven motion can be thought of as Stokes 2nd problem in which the interaction strength is reduced by roughly the area fraction described in Figure 5.8.

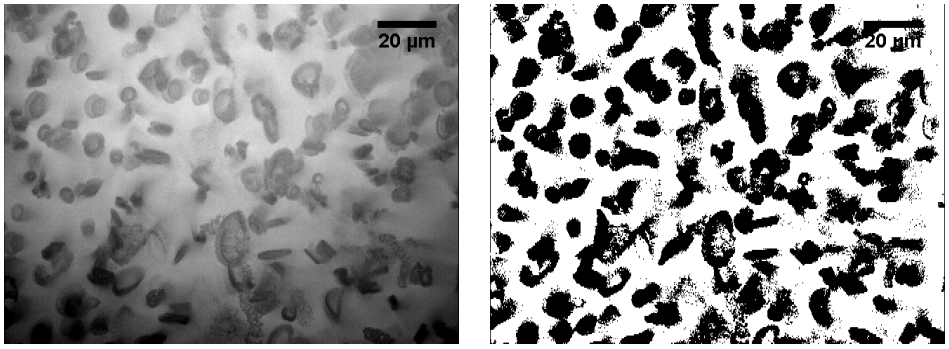

Figure 5.8: To measure what area of the plane at the height of cilia tips is encompassed by the motion of the cilia tips over a beat cycle, I first obtained the minimum intensity projection over many beat cycles, so that the area the cilia cover is much darker than the background. However, the illumination is not flat (uniform across the field-of-view), and so I convolve the MIP and divide the original by the convolved image to flatten the illumination. Finally, the image is thresholded, which is displayed at right, and the area which is black is calculated as a fraction of the total.

cilia tips encompass over their beat cycle. I display in Figure 5.8 the method I use to measure this area fraction, and for this experiment it is very close to 50% of the total area of the video frame.

Thus, I make the additional *ad hoc* assumption that the decoupling of the 'plane' at the height of the cilia tips from the fluid can be accomplished by an effective viscosity which is reduced by the area fraction. In Figure 5.7c I also display the experimental epicycle amplitudes as a function of height, comparing the predicted amplitude from Stokes 2nd problem with and without this decoupling factor. Using the area fraction as a measure of the reduction in the effective viscosity of the fluid clearly gives a much better estimate of the rate of decay of the epicycle amplitude with height.

To conclude this section, I have shown for the first time that Stokes 2nd problem can be applied as a model for understanding particle transport above an array of oscillating cilia. I have been forced to make two *ad hoc* assumptions, but I now note that in reality these two assumptions are the same conceptually, but applied to two separate phenomenon in the model. Both assumptions are that the cilia interaction with the fluid is reduced by about a factor of 2 from what one would expect for a flat plane.

This assumption must be applied to the cilia tip velocity in order to achieve the correct amplitude at the height of the cilia tips, and then it must be applied again as an effective viscosity in order to describe the fact that the modeled plane only interacts with the fluid over a fraction of its total area.

5.2.3 Cilia-driven, long-range, directed fluid transport

Over longer time scales than the epicycle period, the tilted conical beat drives long-range, directed fluid transport. In this section I will describe this directed transport at the height of the cilia tips, before turning to a description of the flow over the entire height of the flow cell. At the cilia tips I define the average fluid velocity as u_0. This average velocity is relatively constant over the entire cilia array and is typically on the order of $5 - 10$ $\mu m/s$, much slower than the short time scale speeds around an epicycle of about 150 $\mu m/s$ (as in Figure 5.7).

Figure 5.9 shows a sequence of maximum intensity projections of fluorescent tracer motion at the height of the cilia tips, up to a duration of about 20 seconds. The directional transport is clear, and the epicycles are also visible. This tracer motion is the raw video data which I tracked to produce the results in Figure 5.10. The first two panels (a-b) are the average tracer velocities along each component of the video frame, demonstrating that the mean transport is entirely along the y-direction. In panel (c), I plot the pathlines of those tracers which were tracked from this data set, with the local color of the pathline mapped to the tracer velocity averaged over a 0.25 s window. Panel (d) shows the distribution of velocities, in the transport direction, for the tracers in (c), as well as for diffusive tracers tracked while the cilia were motionless.

I will discuss the process of diffusion in more depth in Chapter 6, but I briefly note that the probability distribution of tracer velocities for diffusive motion should be zero mean and Gaussian, as it appears to be, with a standard deviation which

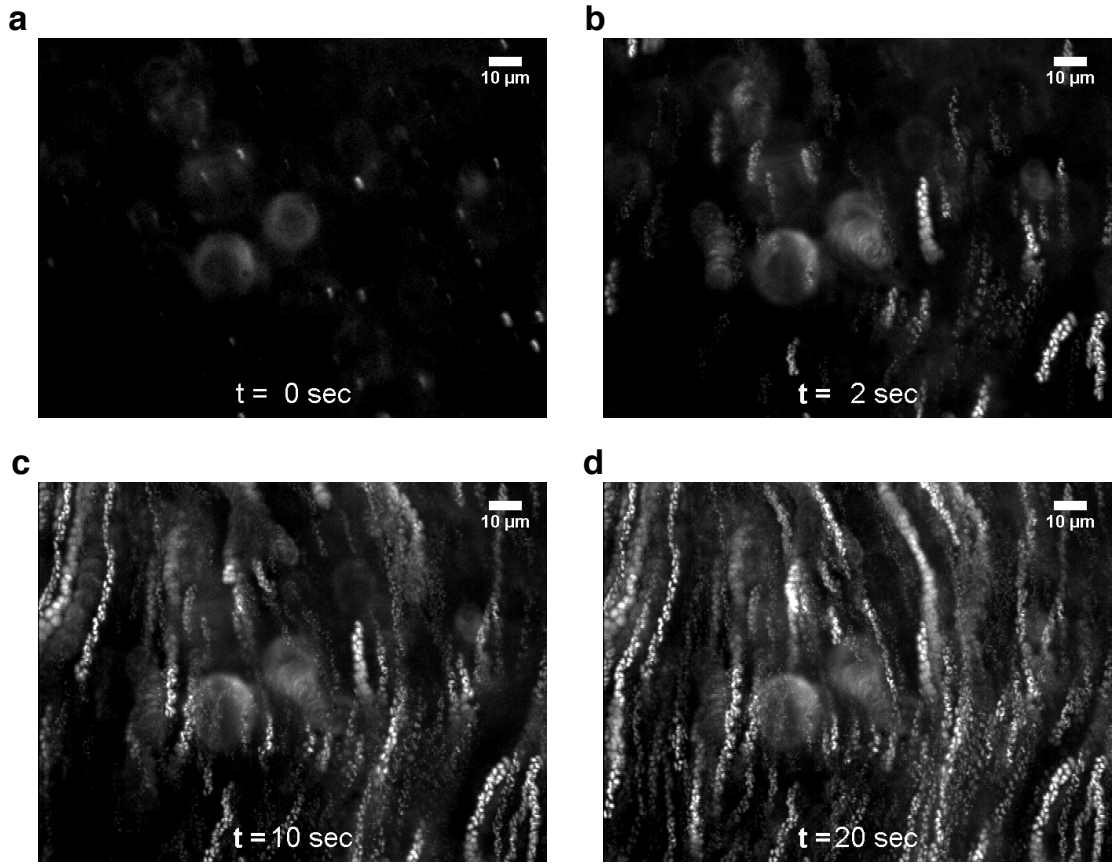

Figure 5.9: Montage of maximum intensity projections, of increasing durations in time, of the directed transport of fluorescent tracers at the height of the cilia tips. The overall directionality, towards the bottom of the video frame, is clearly evident. The larger, blurry circles are slightly out-of-focus light from beads which are stuck to individual cilia.

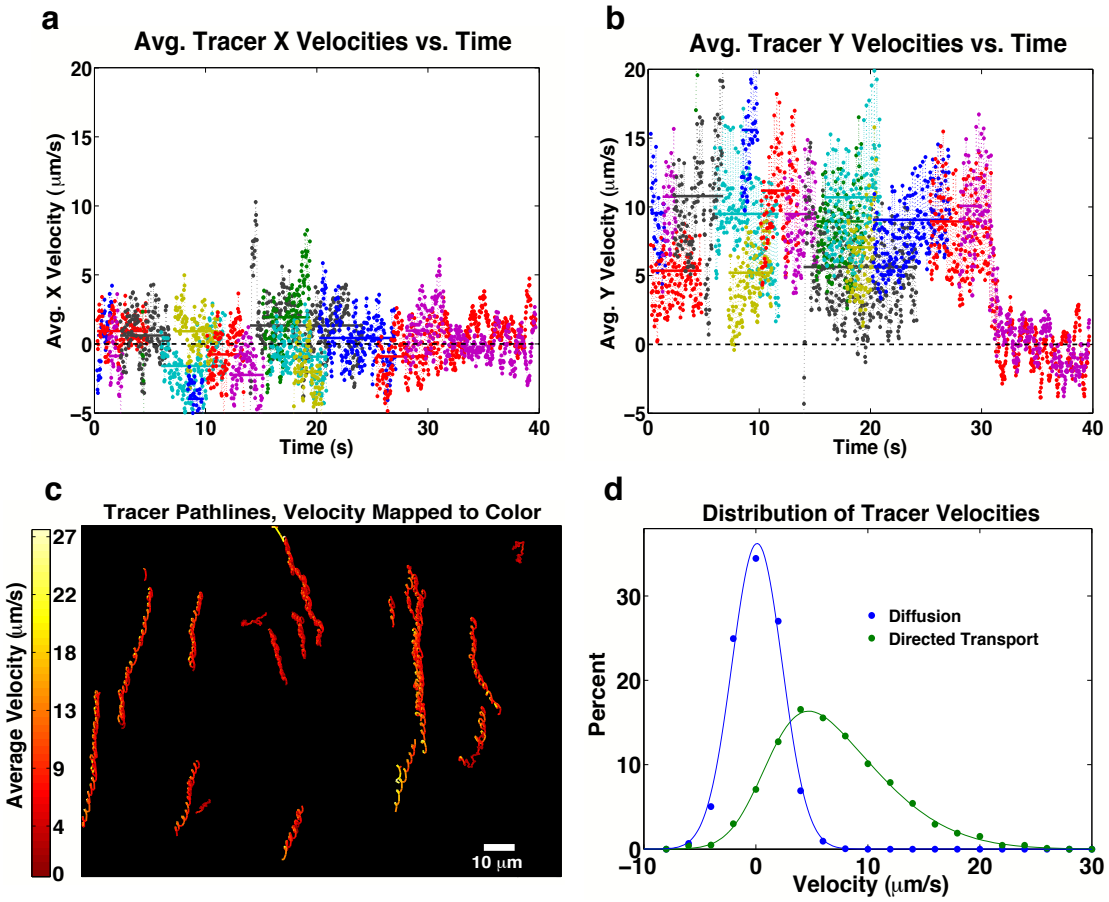

Figure 5.10: Analysis of tracer velocities for those tracers shown in Fig. 5.9. (a) Tracer x velocities vs time, showing the lack of any significant motion in the x direction. (b) Tracer y velocities vs. time, demonstrating the directionality and variation of the tracer motion. In (a-b), each colored line is a single tracer, and the solid bar of the same color is that tracer's average velocity over the time it was tracked. (c) Pathlines of video-tracked tracer particles with the local average velocity, over a 0.25 s window, mapped to color. (d) Probability distributions of the component of the tracer velocities in the transport direction as a percentage of the total counts in (b). The green dots show the distribution of the cilia-driven tracer velocities shown in (b). In comparison, the blue points are for diffusing particles, tracked while the cilia were turned off. The solid curves are fits to a skew normal distribution, as described in the text. From the fit, the mean of the transport velocity is 7 ± 5 $\mu m/s$ (s.d.) and the skewness is 0.4. As expected, the distribution for the diffusive tracers is mean zero and has no skew.

reflects the diffusivity of the particles. In contrast, the distribution of the cilia-driven tracers in the directional transport is clearly non-Gaussian. At first glance, there is no obvious reason why the velocity distribution above the tips should not be Gaussian, but it is clearly skewed to the right. I attribute this skew to the manner with which I generate the tilted conical beat (by offsetting the magnet's rotational axis). This setup leads to a non-constant angular velocity of the cilium over a single beat cycle, and this non-constant velocity produces probability distributions which are skewed in the direction of fluid transport. Although the magnet's rotation itself is at a constant angular velocity, the offset means that when the magnet passes directly over the cilia sample, the cilium's deflection changes more rapidly than when the magnet is further from the sample. This change in angular velocity can be seen in the minimum intensity projection in Figure 5.5 as a difference in the spacing of the cilium's position between frames, as well as in the animation in Figure 5.12. However, I emphasize that, as the reader learned in Chapter 2, the low Reynolds number of the system means that this change in angular velocity is not the reason for the directed transport.

This non-constant angular velocity also leads to velocity distributions whose characteristics change based on the duration of the averaging window used to calculate the tracer velocities. This behavior is displayed in Figure 5.11 for multiple distributions from the same dataset, but with differing averaging times. Over a small averaging time window, the rapidity of the cilia beat during its effective stroke means that a majority of the data points of a tracer's velocity time course correspond to the recovery stroke, when the cilium moves more slowly. Thus, the velocity distribution over short time scales has a negative mean, even though the tracer's long-time average velocity is in the positive direction. Increasing the duration of the averaging window adjusts the mean of the distribution until, above about 0.25 seconds, it reflects the properties of the bulk flow rather than the properties of the tracer oscillation.

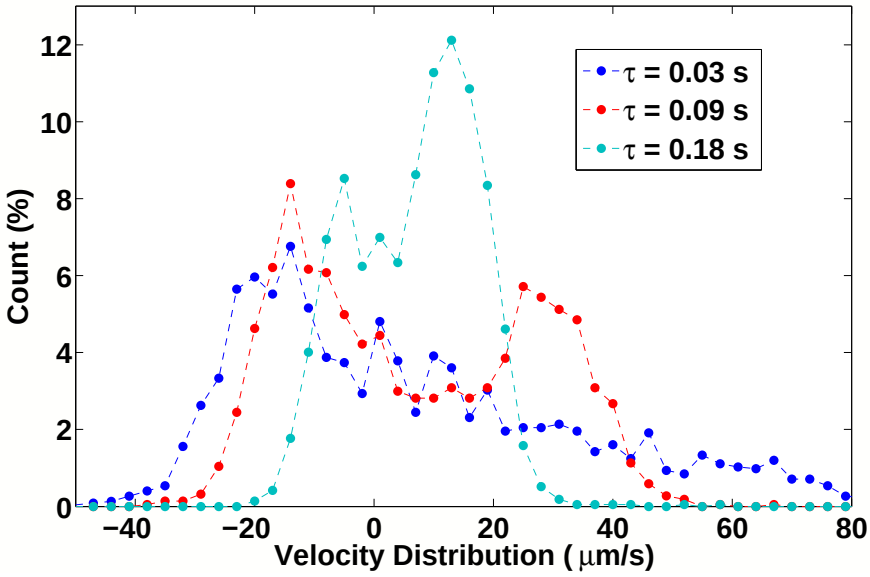

Figure 5.11: The velocity distributions above the cilia tips have a mean which depends on the averaging time used to calculate the tracer velocities. This is due to the non-constant angular velocity of the cilia beat, which means that at short time scales the majority of the counts correspond to the parts of the tracer oscillation in which it is moving in the negative direction. At longer time scales the average motion becomes that of the directed transport, in the positive direction.

Because the non-constant angular velocity of the cilia tips produces tracer velocity distributions above the tips which are not symmetric about the mean I have fit this distribution to a more general form of a Gaussian which incorporates skew, the so-called skew normal distribution. From the fit I compute that the mean of the fitted distribution is 7 $^{\mu m}/_{s}$ and it's skewness is 0.4.

The Skew Normal Distribution. The probability density function (PDF) for a normally distributed variable x is a Gaussian given by

$$\phi(x) = \frac{1}{\sqrt{2\pi\sigma^2}} e^{\frac{-(x-\mu)^2}{2\sigma^2}}, \tag{5.3}$$

with mean μ and standard deviation σ. The cumulative distribution function (CDF), which represents the probability of a value being less than some value x, is given for the normal distribution by

$$\Phi(x) = \int_{-\infty}^{x} \phi(t)dt = \frac{1}{2}\left[1 + \text{erf}\left(\frac{x}{\sqrt{2}}\right)\right] \tag{5.4}$$

where erf is the error function.

A Gaussian distribution is symmetric about the mean, or equivalently does not have any skew. A skew normal PDF with parameter α can be constructed from the normal PDF and CDF and is given by

$$f(x) = 2\phi(x)\Phi(\alpha x). \tag{5.5}$$

where we take $x \rightarrow {(x-\delta)}/{\gamma}$. This substitution provides the location and width parameters δ and γ, respectively. The statistics of the skew normal distribution are then given by the following, using the parameter $\xi = {\alpha}/{\sqrt{1+\alpha^2}}$:

$$\begin{aligned} \text{mean} &= \delta + \gamma\xi\sqrt{\frac{2}{\pi}}, \\ \text{variance} &= \gamma^2\left(1 - \frac{2\xi^2}{\pi}\right), \\ \text{skew} &= 2(\pi-3)\frac{({\xi^2}/{\pi})^3}{(1-{2\xi^2}/{\pi})^{3/2}}. \end{aligned} \tag{5.6}$$

For a skewless distribution $\alpha = \xi = 0$, and the distribution is equivalent to a Gaussian with mean $\delta = \mu$ and $\gamma = \sigma$ (Azzalini, 1985).

5.2.4 Directionality of epicyclic transport

The direction the cilia are tilted, and thus the direction of fluid transport, is determined by the relative positioning of the magnet and the cilia sample, as described in

the caption to Figure 5.5. This correspondence is also demonstrated in Figures 5.12 and 5.13. Figure 5.12(a) displays a minimum intensity projection of cilia in a 50x field-of-view. Despite the random nature of the array, and the differences in the beat of individual cilia, a number of cilia can easily be identified as being tilted towards the top of the image. As these cilia are actuated with a counter-clockwise rotation, the fluid flow due to the tilted conical beat should be approximately rightward. The maximum intensity projection of fluorescent tracer motion in (b) shows that this indeed is the case.

Thus, by repositioning the actuating magnet I can generate fluid transport in any in-plane direction. This control over directionality is a novel ability of cilia as a micropump, as with any traditional pump which operates externally to the fluidic system the flow direction is essentially fixed. In addition, the direction of transport can rapidly be switched 180° simply by reversing the rotation of the actuating magnet, as demonstrated in Figure 5.13. These results highlight the unique ability of biomimetic cilia to function as a novel device for micropumping, as well as other applications such as the precise micropositioning of objects (Suh et al., 1997).

5.2.5 Transport velocity vs. cilia beat frequency

I can also easily control the velocity of the transport by adjusting the frequency of the cilia beat. Figure 5.14 displays the cilia-driven fluid velocity u_0, at the height of the cilia tips, as a function of beat frequency for three combinations of tilt angle Θ and half-cone angle Ψ, clearly exhibiting a linear relationship. This control over the velocity would, in an open-ended channel, provide an easy means for adjusting flow rates in a microfluidic pumping context. This linear relationship with beat frequency will also be of interest below.

In addition, Figure 5.14 displays a comparison of biological measurements of the

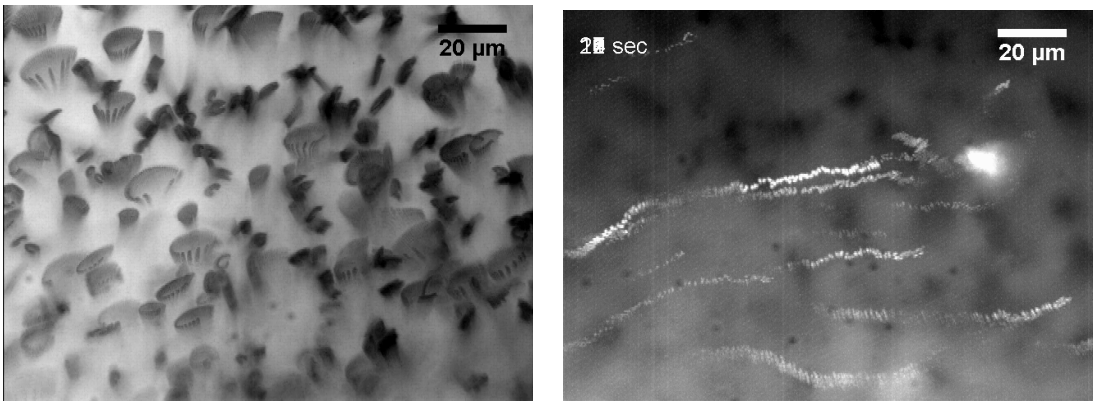

(a) **Click to Animate** (b)

Figure 5.12: Fluid flow directionality is controlled by cilia tilt direction. (a) A minimum intensity time lapse projection of a single rotation of a cilia array. Heterogeneity in the cilia beat patterns is evident, but many cilia have an obvious tilt towards the top of the image. (b) A maximum intensity projection of fluorescent bead motion over the array in (a). The cilia in (a) are rotating in the counter-clockwise direction as viewed from above, producing a net motion of fluid towards the right.

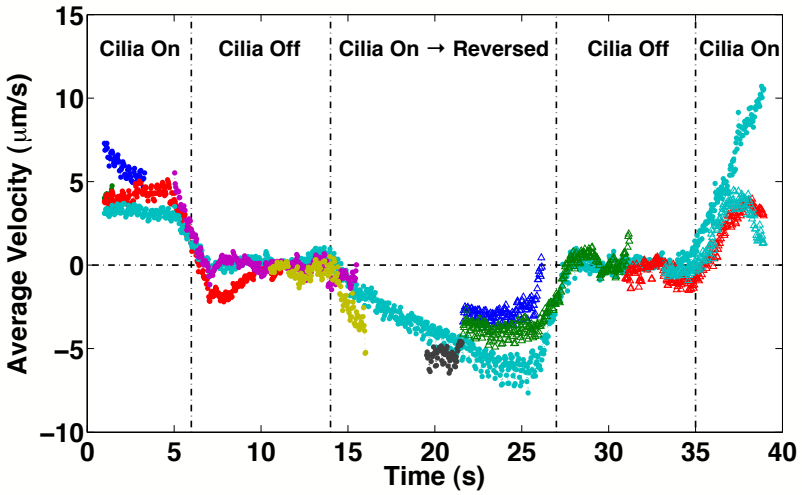

Figure 5.13: Switching fluid transport direction by reversing the cilia beat. Initially the biomimetic cilia are driving fluid transport in a given direction. At $t = 6$ s the cilia are turned off and the transport ceases. At $t = 14$ s the magnet rotation is reversed, resulting in fluid transport in the opposite direction. At the end the cilia are switched back to their initial beat.

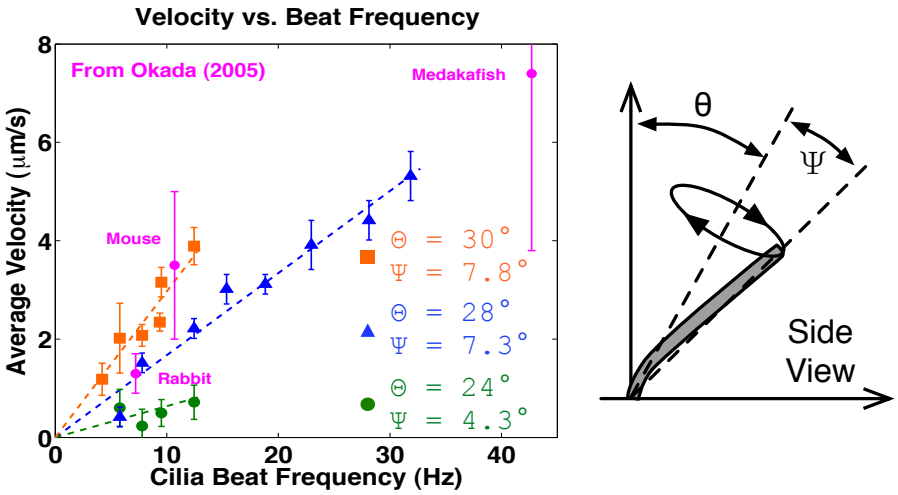

Figure 5.14: Average transport velocity vs. cilia beat frequency in a plane just above the cilia tips for three different tilted conical beats. The beat is described by the tilt angle Θ and half-cone angle Ψ. Least-squares fits demonstrate the linear relationship between velocity and cilia beat frequency.

fluid flow in the embryos of mouse, rabbit, and medakafish with my own data (Okada et al., 2005). These biological species have also demonstrated a correlation between fluid velocity and cilia beat frequency. I note that it should not necessarily be expected that a direct comparison between my data and the biological flow data should match, as the differences, such as cilium length, suggest that the velocities should not be equivalent. However, both sets of data show a similar linear trend in velocity vs. beat frequency, and it is encouraging that my cilia are able to generate flow speeds with characteristic velocities at the same scale as in biology. Finally, I note Okada et al.'s fascinating report that the variation in speeds in each species is accompanied by a difference in node size of the three vertebrates. Remarkably, the ratio of the fluid velocity to the node size is equivalent among each species, suggesting that the Péclet number is a conserved quantity in the node.

5.2.6 Velocity flow profile

Recall that the fluidic cell in my experiments is roughly a rectangular prism, with the floor covered by cilia. At low magnification, I have observed that in a plane near the cilia tips the flow velocity is relatively constant in magnitude and direction over the entire array (except, for example, where there are major defects in the array, as shown in Figure 5.15). As the cell is completely enclosed, it is clear that this driven flow must force a recirculation of fluid elsewhere in the cell such that the net flux, across planes perpendicular to the transport direction, is zero. Thus, the flow is clearly three-dimensional and will vary across the cell, particularly near the boundaries.

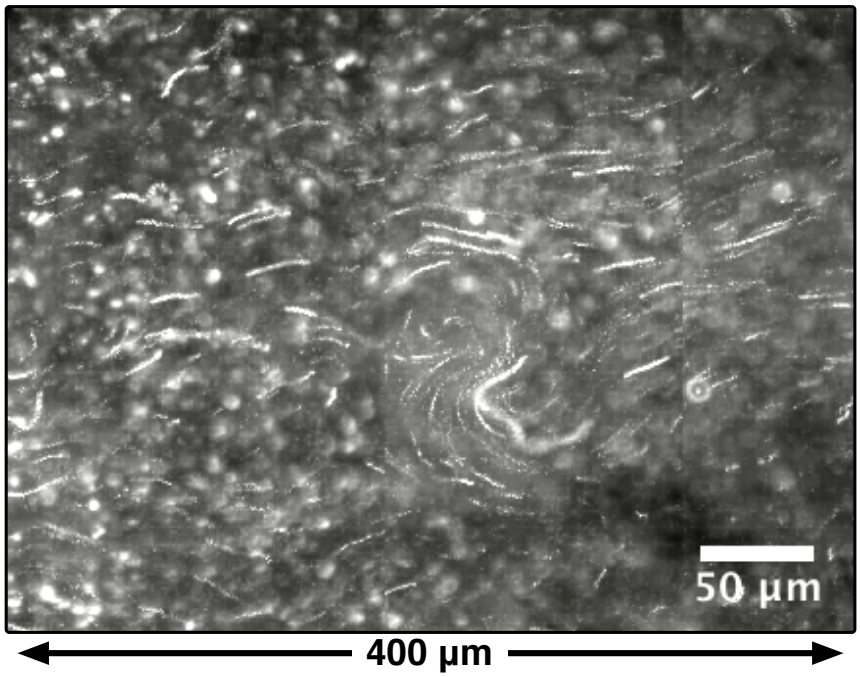

Figure 5.15: A low magnification maximum intensity projection of fluorescent tracers in long-range, cilia driven flow over 9 seconds. The single merged image is stitched together from crops of three adjacent fields of view at 10x magnification, and demonstrates the relatively constant flow over hundreds of microns. The rotational motion near the center of the image signals a patch where a number of cilia did not survive fabrication. As the fluid enters the void it temporarily moves in the opposing direction before rejoining the main transport.

However, for now I will only consider the velocity profile $u(z)$ in the vertical direc-

tion, at a region of interest near the center of the array. I define the transport direction as the y-axis and assume that this velocity profile is constant across the cell along the x-axis, essentially ignoring for the moment the effect of the lateral walls on the fluid flow. Such an assumption is increasingly valid for $w > h$, and the dimensions of a typical fluidic cell in my experiments are $h = 200\ \mu m$ and at least $w = 1\ mm$.

To measure the velocity profile I took 40 second videos of fluorescent tracer motion at a number of horizontal planes above and below the cilia tips. As controls, in each video I turned off the cilia at $t = 30\ s$ to observe the Brownian motion of the tracers with the cilia motionless (aside from the cilia's own thermal motion, which is typically small). In all experiments, extreme care is taken with sealing the fluidic cell to prevent evaporative currents or other sources of drift.

In Figure 5.16 I display maximum intensity projections of tracer motion at selected planes at or above the cilia tips over 30 seconds (recall that in Chapter 6 I will compare this transport with the flow below the cilia tips). As previously mentioned, the fluid flow has a maximum average velocity at the height of the cilia tips, as represented in the projections by longer particle trajectories. I also observe a slow recirculation of fluid, moving in the opposite direction as the main transport, near the chamber's upper boundary due to the enclosed nature of the flow cell, as expected. This recirculation has also been reported in the enclosed nodal pit (Okada et al., 2005; Nonaka et al., 2002). Finally, in the transition from bulk transport to recirculation the tracer particles actually move perpendicular to the transport direction, but slowly, and are actually moving in the vertical direction as well, as they rapidly go out of focus and join one of the two more rapid flows.

Video-tracking of a subset of the particles and calculating the average velocity, in the transport direction, allows me to construct a velocity profile, with results displayed in Figure 5.17. The main features described above are apparent in the profile. Also

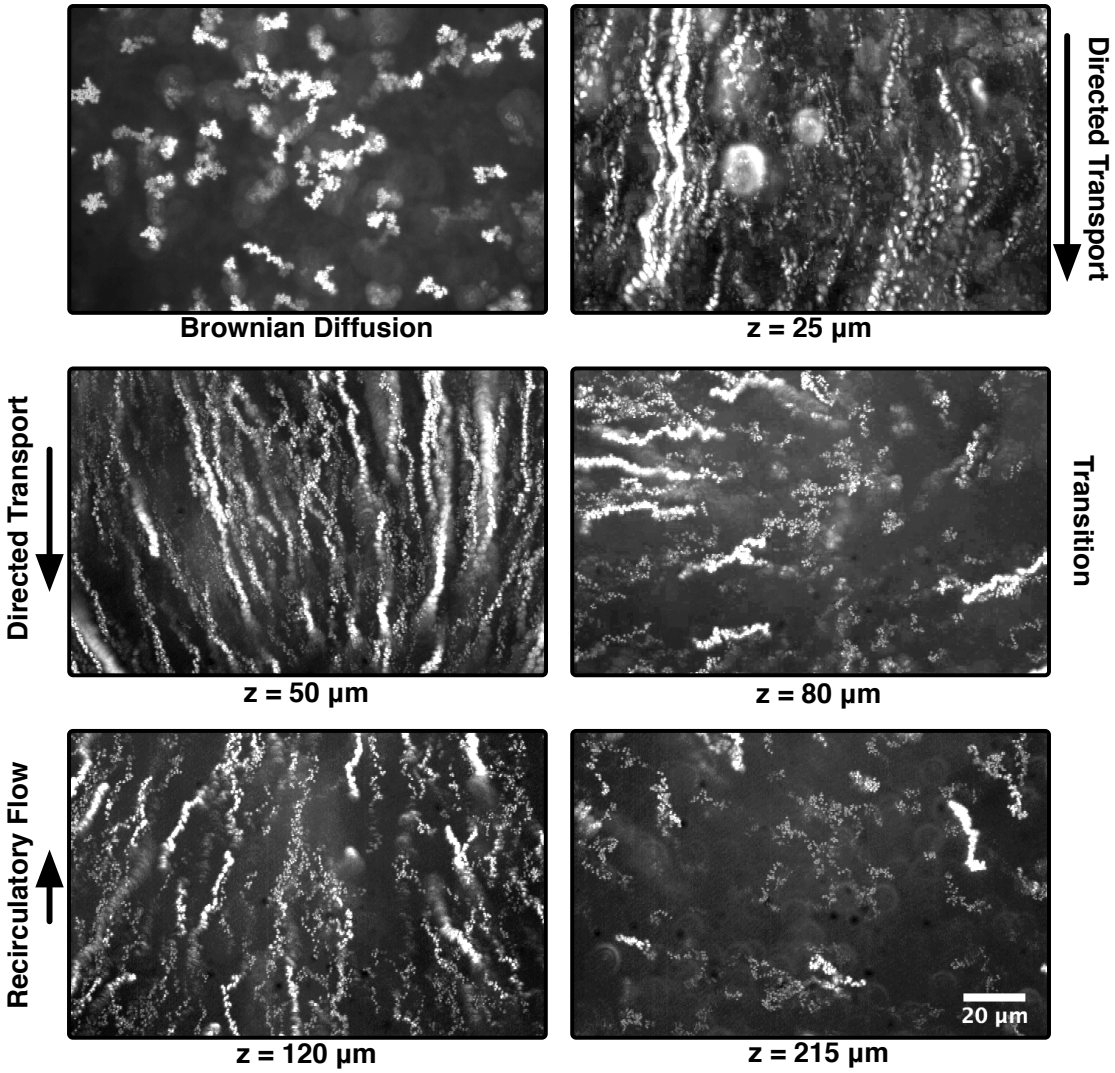

Figure 5.16: Maximum intensity projections of 30 seconds of fluorescent tracer motion. The first panel is Brownian motion, with the cilia turned off, and the other panels are cilia-driven flow at various heights above the cilia tips. The main transport is towards the bottom of the image. At $z = 80\ \mu m$ the main transport is transitioning to the recirculatory flow, and the tracers at this height actually move laterally, briefly, before going out of focus and joining either the main transport or the recirculatory flow. At $z = 120\ \mu m$ the flow is moving upwards, opposite the main transport direction. Finally, near the upper boundary the transport is very slow due to the no-slip condition, and the particle motion looks essentially diffusive.

note that the average velocity decays rapidly below the cilia tips. While the speeds are most rapid in this regime, the motion lacks an overall directionality and so the average velocity is very small. Above the cilia tips the average velocity decays much more slowly, until reaching the transition where it becomes the recirculatory flow.

As this velocity profile represents the contribution of a large number of cilia, it is essentially a measurement of the coarse-grained behavior of an array of cilia. To gain insight into the nature of the profile I compared it to one of the superpositional solutions to the Navier-Stokes equations which I discussed in Chapter 2, Poiseuille-Couette (PC) flow, and found excellent agreement. This remarkable result, which is the first closed-form, analytical solution to show agreement with a cilia-driven flow profile (artificial or biological), demonstrates that the collective beating of thousands of cilia behaves coarsely as a simple superposition of shear- and pressure-driven fluid flow.

Velocity profile is Poiseuille-Couette flow

In Figure 5.17 the solid blue curve was obtained as a least-squares fit of the biomimetic cilia-driven velocity profile. I consider only the portion of the velocity profile between the cilia tips (z' = 0) and the upper boundary (z' = h), to equation 2.39. This fit suggests that the collective motion of thousands of cilia generates a velocity profile that can be simply conceptualized as the sum of an effective shear-stress produced at the cilia tips (Couette flow) and an opposing induced pressure gradient generated by the interaction of the fluid with the closed flow cell boundaries (Poiseuille flow). Similarly, Liron recognized that his Stokeslet solutions between parallel plates were not unique, because a pressure-driven flow could be added to the profile without loss of generality (Liron, 1978). Thus, Liron solved for a velocity field due to the Stokeslets, but then included an *ad hoc* Poiseuille flow which gives a family of possible velocity profiles, some of which are qualitatively similar to Figure 5.17 (Liron, 1978). Similarly, Cartwright et

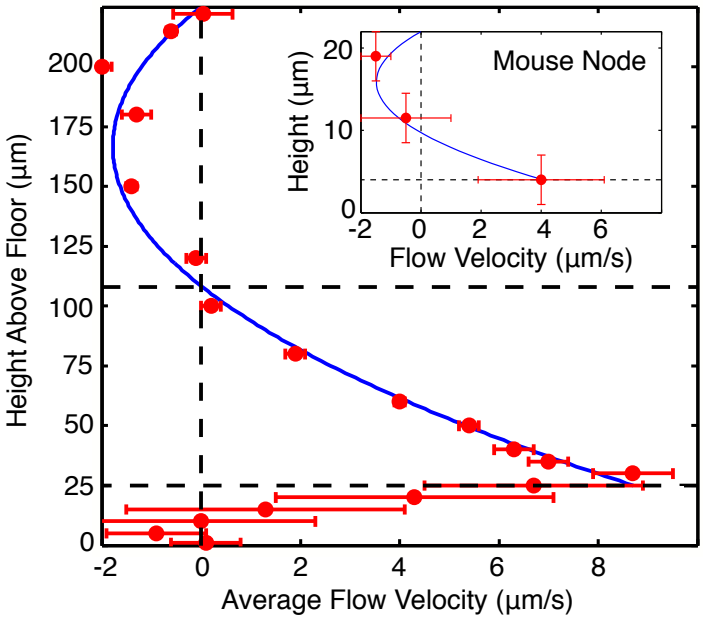

Figure 5.17: The velocity flow profile of biomimetic cilia-driven fluid transport. The points are the tracers' average velocity data in a plane for various heights above the flow cell floor. The solid curve is a least-squares fit to the PC flow profile of equation 2.39 with fit parameters $u_0 = 8.7\ \frac{\mu m}{s}$ and $\nabla p = 1.05\ \frac{Pa}{m}$. The maximum average velocity occurs just above the cilia tips, analogous to the velocity u_0 of the sliding plane in PC flow. Near the top of the fluid chamber we observed a recirculatory flow as expected due to the enclosed nature of the chamber. Inset: Mouse nodal flow velocity data at three heights taken from Okada et al. (2005) (and also plotted in Figure 5.14) and a fit to the PC flow profile with $u_0 = 4\ \frac{\mu m}{s}$ and $\nabla p = 79\ \frac{Pa}{m}$. I attribute the large difference in the pressure gradients between each fit to be due to the overall size of my fluidic cell, which is about an order of magnitude larger than the node.

al. have reported on a computational simulation of the node and calculated a velocity profile that has certain features which qualitatively match the profile in my biomimetic system (Cartwright et al., 2008). However, I stress that neither of these solutions were analytical descriptions of the flow.

I also compare this model with limited biological measurements taken in a mouse embryo. Okada et al. (2005) reported the mouse nodal flow velocity at three heights above the node floor (Okada et al., 2005). In the inset in Figure 5.17 I plot these three data points along with a least-squares fit to equation 2.39, demonstrating that the time-averaged velocity profile in the embryonic node is also consistent with the PC flow model. This is the first wholly analytical solution to be identified which is consistent with the fluid flow in the embryonic node, or more generally, in any biological ciliated system. It is also the first report of any correspondence between the fluid flow in an artificial and biological ciliated system.

Recirculatory flows

I note that integrating either fit to equation 2.39 over the height fails to give zero net flux as should be expected for a closed geometry. Previous work by Liron has demonstrated that this behavior can be due to a portion of the return flow which is recirculated around the periphery of the system (Liron and Meyer, 1980). This is likely the explanation in my system as well, as such a peripheral recirculation can also be seen in the embryonic node in supplemental videos from Okada et al. (2005) (Okada et al., 2005).

There has also been some discussion and controversy about the existence of a secondary recirculation along the floor of the embryonic node. As mentioned above, Cartwright et al.'s simulation of the node largely matched my velocity profile. But it also predicted this secondary floor recirculatory flow (Cartwright et al., 2007), which is

much different from Figure 5.17 in the region below the cilia tips. However, Cartwright's most recent work further predicts that the velocity of this floor recirculation is sensitive to the ratio of the cilia length to the node depth (Cartwright et al., 2008). In both the node and my system this ratio is on the order of 0.1, and Cartwright's model predicts a small velocity which, in reality, is likely dominated by the rapid, complex fluid motion below the cilia tips. While Cartwright et al.'s simulations are time-independent, other work by Smith et al (2007), which is time-dependent, supports this notion. Thus, it is expected that in the embryonic node there is no detectable floor recirculation as well.

5.3 Volume Flow Rate of an Array of Cilia

The volumetric flow rate driven by a collection of cilia is an important measure for biological cilia, as well as a critical measure of pumping performance in the context of a microfluidic device. This bulk flow rate is the cumulative result of fluid flow generated by each cilium, but in general it will not be a simple sum of their individual contributions. This is because the cilia interact with each other in ways that are difficult to predict because the theoretical solutions for a single cilium cannot be simply added together, due to the fact that the no-slip condition on each cilium cannot be satisfied simultaneously. Thus, another critical goal for the coarse-graining of cilia-driven fluid flows is the ability to predict the bulk flow from knowledge of the ciliary beat shape.

However, theoretical analyses are severely limited in their ability to predict the interactions of neighboring cilia and it is therefore difficult to predict bulk flow rates from knowledge of the beat shape of individual cilia, especially at high cilia densities. The ability to make such predictions would be another invaluable tool for understanding the coarse-graining of cilia-driven fluid flow. For the case of the tilted conical beat of nodal cilia, a recently published result uses resistive force theory to derive the volume flow rate as a function of the cilia beat parameters.

Resistive Force Theory. Developed by Gray and Hancock (Gray and Hancock, 1955), resistive force theory is an approximate form of slender body theory, which considers a cilium as a distribution of point forces, or Stokeslets, along the cilium's centerline. For a slender body of length L parameterized by $\mathbf{X}(s,t)$, where s is the arc length with $0 \leq s \leq L$, resistive force theory gives the force density as

$$f_j = C_T \left[\frac{C_N}{C_T} \delta_{jk} - \left(\frac{C_N}{C_T} - 1 \right) \frac{\partial X_j}{\partial s} \frac{\partial X_k}{\partial s} \right] \frac{\partial X_k}{\partial t} \tag{5.7}$$

where δ_{jk} is the Kronecker Delta and I have used the summation convention. The parameters C_N and C_T are the resistance coefficients for normal and tangential motion, respectively. For the tilted conical beat, Smith et al. recently used this approximation to derive the volume flow rate per cilium (Smith et al., 2008). Using the tilt angle Θ, half-cone angle Ψ, and the angular beat frequency ω, they give the parameterization of the beat

$$\begin{aligned} X_1 &= s sin\Psi cos\omega t, \\ X_2 &= -s sin\Psi sin\omega t cos\Theta - s cos\Psi sin\Theta, \\ X_3 &= -s sin\Psi sin\omega t sin\Theta + s cos\Psi cos\Theta. \end{aligned} \tag{5.8}$$

Using their axes definitions the transport is in the x_1 direction, and so the force distribution is given as

$$f_1 = C_T \left[\frac{C_N}{C_T} \frac{\partial X_1}{\partial t} - \left(\frac{C_N}{C_T} - 1 \right) \left(\frac{\partial X_1}{\partial s} \frac{\partial X_1}{\partial t} + \frac{\partial X_2}{\partial s} \frac{\partial X_2}{\partial t} + \frac{\partial X_3}{\partial s} \frac{\partial X_3}{\partial t} + \right) \right]. \tag{5.9}$$

Performing the partial derivatives gives the simple result

$$f_1 = -C_N \omega s sin\Psi sin\omega t. \tag{5.10}$$

Returning to slender body theory, the volume flow rate at time t is given as

$$\int_0^L \frac{X_3(s,t)}{\pi\eta} f_1(s,t) ds \tag{5.11}$$

and so the mean volume flow rate is this result, integrated over one beat cycle and divided by the beat cycle period $T = {}^{2\pi}/_{\omega}$, or

$$\tilde{Q} = \frac{C_N \omega L^3}{6\pi\eta} sin^2\Psi sin\Theta \tag{5.12}$$

5.3.1 Theoretical flow rate for a biomimetic cilium

To evaluate the volume flow rate for a single cilium from resistive force theory (eq. 5.12) I need only calculate the normal resistance coefficient C_N, as the other parameters are either known or can be measured from video of the cilia actuation. There

are various methods in the literature for calculating C_N. Smith et al. use the result

$$C_N = \frac{8\pi\eta}{1 + 2\ln\left(\frac{2q}{a}\right)} \tag{5.13}$$

where a is the diameter and q is a length parameter of order $O(a\sqrt{L/a})$ (Smith et al., 2008). For a typical biomimetic cilium I have $a = 0.75\ \mu m$ and $L = 25\ \mu m$ for $q = 4.3$, which gives $C_N = 1.36\pi\eta$. Substituting this into equation 5.12 gives the theoretical volume flow rate for my typical biomimetic cilium as

$$\boxed{\tilde{Q} = 0.23\omega L^3 sin^2\Psi sin\Theta.} \tag{5.14}$$

The average beat parameters of the cilia driving the velocity profile of Figure 5.17 were $\Theta = 7.1 \pm 0.6°$, $\Psi = 6.3 \pm 0.6°$, and $\omega = 2\pi(34 \pm 3\ Hz)$, which gives

$$\tilde{Q} = 1.3 \pm 0.4\ {}^{pL}/_{s} \text{ per cilium.}$$

Lastly, I note an interesting aspect of equation 5.14, that the volume flow rate a cilium can produce with a given beat shape does not depend on the fluid viscosity. This is another reflection of low Reynolds number fluid flow: the motion of the fluid only depends upon the motion of the surfaces in the fluid.

5.3.2 Validity of theoretical flow rate

This result is reasonable, considering that, for these 25 μm tall cilia beating at 34 Hz, 1.3 ${}^{pL}/_{s}$ is equivalent to each cilium transporting a volume equal to a cube 11 μm on a side per second. However, it is important to note that the derivation of this result assumes the cilium is beating in a semi-infinite space, with no upper boundary. In fact, as in the case of a single Stokeslet, once an upper boundary is present, and the

cilium is no longer in a semi-infinite space, the volume flow rate predicted by slender body theory becomes zero (Liron, 1978). However, in that case particle pathlines can still move significant distances away from the cilium before returning. Thus, for an array of cilia where particles can be transported from cilium to cilium, each cilium can effectively produce a non-zero volume flow rate even with an upper boundary present.

Even with a non-zero flow rate per cilium, however, the volume flow rate per cilium which is achieved in reality will likely not be as large as the prediction of equation 5.14 due to the increased resistance due to the presence of the upper and lateral boundaries, which are not accounted for in the theory. On this line of reasoning, in what follows I will define this result as the maximum flow rate a cilium could produce in a system of negligible resistance, or $Q_{max} \equiv \tilde{Q}$.

5.3.3 Experimental volume flow rate

Experimentally, I can measure the volume flow rate produced by the entire system by noting that for flow in a cell whose width w is larger than its height h (as is the case in both the mouse node and my flow cell) the total volume flow rate can be approximated as

$$Q \approx w \int_0^h |u(z')| dz' \tag{5.15}$$

where $u(z')$ is the velocity flow profile. Note that I use $|u(z')|$ because both the primary flow and the recirculation are attributed to the motion of the cilia array. Performing the integration on the velocity profile of Figure. 5.17 gives an experimental value of $Q^{total} = 460 \pm 50\ pL/s$.

How should this measurement, which is the summed contribution of the entire array, be compared to the theoretical prediction for a single cilium? To do this generally would require knowledge of the interactions between neighboring cilia. It is clear that such interactions will affect the contribution each cilium makes to the bulk flow, and there

is much ongoing work on the study of these cilia-cilia interactions (Mitran, 2007).

In the following subsection, I will use an analogy between classical pumps and cilia in order to arrive at theoretical limits on the bulk flow rate. These limits encompass my experimental measurement and are considered for the opposing cases of non-interacting and strongly-interacting cilia.

5.3.4 Cilia as classical pumps

A classical example of a pump is the centrifugal pump, which is essentially a rotating impeller that draws liquid into its center and spins it radially outward to continually increase its velocity. At the periphery of the pump housing the water exits the impeller cavity and rapidly slows down, which by Bernoulli's principle increases its pressure, driving fluid flow through the system. The performance of such pumps is governed by the affinity laws, which, based on the characteristics of the pump and the nature of the fluidic system, allows one to perform an operating point analysis to determine the flow rate of the pump. For multiple pumps, which must be configured in either series or parallel with the first, the operating point of the new system can now be determined simply by knowing the number of pumps which are added in each configuration. By considering a single cilium as such a pump, I can place theoretical limits on the volume flow rate of the experimental system. Interestingly, I note that this impeller-driven fluid flow is remarkably similar to fluid flow I have observed in the vortex around a single cilium, as I will discuss in more depth in Chapter 6 (see Figure 6.1).

Characteristic curves of the pump and the system

In order to perform an operating point analysis I must know the characteristic curves of the pump and the characteristic curve which defines the losses in the system. The affinity laws provide the definition of the characteristic curve of the pump. For a

pump operating at speed f, these laws give the following relationships for the volume flow rate per pump $\tilde{Q}$ and the pressure head generated by the pump ΔP :

$$\tilde{Q} \propto f \quad and \quad \Delta P \propto f^2 \tag{5.16}$$

Combining these two laws gives the characteristic 'pump curve'

$$\Delta P \propto \tilde{Q}^2 \tag{5.17}$$

which describes the performance of the pump. The actual pump curve can be defined by two parameters, the system back pressure at which the pump is no longer capable of producing net flow, ΔP_0, and the maximum flow rate the pump could achieve in a system with zero resistance, Q_{max}. Then the pump curve is

$$\Delta P = -\frac{\Delta P_0}{Q_{max}^2} Q^2 + \Delta P_0 \tag{5.18}$$

or

$$\boxed{\Delta P = -\frac{\Delta P_0}{Q_{max}^2}(Q^2 - Q_{max}^2).} \tag{5.19}$$

Next, I need to determine the system curve for a fluidic channel. If I assume that the large majority of the losses in the system are due to friction with the channel walls, then the system is described by the Darcy-Weisbach equation

$$\Delta P = f_f \frac{L}{D_H} \frac{\rho v_{avg}^2}{2} \tag{5.20}$$

where f_f is the Darcy friction factor, L is the channel length, D_H is the hydraulic diameter of the channel, ρ is the fluid density, and v_{avg} is the average velocity of the fluid (Happel and Brenner, 1963). Thus, in general the system curve will be quadratic

in the velocity of the fluid.

However, in low Reynolds number Stokes flow, the Darcy friction factor is inversely related to the the Reynolds number $Re = \frac{\rho v_{avg} D_H}{\eta}$, and proportional to some geometric factor g which depends on the channel cross section, so I can write $f_f = \frac{g}{Re}$. Substituting this Stokes flow result into the Darcy-Weisbach equation I get

$$\Delta P = \frac{g\rho}{2Re}\frac{L}{D_H}v_{avg}^2 = \frac{g\eta L}{2D_H^2}v_{avg} \tag{5.21}$$

Finally, to obtain the system curve I need to know v_{avg} in terms of the volume flow rate Q. In any channel the volume flow rate is simply the average velocity multiplied by the cross-sectional area A, or $Q = Av_{avg}$. Solving for v_{avg} and substituting the result into equation 5.21 I arrive at the Hagen-Poiseuille equation

$$\Delta P = \frac{g\eta L}{2AD_H^2}Q. \tag{5.22}$$

Thus, while the Darcy-Weisbach equation goes as v_{avg}^2 (or Q^2), at low Reynolds number the system curve becomes linear in Q. I also note that the Hagen-Poiseuille equation is the fluidic analog of Ohm's law, with ΔP analogous to the voltage, Q the current, and a resistance R determined by the fluid and channel geometry. Thus, I can write the system curve as

$$\Delta P = RQ, \quad R \equiv \frac{g\eta L}{2AD_H^2}. \tag{5.23}$$

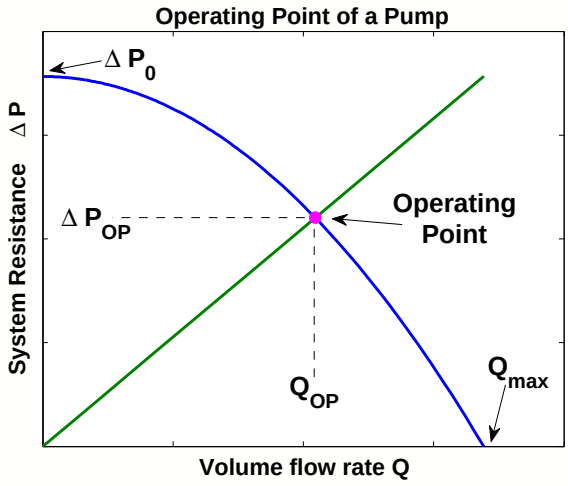

Figure 5.18: The operating point of a single pump, determined by the intersection of the pump curve and the system curve.

System curve for rectangular channel. In microfluidics, channel cross-sections are typically rectangular due to the use of photolithography for defining channel features. For a rectangular channel of height h and width w, the hydraulic diameter is $D_H = \frac{2hw}{h+w}$ and the cross-sectional area is $A = hw$. There are a number of methods for determining the friction factor for a rectangular channel. Shah and London (Shah and London, 1978) use a series in the channel aspect ratio $\alpha = h/w$ ($\alpha < 1$)

$$f_f = \frac{g}{Re}, \qquad g = 24^*(1 - 1.3553\alpha + 1.9467\alpha^2 - 1.7012\alpha^3 + 0.9564\alpha^4). \tag{5.24}$$

In a typical experiment I have $w = 1000\ \mu m$ and $h = 225\ \mu m$, giving $\alpha = 0.225$ and $g = 24^*0.7767$.
Thus, for my typical rectangular channel the Hagen-Poiseuille equation (5.22) is

$$\Delta P = \frac{2.33\eta L(h+w)^2}{h^3w^3}Q. \tag{5.25}$$

and I will define the rectangular channel system curve as

$$\boxed{\Delta P = RQ, \quad R = \frac{2.33\eta L(h+w)^2}{h^3w^3}.} \tag{5.26}$$

Operating point of a system of pumps

Knowledge of the pump and system curves is sufficient to determine the operating point, which is the intersection of the two characteristic curves

$$RQ_{OP} = -\frac{\Delta P_0}{Q_{max}^2}(Q_{OP}^2 - Q_{max}^2) \tag{5.27}$$

as pictured in Figure 5.18. The solution of this (I am interested only in the positive root) gives the operating point

$$Q_{OP} = \frac{Q_{max}^2 R}{2\Delta P_0}\left(-1 + \sqrt{1 + \frac{4\Delta P_0^2}{Q_{max}^2 R^2}}\right), \quad \Delta P_{OP} = RQ_{OP}. \tag{5.28}$$

I have derived this, thus far, for a single pump. What is the effect on the system for including additional pumps in series or parallel? For pumps in parallel, there is no effect on ΔP_0, the maximum pressure head the pumps can overcome. However, each pump transports distinct volumes of fluid and so the maximum possible flow rate becomes $Q_{max}^{total} = n_p Q_{max}$, where n_p is the number of pumps added in parallel. Conversely, for pumps configured in series, which sequentially transport identical fluid volumes, there is no effect on Q_{max}^{total}, while each pump in series does increase the total pressure generated such that $\Delta P_0 \rightarrow n_s \Delta P_0$. These characteristics of pumps in parallel and series are depicted generically in Figure 5.19. Thus, for a system of pumps I can use these substitutions to get the new operating point

$$\boxed{Q_{OP} = \frac{n_p^2 Q_{max}^2 R}{2 n_s \Delta P_0}\left(-1 + \sqrt{1 + \frac{4 n_s^2 \Delta P_0^2}{n_p^2 Q_{max}^2 R^2}}\right), \quad \Delta P_{OP} = RQ_{OP}.} \tag{5.29}$$

Theoretical limits on volume flow rate

To evaluate the operating point of the system, the parameters which govern the pump performance, Q_{max} and ΔP_0, must be known, as well as the system resistance R. As previously mentioned, as the resistive force theory derivation of the volume flow rate per nodal cilium (eq. 5.14) was performed in a semi-infinite space, I will define this result as the maximum flow rate a single cilium can obtain, or $Q_{max} = 1.3 \pm 0.4\ ^{pL}/_{s}$. However, there is no clear way to evaluate ΔP_0 for a nodal cilium, and so in general I cannot actually predict the operating point of the system. By itself, the knowledge of Q_{max} is only enough to specify theoretical limits on the total volume flow rate. The calculation of these limits then becomes a counting problem, which is to say that I need only specify the number of cilia which can effectively be taken as beating in parallel.

As mentioned, the fluidic interactions between nearby cilia are not well understood. To specify these limits I will consider the extremes of cilia-cilia interactions, namely non- and strongly-interacting cilia. As this is Stokes flow, in the absence of interactions between cilia the flow field is simply a superposition of the flow field around each cilium. In this case, I would expect that the total volume flow rate would be the linear sum of each cilium's contribution, or $Q_{max}^{total} = NQ_{max}$. This statement is the equivalent of a

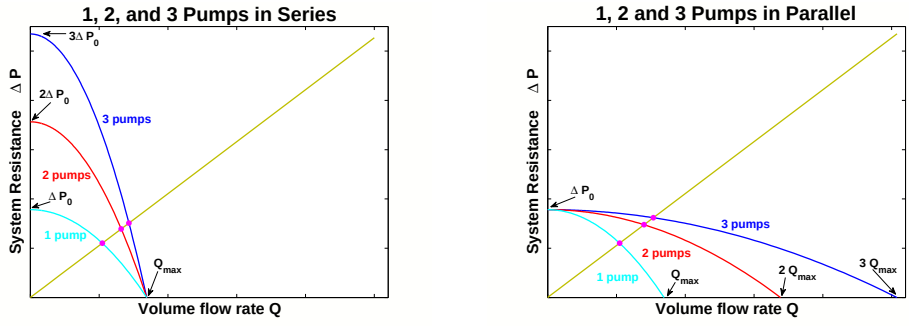

(a) 1, 2 and 3 pumps configured in series.

(b) 1, 2, and 3 pumps configured in parallel.

Figure 5.19: Characteristic curves of systems of pumps in series or parallel.

sparse array of cilia in the experiment, and each cilium is treated as effectively in parallel with the others such that $n_p = N$. For my velocity profile experiment I have $N \approx 3,000$, and so non-interacting cilia give an upper limit on the total, maximum possible flow rate of $Q_{max}^{total} = 3,900\ ^{pL}/_{s}$. This upper bound is well above the experimental value of $460\ ^{pL}/_{s}$, however as I have said the actual operating point of the model would further depend on losses in the system and the pump parameter ΔP_0.

In contrast, for strongly-interacting cilia I assume that only cilia arrayed across the width of the fluid cell, perpendicular to the transport direction, would behave as classical pumps in parallel. The rest of the cilia, arrayed down the channel, would then act as pumps in series, each of which would make no contribution to Q_{max}^{total}. In the velocity profile experiment I have $n_p \approx 55$, giving a lower bound of $Q_{max}^{total} = 72\ ^{pL}/_{s}$.

Thus, my experimental value falls within upper and lower bounds considered for non- and strongly-interacting cilia treated as classical pumps. In the case of the lower bound, the analogy with classical pumps predicts a value that significantly underestimates Q_{max}^{total}. I note that this discrepancy implies that cilia arrayed down the length of the channel are actually able to make an effective contribution to Q_{max}^{total}, in violation of my assumption that they behave as classical pumps. However, this implication is interesting because it suggests the possibility that future experiments performed by varying the number of cilia in an open-ended channel could shed further light on the effective interactions between beating cilia in an array.

Chapter 6

ENHANCED DIFFUSION AND MIXING

"It is possible that the motions to be discussed here are identical with the so-called 'Brownian molecular motion'; however, the data available to me on the latter are so imprecise that I could not form a definite opinion on this matter. If it is really possible to observe the motion to be discussed here, along with the laws it is expected to obey, then classical thermodynamics can no longer be viewed as strictly valid even for microscopically distinguishable spaces, and an exact determination of the real sizes of atoms becomes possible."

- A. Einstein, "On the Movement of Small Particles in Stationary Liquids Required by the Molecular-Kinetic Theory of Heat" *Annalen der Physik* 17, (1905)

In addition to the work quoted above, Einstein's work in his *annus mirabilis* also included special relativity and an explanation of the photoelectric effect, for which he was awarded the 1921 Nobel Prize in Physics. While in the public perception relativity theory is generally perceived as his crowning achievement, none of his work can compare to the above in terms of elucidating a fundamental aspect of reality: *what is the world made of?* While relativity and the quantum are of the utmost importance in modern physics and technology, for the average person they have little bearing on

the individual's conception of the everyday world around them, and many people are not even aware of the basic concepts behind either theory. Conversely, the composition of matter has aroused the interest of great thinkers for all of recorded history, from the Greeks' *átomos* to the corpuscles of Newton to Thomson's discovery of the electron, and today most people are likely to be aware of the notion that their world is made up of atoms.

Einstein's key recognition was that the statistics of stochastic events, which for over 100 years had been described by a diffusion coefficient, had an equivalence with the physical process of random thermal motion of microscopic particles, which we now simply know as 'diffusion' (Narasimhan, 2009). Despite the apparent obviousness (in hindsight) of this connection, the equivalence of abstract mathematics with a physical process was novel and another indication of Einstein's genius. Over the century since 1905, diffusion and related topics have remained areas of scientific study, largely due to the increasing recognition of the role of fluid mechanics and transport phenomena in microscale biological processes.

Diffusion, which more simply refers to 'spreading', is useful at the molecular and cellular levels because it provides a means of particle transport without any additional input of energy. This transport is essential for processes such as biochemical signaling, chemosensation, and reaction-diffusion systems. Conversely, other processes, such as chemotaxis, rely on the existence of chemical gradients, the stability of which must compete with diffusion's tendency to eliminate gradients.

Because diffusion can homogenize concentration gradients, it is one means of producing fluidic mixing. Colloquially, mixing is often synonymous with stirring because in the macroscopic world we almost always rely on stirring processes to induce mixing. However, a number of classical works in fluid dynamics emphasize the important distinction between 'mixing' and 'stirring' (Ottino, 1990). Given two separate fluids with

some initial interfacial area, an efficient means of stirring, or 'stirring protocol', will repeatedly stretch and fold the two fluids into one another, typically producing a striated solution with a greatly increased interfacial area between the two fluids. However, in the absence of diffusion this is *all* stirring can ever accomplish. Further stirring will produce ever thinner striations, but the two fluids will never actually mix together. Of course, this entire discussion hinges on the definition of 'fully-mixed', which is largely a question of resolution. In general, there are not standard definitions of what it means to be mixed, and measures of mixing in experimental systems are typically defined in a way which is specific to the experiment. As an example, one measure that has been widely used it the 'interface stretch exponent' χ (Biswal and Gast, 2004), which measures the exponential rate at which striations are stretched such that the thickness of the striation is given by

$$s(t) = s_0 e^{-\xi t} \tag{6.1}$$

where s_0 is some initial lamellar thickness.

Regardless of what it means to be fully-mixed, classical treatments argue that, at some level of resolution, diffusion is a necessary process to produce a truly homogenized fluid. Diffusion is one mechanism which can allow advected particles to move off of fluid streamlines. Thus, during a stirring protocol, diffusion will actually allow for the striations to merge and become mixed. Stirring decreases the time needed to mix a fluid because the increase in interfacial area implies a decreased distance between interfaces, and thus a decreased time required for diffusion to merge the fluids. Thus, stirring and mixing, although related, are actually two separate processes with an important distinction. In section 6.3.2, I will present a newer concept called 'chaotic advection', a dynamical systems phenomenon which has been suggested to allow for complete fluidic mixing even without the aid of diffusion.

Thus, the understanding of many biological fluid-mediated processes, and by exten-

sion the cellular systems which rely on these processes, requires an understanding of how stirring and diffusive processes interact to produce particle transport. In systems with motile cilia, the fluid-driven by the cilia motion creates stirring and results in the advective motion of the particles. Many of these systems also rely on fluid-mediated processes which may be affected by cilia-driven advection. As I discussed in Chapter 3, experimental studies of biological ciliated systems are time-consuming and often difficult to interpret due to the large number of complications with both *in vivo* and *in vitro* studies. For such reasons, to date there is very little experimental data on the detailed motions of cilia-driven particles. Furthermore, theoretical studies of ciliated systems rarely incorporate diffusion because of the added theoretical complexity, instead assuming that advective transport is sufficiently strong to dominate diffusion.

In this chapter, I will continue the discussion of my observations and analysis of driven particle motion in my biomimetic cilia arrays, focusing on the nature of the fluid flow in the flow regime below the cilia tips. I will present two frameworks for the quantitative analysis of these flows, none of which has been applied to cilia-driven fluid flow in the past. It is important for me to clarify that these two frameworks are alternative descriptions of the same phenomena, with some similarities and some differences. Thus, they provide different interpretations of the fluid flow, each of which may be a useful descriptions in appropriate circumstances.

The first framework I describe is that the biomimetic cilia drive a fluid flow below their tips in which the dispersion of advected particles can be approximated as an enhanced diffusion process. This means that particles in this flow may be mixed at a rate which scales in time like a diffusive process, but the rate itself is enhanced over that which would be expected from the intrinsic diffusivity of the particle. This analysis is the simpler of the two frameworks in terms of interpretation, but still provides a substantially more thorough characterization of fluid flow in proximity to a cilia-like

structures than exists in the literature. These statistical results also form the first experimental quantification of the potential for significant mixing in ciliated systems.

The second framework I will describe is more abstract than the first, but provides a richer sense of the possible phenomena which may be present in cilia-driven flows. Broadly speaking, these phenomena fall under the umbrella of anomalous transport, which has also been referred to as strange kinetics. These terms describe dynamical systems in which the transport properties exhibit non-Gaussian statistics, and the phenomena which are encompassed by these terms include chaotic advection and Lévy flights. As I discussed in Chapter 3, chaotic advection has been speculated upon in theoretical treatments (Smith et al., 2007; Fauci and Dillon, 2006), and the single experimental work to address the issue did not support their claims with appropriate evidence (Supatto et al., 2008).

Finally, I note that, in addition to the biological implications, the presence of mixing within our artificial cilia system may also be of use in a microfluidics setting. As I have noted, low Reynolds number fluids cannot support turbulent fluid motion. This restriction means that mixing is often diffusive, requiring long time scales. For many microfluidic applications, such slow mixing is the determining factor in how rapidly fluid can be moved through a channel, and thus how long a given experiment will take. For example, microarray biosensors have demonstrated pathogen and toxin detection with volumes of fluid and processing times orders of magnitude smaller than conventional techniques. However, at the low Reynolds number of these devices, current processing times are restricted by the fact that reactions require diffusive transport in order to bring reagent and analyte together. Thus, cilia-driven fluid flows could have possible applications as a magnetically driven micromixer.

6.1 Cilia-Driven Flow: Comparing Flow Regimes

In the introduction to Chapter 5, I described how the cilia-driven particle motion in my fluidic system exhibits distinct flow regimes separated by a plane at the height of the cilia tips. The focus of that chapter was on the directional flow regime above the cilia tips. In that regime, particle motion was highly directional over long ranges, and fairly uniform in average velocity. In this chapter, I turn my focus to the fluid flow regime below the cilia tips. Broadly speaking, the flow field below the cilia tips behaves as an array of vortices, one vortex per beating cilium. Because the cilia are randomly distributed, the interactions between these vortices gives rise to rich particle motion which has not been documented in the literature. Figure 6.1 exemplifies the vortical flow I have observed around each cilium, and shows an 'orbit-and-escape' behavior which I have observed to be typical, and which will be of further relevance to my discussion of anomalous transport in a moment.

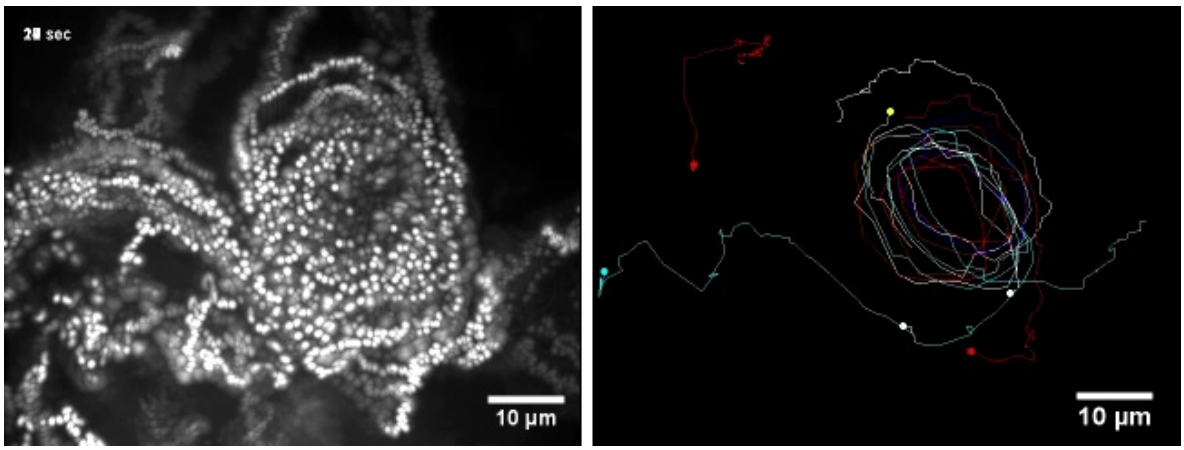

Figure 6.1: Click to Animate. The vortical flow around a single cilium. New tracers repeatedly come under the influence of the vortex, perform some number of revolutions around the cilium, and eventually escape off the left side of the video frame. These types of vortices make the flow below the cilia tips much different from that above.

As with the directed fluid transport, the results presented in this chapter were generated by cilia executing the tilted conical beat of embryonic nodal cilia (Fig-

ure 5.3). However, my observation has been that in all circumstances the actuation of a biomimetic cilium induces a local flow around the cilium which is complex and essentially vortical. Even if the beat shape appears planar, like that of cilia in the airway epithelia, particles still orbit the cilium in local vortices, albeit vortices which appear much more irregular and disordered than the rotational beat. This is displayed by the animation in Figure 6.2, which is unfortunately of poor optical quality and slightly difficult to interpret. However, close inspection shows that the cilia beat is roughly planar, and the particle motion is complex and looks much like the flows I've discussed for the tilted beat. This behavior is likely a result of small deviations from a planar beat, in essence because a perfectly planar beat would be difficult or impossible to achieve. As such, it is my expectation that approximately vortical flow around a beating cilium is a general feature whose existence is largely independent of beat shape. Theoretical treatments of nodal cilia have shown clear vortices, but the strong interactions between airway cilia have prevented any significant modeling of particle pathlines nearby airway cilia, and so I am not aware of a prediction of vortices around airway cilia within the literature.

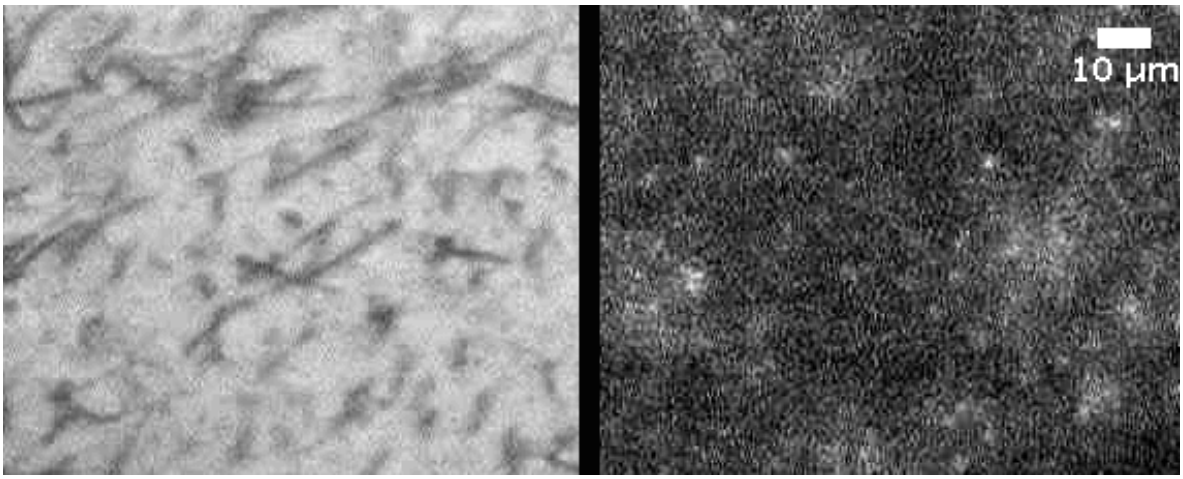

Figure 6.2: Click to Animate: This is, unfortunately, a rather low optical quality movie of the complex flows around cilia executing the planar beat of airway cilia. The vortices around a cilium are present, but much more irregular.

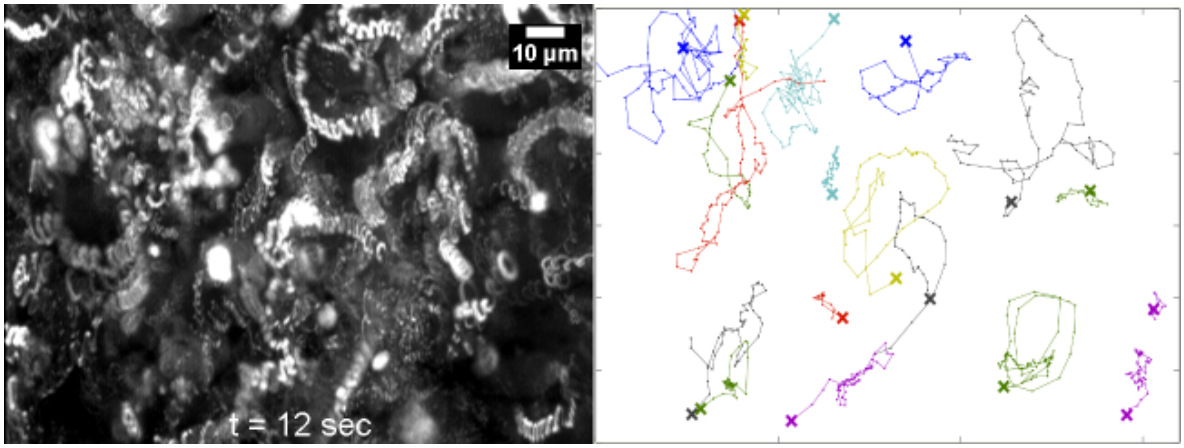

Figure 6.3: Click to Animate. Flow below the cilia tips. At left, poster image displays maximum intensity projection of tracer motion, while movie displays same data played at 4x real time. At right, trajectories of video-tracked particles in the flow.

6.1.1 Flow Below Tips is Rapid and Non-Directional

A broader view of the cilia-driven fluid flow, in the regime below the cilia tips, reveals that particles move as if they were being driven by an array of vortices. In my samples, cilia are distributed at random due to the nuclear track etching process which is used to manufacture the polycarbonate templates. Thus, the array of vortices, one per cilium, are distributed at random as well. As I demonstrated in Figure 6.1, particles can be transiently trapped within such vortices, performing a number of orbits before escaping. After escape from a given vortex, particles typically move rapidly, but with no predictable directionality as I demonstrated for the flow above the cilia tips. These escaped particles will sometimes be caught up in another nearby vortex, while other times they will move through the vortex array without being trapped before exiting the microscope field of view. Figures 6.3 and 6.4 display this type of motion.

To compare the flow below the cilia tips with the uniform, directional transport above the cilia tips discussed in Chapter 5, Figures 6.5 and 6.6 display comparative analyses of the velocities of video-tracked tracer particles in each flow regime. Figure 6.5 shows trajectories of these tracers with the local average velocity mapped to color,

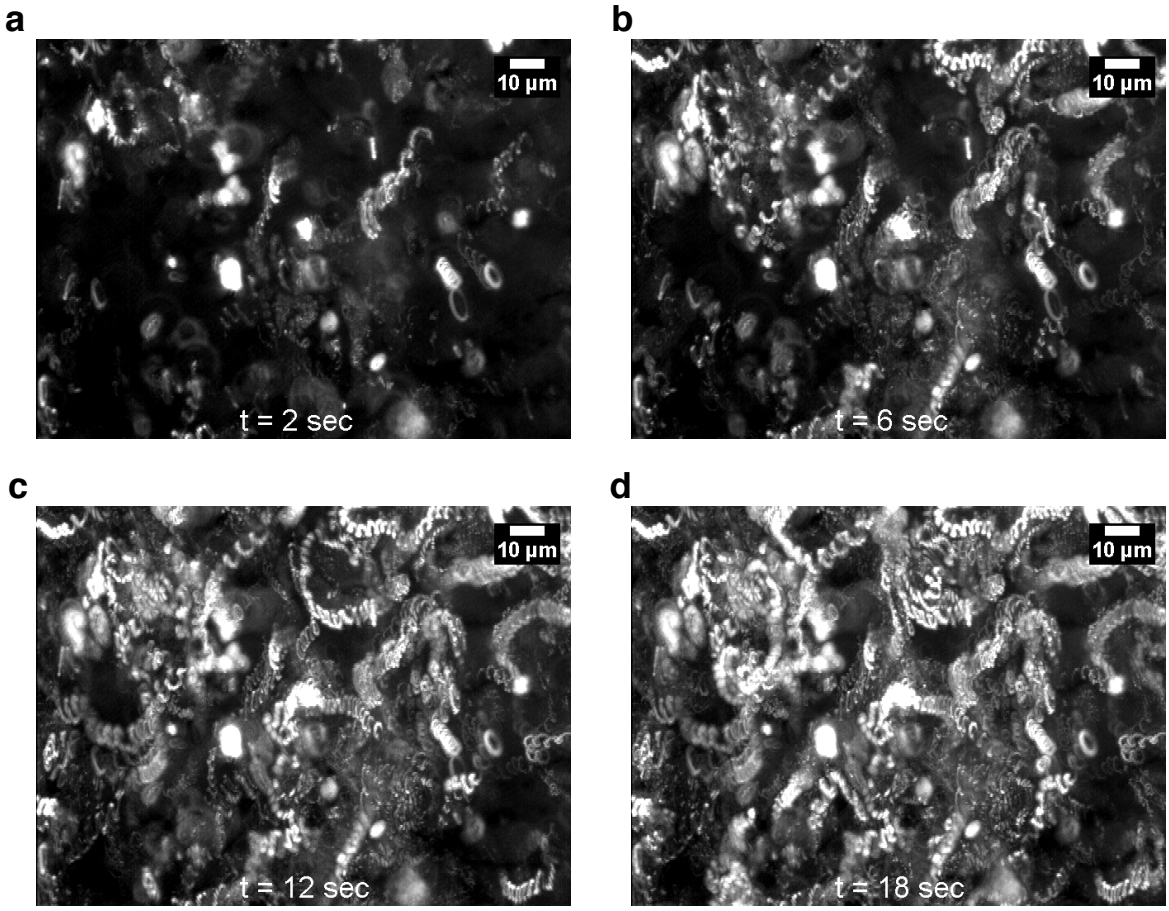

Figure 6.4: Montage of maximum intensity projections of increasing duration, representing cilia-driven tracer motion below the cilia tips. In this regime the flow is very different from the directed transport described in Chapter 5, as particles move haphazardly between the vortices associated with each cilium.

where a sliding average is performed over a 0.25 second time window. Panel (c) serves as a control, displaying the intrinsic diffusive motion of the tracers when the cilia are motionless.

In Figure 6.6a-b the velocity time courses are plotted for the same tracers whose trajectories are shown in Figure 6.5a-b. The plotted velocities are in the direction of fluid transport above the tips, as defined in Figure 6.5a. For each plot, at approximately $t = 30$ seconds the cilia beat is turned off, allowing the tracers to revert to their intrinsic diffusive motion, which serves as an additional control to ensure there is no fluid motion due to evaporative drift. Lastly, Figure 6.6c plots the statistical distribution of the average velocity time courses, including the diffusive motion shown in Figure 6.5c.

Taken together, the panels of Figures 6.5 and 6.6 highlight the dramatic differences in the velocity field between the flow regimes above and below the cilia tips. The tracer trajectories demonstrate the distinct difference in directionality between the two regimes, while the velocity map and velocity time courses reflect the homogeneity of the flow above the tips and the heterogeneity below. This difference is especially evident in the fluctuations in velocity seen in the velocity time courses. As the averaging window used is 0.25 sec and the cilia beat is roughly 30 Hz, these velocity fluctuations are reflective of inhomogeneities in the velocity field rather than changes over the tracer epicycles. Aside from the fluctuations in velocity as a function of time, the ensemble average (over all tracers at all times prior to the cilia being turned off) of the flow below the cilia tips is very close to zero with a large standard deviation, while above the tips the highly directional flow results in a non-zero average velocity with a much tighter standard deviation.

To statistically compare the velocity of tracers in each regime and for the diffusive control, I plot the distributions of average velocities in Figure 6.6c. These velocity distributions are the likelihood of a given average velocity over the 0.25 s averaging

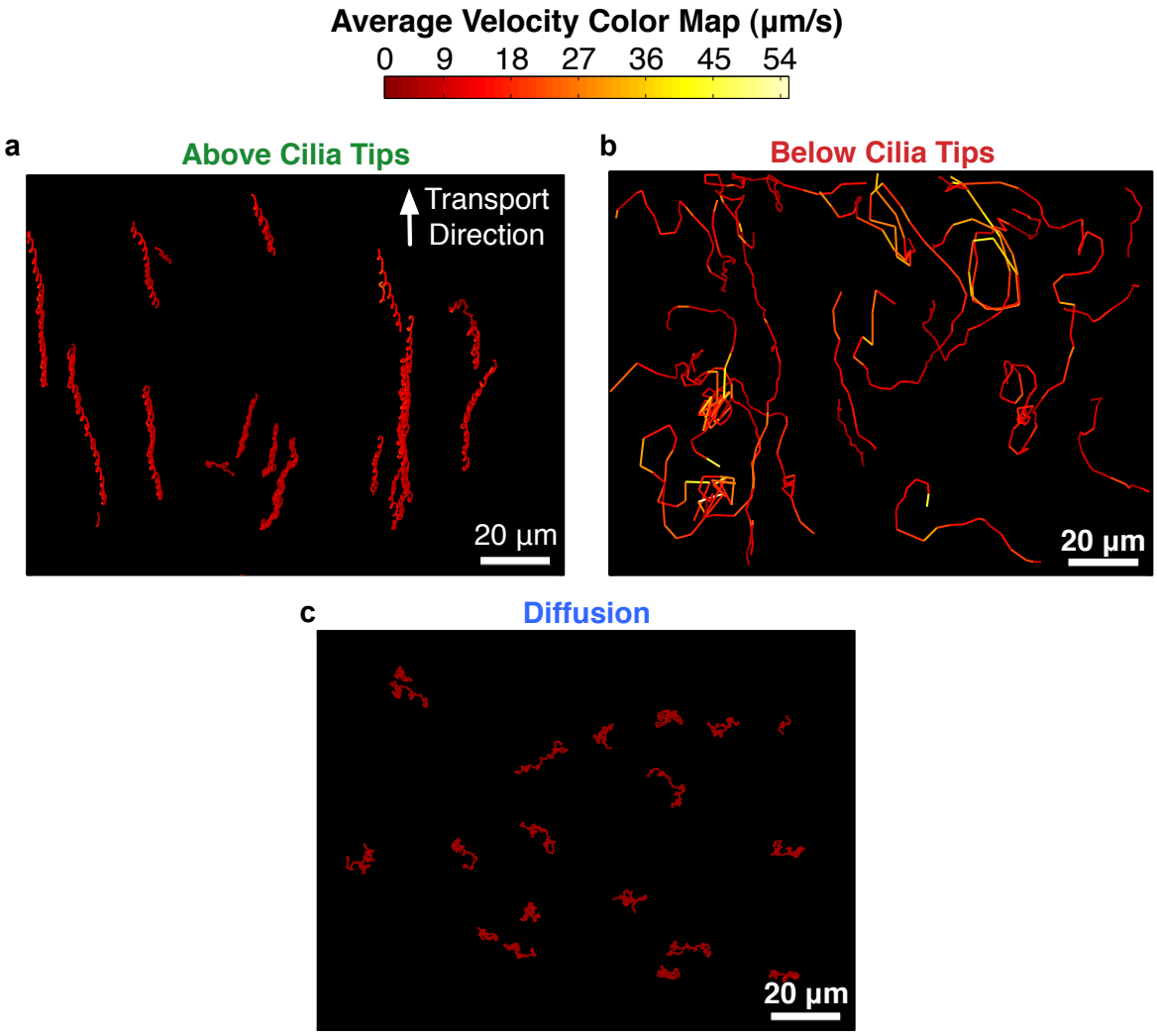

Figure 6.5: A comparison of tracer pathlines in each flow regime as well as for the tracer's intrinsic diffusive motion with the cilia turned off. The tracer pathlines are plotted over a 0.25 s averaging window with the average velocity at that position mapped to color. Each velocity map is scaled to the maximum velocity below the cilia tips in order to compare the heterogeneity of the flow below the tips with that above. Also see Figure 6.6.

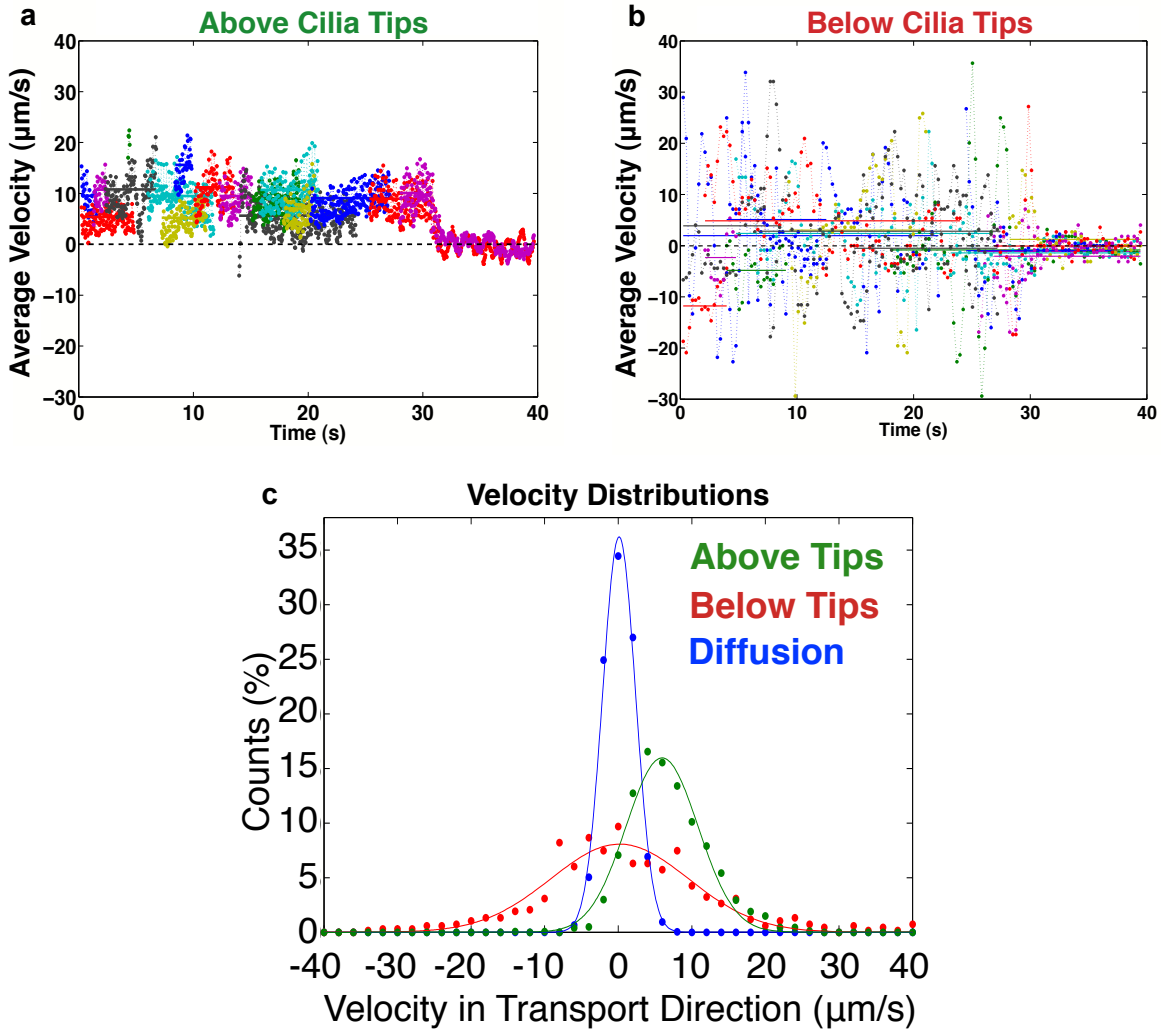

Figure 6.6: (a-b) Comparing tracer velocities (one tracer per color) as functions of time, above ($z = 30\ \mu m$) and below ($z = 15\ \mu m$) the cilia tips, along the axis of the directed transport as shown in Fig. 6.5a. The cilia beat is switched off at roughly $t = 30\ s$, allowing the tracers to revert to their intrinsic diffusive motion. The colored, solid horizontal bars are the corresponding tracer's average velocity over the duration of its tracked motion. The directionality and well-defined ensemble average velocity above the cilia tips is dramatically contrasted by the heterogeneity and lack of an average directionality in the tracer motion below the cilia tips. (c) The probability distributions of the average velocities in (a-b), prior to the cilia turning off, as well as for the diffusive motion shown in Fig. 6.5c. The solid curves are fits to a skew normal distribution, with the distribution means, standard deviations, and skews given in Table 6.1. However, I note that in the anomalous transport section I will demonstrate that the flow below the cilia tips can be fit to a more general class of distribution than I have used here.

Velocity Distributions: Skew Normal Fit Statistics			
Fluid Flow Regime	Mean ($\mu m/s$)	Standard Deviation ($\mu m/s$)	Skew
Above Tips	6.9	5.2	0.5
Below Tips	1.7	9.7	0.2
Diffusion	0.1	2.2	0.0

Table 6.1: Statistics for the distributions in Figure 6.6c, as fit to equation 5.5. Below the cilia tips the fluid flow is essentially mean zero with a large standard deviation, reflective of the heterogeneity of the flow in this regime.

time, or lag time, for all tracers over their entire trajectory (while the cilia are beating). The total number of counts for the distributions exceed 1000 each. As mentioned, this quantity of statistically analyzed flow data is substantially larger than previously published analyses of cilia-driven flow in biological systems.

Einstein showed in his 1905 work that Brownian, diffusive motion of an ensemble of particles along a single dimension $\vec{x}$ should behave as a collection of random walks such that the average particle displacement was $\langle x \rangle = 0$, while the probability of a given position along x as a function of lag time τ should be given by a Gaussian distribution with mean $\mu = 0$, and a standard deviation $\sigma = \sqrt{2D_0\tau}$ where D_0 is the diffusivity. This means that the distribution of particle velocities, in a diffusive process, is expected to have a width given by $\sigma = \sqrt{2D_0/\tau}$.

As I explained in Chapter 6, the velocity distributions are potentially skewed about their means because of a non-constant angular velocity in the cilia's tilted conical beat. In that chapter I used the skew normal distribution to fit this data, with the fits displayed as the solid curves in panel (c). From these fits I can compute the mean, standard deviation, and skew of each distribution using equations 5.6 with the results displayed in table 6.1.

As expected for the control data, the diffusive particle motion is mean zero, has no skew, and has a standard deviation of $\sigma = 2.2$ $\mu m/s$, which implies a diffusivity of $D_0 = \sigma^2\tau/2 = 0.6$ $\mu m^2/s$, about 30% different from its expected value of 0.45 $\mu m^2/s$. The

flow above the cilia tips does have some skew and a clearly non-zero mean, reflecting the directional transport, as I discussed in Chapter 5.

The velocity distribution for the flow regime below the cilia tips is clearly much wider than either the control data or the flow above the cilia tips, demonstrating a significant heterogeneity in the velocity field. Although particles are seen to regularly achieve velocities of $\pm 20 - 30$ $\mu m/s$, the flow is essentially mean zero, demonstrating that just 10 μm below the cilia tips the directionality of the large scale flow has been lost. The distribution below the tips retains a small amount of skew, but otherwise I note that the distribution appears much like the diffusive velocity distribution, but with a substantially larger standard deviation. As I mentioned for the first framework I will use to characterize this data, this suggests that the flow below the tips appears like a diffusive process with a particle diffusivity that is enhanced relative to its expected, intrinsic diffusivity. Just with the diffusive data, if the flow below the tips is considered to be diffusive, then the standard deviation of $\sigma = 9.7$ $\mu m/s$ implies a diffusivity $D_0 = 11.7$ $\mu m^2/s$, and enhancement of 26 with respect to the expected diffusivity. This simple estimate will prove to be fairly consistent with a more robust method for determining the effective diffusivity which I describe below.

To this point, the data I have shown in the flow regime below the cilia tips has been at a single height, $z = 15$ μm. The tracer motion is qualitatively similar at other heights below the tips, except for very near the tips in the transition region to the directional flow regime. For completeness, Figures 6.7 and 6.8 display tracer pathlines and velocity time courses, respectively, at a number of other heights below the cilia tips. The tracer pathlines highlight the dramatic transition from the non-directional flow over $z = 0 - 15$ μm to the uniform directionality at $z = 25$ μm. The tracers at $z = 20$ μm represent the transition zone, where tracers typically begin following tortuous trajectories, but are soon caught up in the directional flow and begin

moving towards the top of the video frame. The velocity time courses also emphasize this transition, as below $z = 20\ \mu m$ the lack of directionality is evident, with large fluctuations in velocity which stem from the heterogeneity in the velocity field. At $z = 20\ \mu m$ a trend in the average velocity away from zero begins to be seen, while at the height of the tips the directional flow has set in.

6.2 Flow Below the Cilia Tips is Effectively Diffusive

A fundamental aspect of any process whereby mass is transported in a fluid is to understand how the displacement scales with time. Of course, the shortest distance between two points is a straight line, which is the simple way of saying that the most rapid means to transport a fluid element from one point to another is with a constant velocity, at least in the absence of turbulence. This type of constant velocity transport, or ballistic motion, is the result obtained by the double integration of Newton's Second Law in a system with zero net force, giving the familiar $r = vt$. Thus, as we are well aware, under ballistic motion the net displacement of an object simply scales linearly with time with a rate given by the constant velocity.

Diffusive processes, on the other hand, produce zero average displacement on the whole, but do generate an root-mean-square (rms) displacement which Einstein derived to be given by $\langle r \rangle = \sqrt{2dD_0t}$ where d is the Euclidian dimension and D_0 is the mass diffusivity (Einstein, 1905). Thus, the expected displacement of an object exhibiting diffusive motion scales with the square root of time, much slower than ballistic motion.

To evaluate the temporal evolution of transport in a given fluid flow a widely used

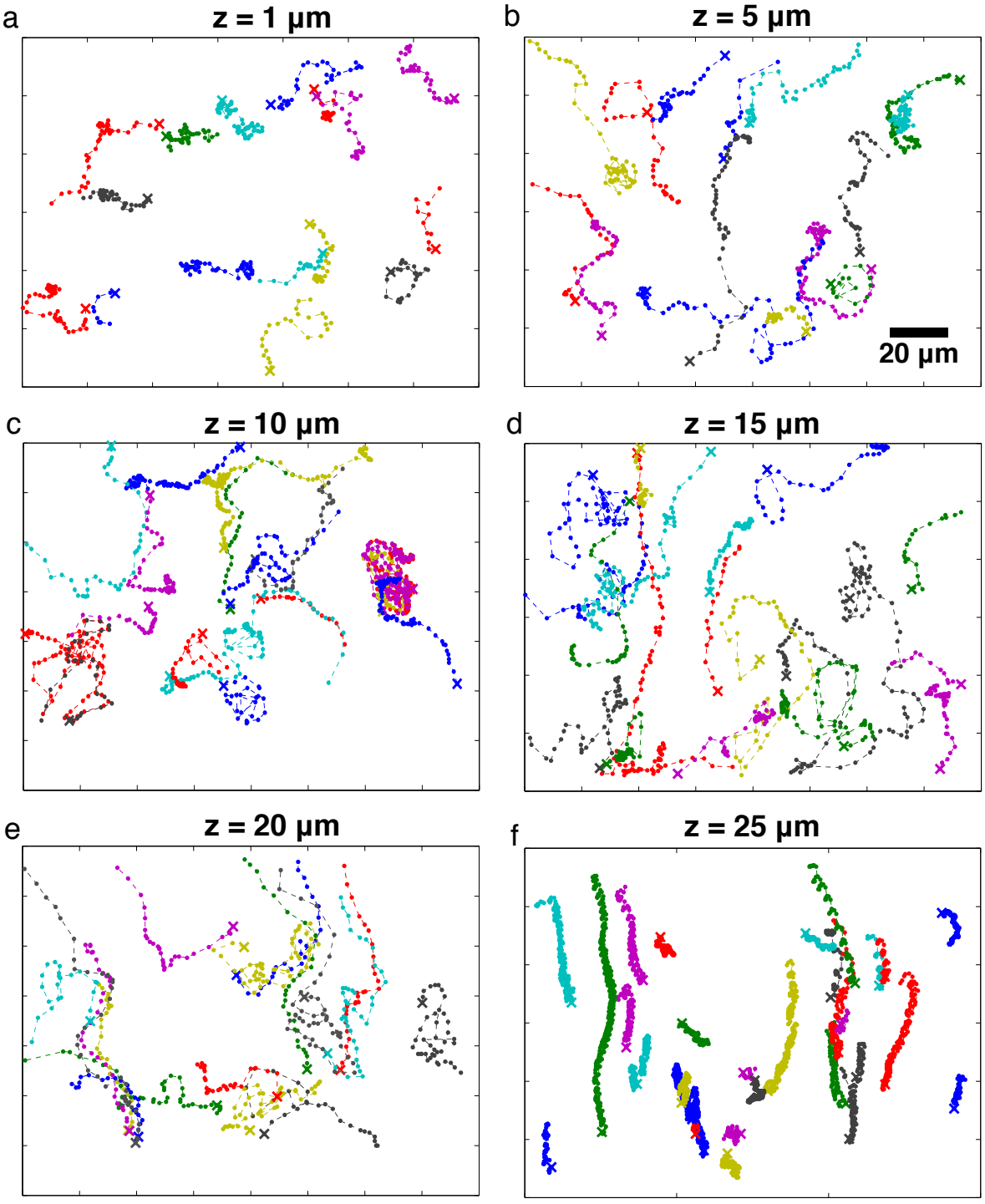

Figure 6.7: Pathlines of cilia-driven tracers in the flow regime below the tips, at various heights between the floor and the height of the tips. The crosses mark the start of each trajectory. Note the scale bar in (b); the width of each video frame is 160 μm. A number of vortices around beating cilia are evident. At $z = 20$ μm the flow begins to transition to the directional transport discussed in Chapter 5, as tracers which initially followed complicated paths are caught up in the transport and driven out of the video frame.

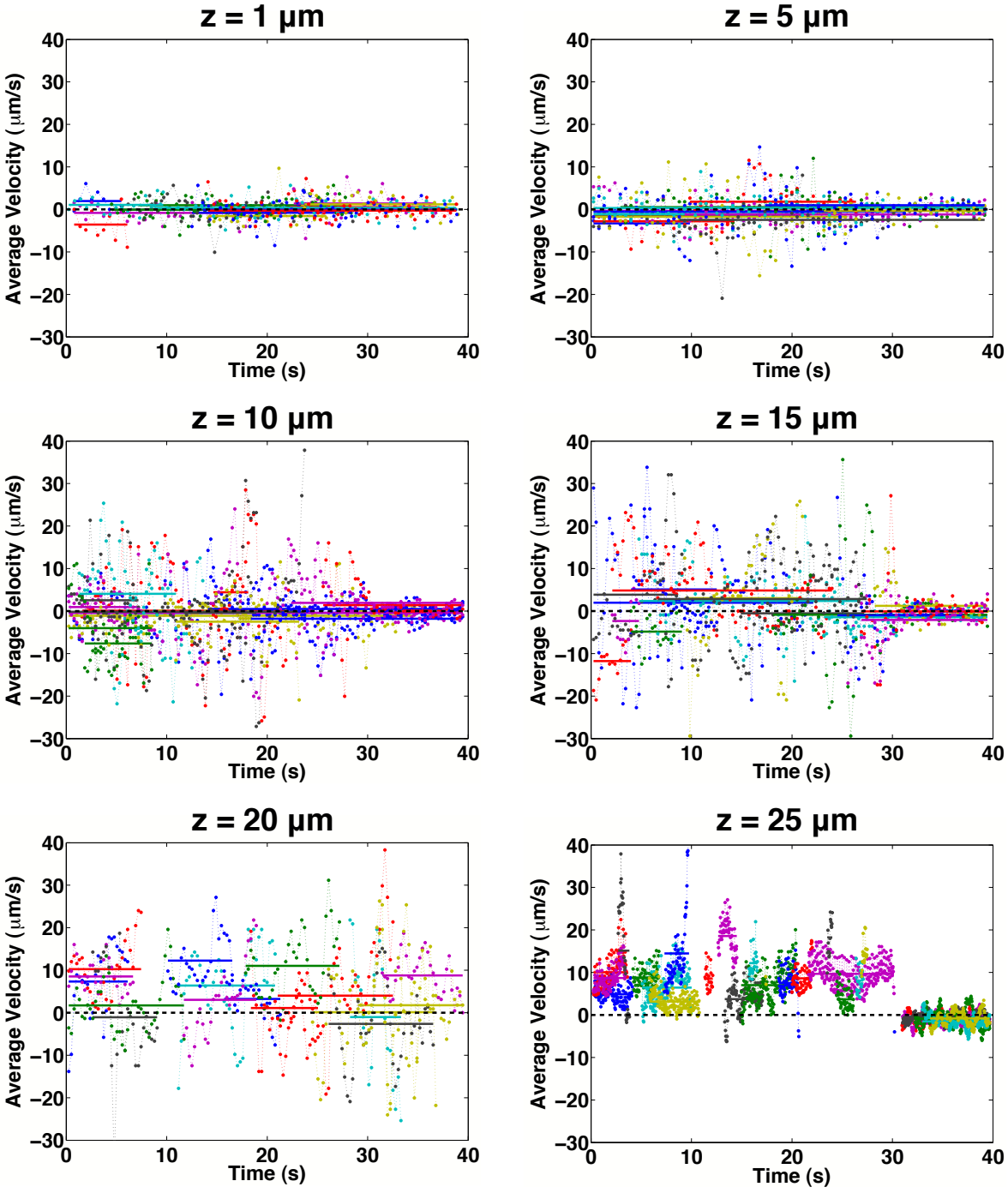

Figure 6.8: A comparison of the time courses of tracer velocities (in the direction of the transport above the tips) for various heights in the flow regime below the tips. The lack of a directionality is evident until the transition region from $z = 20 - 25$ μm, while the velocity fluctuations which imply heterogeneity in the velocity field are most dramatic near the midpoint of the cilia height, at $z = 10$ and 15 μm.

metric is the mean square displacement (MSD) as a function of lag time τ:

$$\langle r^2 \rangle = c\tau^{\kappa}. \tag{6.2}$$

This general form reduces to ballistic motion if $\kappa = 2$, in which case $c = v^2$, and reduces to diffusive motion if $\kappa = 1$, in which case $c = 2dD_0$. In addition, phenomena which inhibit diffusion can lead to $0 < \kappa < 1$, which is referred to as sub-diffusive motion, while in some cases, such as turbulent flow, processes termed super-diffusive can lead to $2 < \kappa \leq 3$.

Briefly I note the important distinction between the use of a lag time τ rather than the absolute time t. While the MSD as a function of time t behaves the same as using a lag time τ, the use of τ treats every point in space as if it were the initial location and calculates the displacement from that point for different lag times. Thus, on a plot of MSD vs. τ, each data point is a property of the *entire trajectory* rather than a representation of any specific moment in absolute time. Typically, MSDs are displayed on a log-log scale such that the form of equation 6.2 becomes $log[\langle r^2 \rangle] = \kappa log(\tau) + log(c)$. Thus, for an isotemporal transport process the slope of the MSD is constant and equal to κ, while the y-intercept of the curve is a function of the rate of transport c.

To understand the temporal scaling of the fluid flow driven by my biomimetic cilia arrays the MSD is advantageous because it will easily discriminate between the constant average velocity motion above the cilia tips and the complex, non-directional flows below the tips. However, the conventional MSD is a measure of how rapidly in time an object moves away from its *initial location*. To address the issue of mixing in biological ciliated systems, a more useful measure is the scaling law with which objects move away *from each other*.

For this reason, in the following analysis I have utilized a technique known as relative dispersion, which is a metric of how the position of one object changes with lag time

relative to other moving objects (Artale et al., 1997; LaCasce and Bower, 2000; Babiano et al., 1990). Conceptually, relative dispersion treats the time course of the separation of two objects as though it were itself a single object. To provide a sense of these 'separation trajectories' Figure 6.9 compares them with the original tracer pathlines for a single height in each flow regime. Note that n original trajectories leads to $(n^2 - n)/2$ separation trajectories. It is immediately clear that the highly directional motion above the cilia tips is strongly suppressed in the separation trajectories, while below the cilia tips the trajectories retain the complexity of the originals.

Relative dispersion, which has been most often used to measure atmospheric and oceanographic tracer transport, still utilizes the MSD to investigate the temporal scaling of the process. However, instead of operating on the displacement $\mathbf{x}(t)$ of an individual object the MSD is calculated for the separation between particles $\mathbf{R}(t) = \mathbf{r}^{(2)}(t) - \mathbf{r}^{(1)}(t)$. As I demonstrated above, in a highly directional, uniform velocity field the particle motion does not lead to an increased separation between particles. In other words, if the flow is truly uniform, then the observation of any increased separation of between particles will be the result of their intrinsic diffusive motion as represented by their relative diffusivity D_0^R. Quickly I note that relative dispersion is not the same technique as two-point microrheology, a similar analysis which looks for correlations in the motion of pairs of particles which are coupled together by a viscoelastic fluid, such as the cellular cytoplasm. In my case, the goal of the relative dispersion calculation is actually to remove correlations due to uniform advection.

Figure 6.10 compares the slopes of linear regressions of the absolute MSD with the MSD of the relative motion of the same tracers for the two fluid flow regimes. This comparison provides a sense of the effect of the relative dispersion calculation. The absolute MSDs are as expected: below the cilia tips the complex nature of the tracer trajectories leads to a temporal scaling which is between ballistic and diffusive, while

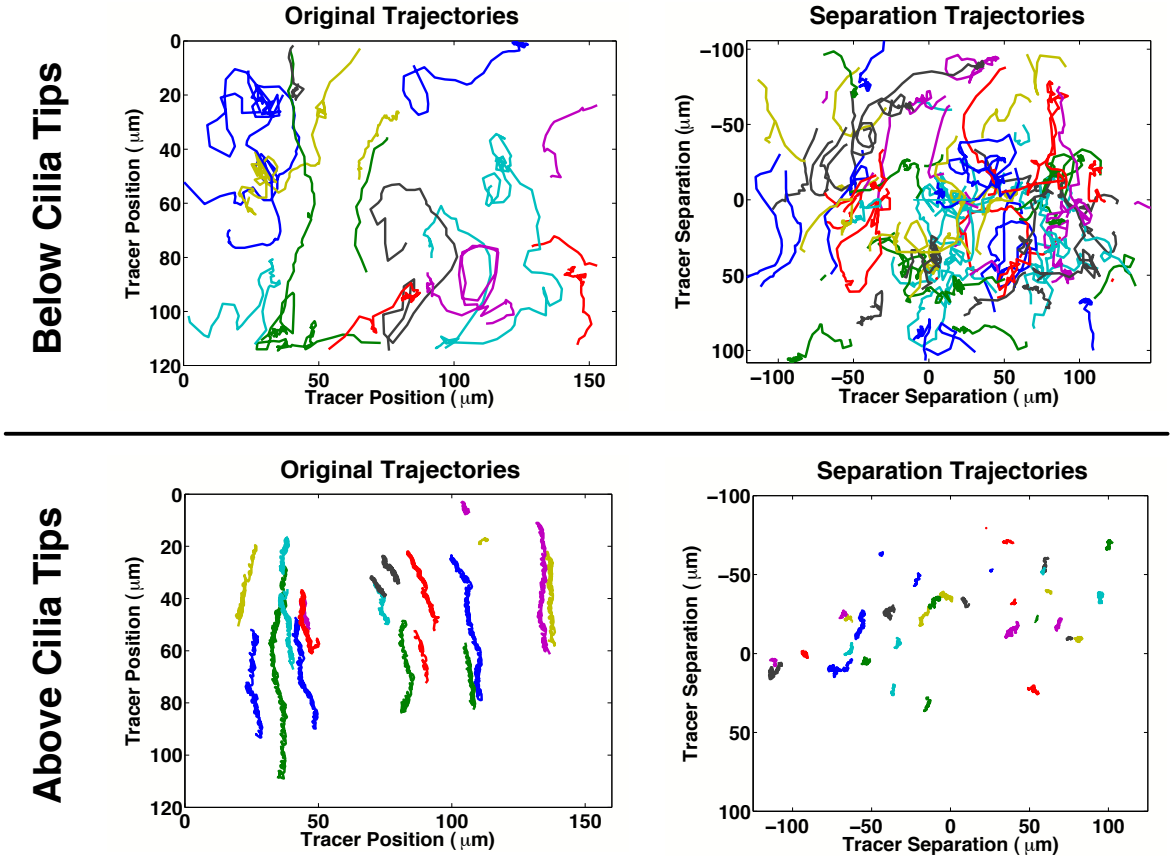

Figure 6.9: A comparison of the original (absolute) particle trajectories with the 'separation trajectories', in which the separations between all particle pairs are treated as if they were also trajectories. In the flow regime below the cilia tips the relative trajectories appear similar to their absolute counterparts, whereas above the cilia tips the directional fluid flow is absent in the relative separations due to the uniformity of the flow.

above the cilia tips the uniform directionality and relatively constant tracer speeds result in a slope which is nearly ballistic. In contrast, for both flow regimes the relative MSD has a slope of nearly $\kappa = 1$. This implies that, although the tracer motion is cilia-driven and thus largely advective, in both regimes the temporal scaling of the *separation* of particles evolves diffusively. This analysis provides the first evidence that cilia-driven advection can lead to tracer transport which is effectively diffusive. The importance of this observation is that it implies that beating cilia have the potential to generate fluidic mixing by enhancing the rate at which particles spread from each other. However, whether cilia will actually enhance mixing of a species depends on the rate of cilia-driven transport as embodied in the y-intercept of the linear fits to the MSD, as well as the size of the particles (which will affect their rate of intrinsic diffusion). I will return to this discussion briefly.

First I note that, while the primary focus of Figure 6.10 is in the slope, and thus the temporal scaling of the cilia-driven flow, a brief comparison of the effects of the relative dispersion calculation on the y-intercept of the MSDs should also be noted. It has been shown that the difference between the absolute and relative transport rate, which I will now define as the effective diffusivities D_{eff} and D^R_{eff}, respectively, is a function of spatiotemporal correlations between tracers (Babiano et al., 1990). Specifically, in the absence of correlations the relative diffusivity is simply double the absolute diffusivity, or $D^R_{eff} = 2D_{eff}$. The presence of correlations has the effect of reducing D^R_{eff}. In Figure 6.10 the relative dispersion calculation has opposing effects on the y-intercept. Below the cilia tips the y-intercept of the relative motion is precisely double that of the absolute motion. In contrast, above the cilia tips the relative motion has a y-intercept which is significantly less than the absolute motion. This demonstrates the large degree of correlation between tracer motion above the tips and a lack of correlated motion in the flow regime below the tips.

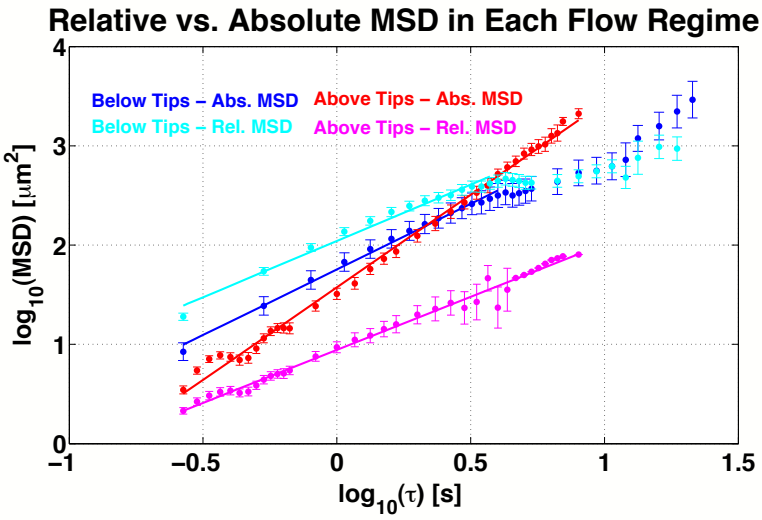

Slope of Relative vs. Absolute MSDs in Each Flow Regime		
Fluid Flow Regime	MSD Type	MSD Slope (κ)
Below Tips	Absolute	1.3 ± 0.1
Below Tips	Relative	1.1 ± 0.2
Above Tips	Absolute	1.86 ± 0.07
Above Tips	Relative	1.07 ± 0.08

Figure 6.10: A comparison of the relative and absolute mean-square displacement (MSD) of ensembles of tracer particles in each flow regime on a log-log scale. The slope of the MSD characterizes the temporal scaling of the transport, with a slope of 1 indicating that the transport scales diffusively. The slopes of the linear fits are given below in the table. For each flow regime, the absolute MSDs reflect a process which is at least partly advective (slopes are greater than 1). However, the relative MSDs each have a slope of nearly 1, indicating that the relative dispersion of the particles scales diffusively. Note that in some cases the linear fits do not include the large τ data points, which due to statistical limitations are more prone to experimental artifacts.

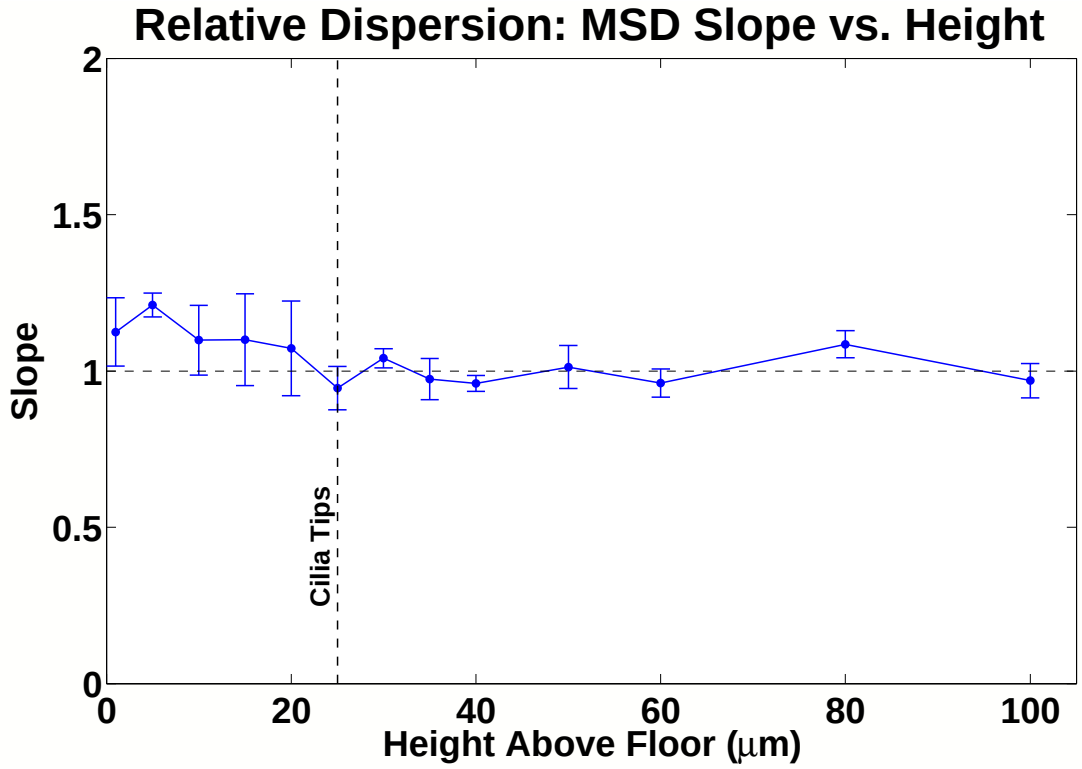

Figure 6.11: The slopes of the relative MSDs at each height above the sample floor, as calculated from linear fits to the log of the MSDs as in Figure 6.10. For each height the slope is approximately 1, indicating that in each flow regime the relative dispersion scales diffusively. Very close to the floor the slopes are slightly elevated due to the slow speeds (and thus the smaller displacements) of the tracers.

To address the rate of the effectively diffusive transport driven by the cilia in my system I performed the relative dispersion calculation on video-tracked tracers at various heights above the sample floor. As with the tracer motion shown for the two heights in Figure 6.10, the slope of the relative MSDs is approximately $\kappa = 1$ at all heights above the floor, demonstrating that the separation of particles evolves diffusively at all heights. The measured slopes are displayed in Figure 6.11 along with error bars which are calculated from the confidence intervals of the linear fits. In almost all cases the slope of 1 expected for a diffusive process is within the error bars. Below the cilia tips the slopes are slightly elevated above 1, which is a result of the fact that at small lag times the motion does evolve advectively. The farther a given tracer is advected by the cilia, the more the slope moves toward 1 because the tracer samples the flow field of an increasing number of cilia, which allows the longer time scale motion to appear effectively diffusive. Very near the floor the slopes are not equal to 1, within error bars, because the tracer motion is relatively slow and thus the duration of tracks does not allow the effective diffusivity to become as apparent as those tracers which move more rapidly, and thus cover more area.

The fact that the majority of these slopes are approximately 1 justifies my definition of the rate of transport as an effective relative diffusivity, D^R_{eff}. Figure 6.12 displays D^R_{eff}, which is obtained from the y-intercept of the linear fits to the relative MSD, at various heights above the floor. As I previously demonstrated, above the cilia tips the tracer dispersion is precisely that expected for the intrinsic diffusive motion of the tracers. In contrast, below the cilia tips the cilia beat produces a significant enhancement relative to this intrinsic motion, up to a factor of approximately 25.

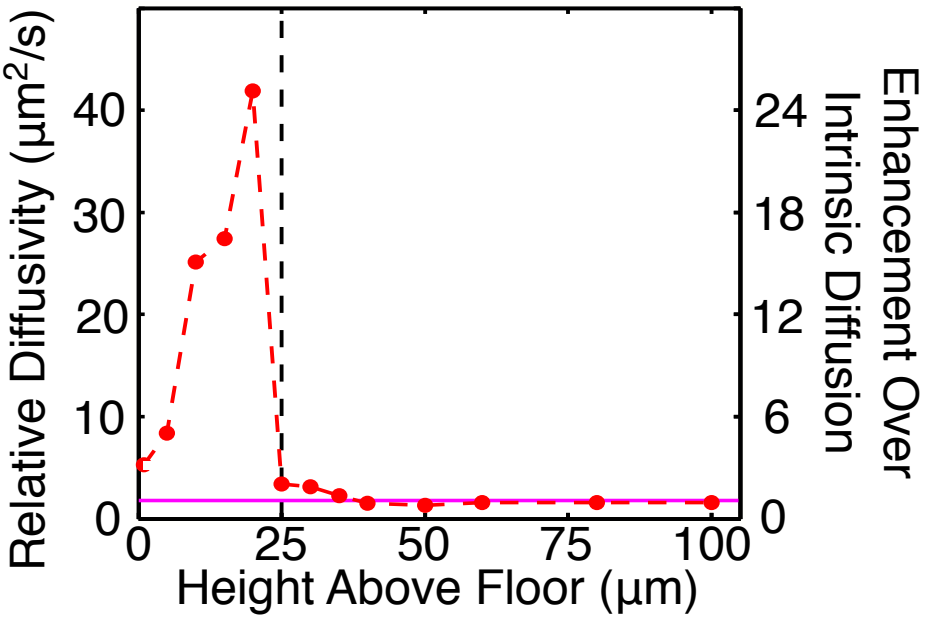

Figure 6.12: The effective relative diffusivity and enhancement as a function of height above the sample floor. The biomimetic cilia motion produces up to a factor of 25 enhancement with respect to the expected relative diffusivity of 1.8 $\frac{\mu m^2}{s}$ (horizontal magenta line). Above the cilia tips (above the vertical dotted line), the relative diffusivity rapidly decays back to the expected value. As a check, the expected relative diffusivity was accurately obtained for diffusing tracers with the biomimetic cilia turned off. Note that vertical error bars are not shown, but are equal to the depth of focus of the microscope, which is on the order of 3 μm.

6.2.1 Size-dependence of the mixing enhancment

As I discussed earlier, a fundamental mechanism to produce fluid mixing is through the spread of a concentrated species due to diffusion. Thus, the enhancement demonstrated in Figure 6.12 implies that the cilia beat in my system produces an equivalent enhancement in the mixing rates of the tracers used in the experiment. However, it is important to note that this enhancement is a function of size. To explore this relationship I assume that D^R_{eff} is independent of particle size, or equivalently that it is solely a property of the velocity field. Under this assumption, the degree to which the cilia beat enhances mixing is simply the ratio of D^R_{eff} to D^R_0. Using the Stokes-Einstein equation for a spherical particle (recall that $D^R_0 = 2D_0$), the 'enhancement factor' for motion in two-dimensions is then given by

$$E_f = \frac{3\pi D^R_{eff}\eta a}{kT}. \tag{6.3}$$

This enhancement factor is essentially a definition of an alternate form of the Péclet number, the dimensionless ratio of advective to diffusive transport which is a critical measure of the fluid flow in systems, like the embryonic node, which depend on the establishment of chemical gradients. Thus, if the enhancement is above 1 than the cilia-driven, effective diffusivity will dominate transport, while if the enhancement is less than 1 than the intrinsic diffusive motion is too fast for the particle transport to be significantly affected by the cilia beat. This enhancement factor is displayed as a function of particle size in Figure 6.13, demonstrating that the velocity fields generated in my system will only enhance diffusive mixing down to particle sizes of roughly 10 nm. This size limit will be important for the biological implications of cilia generated mixing, as I discuss below. In a biological system a large number of variables, such as cilia beat shape, beat frequency, cilia density, and fluid rheology, will have an affect on this size

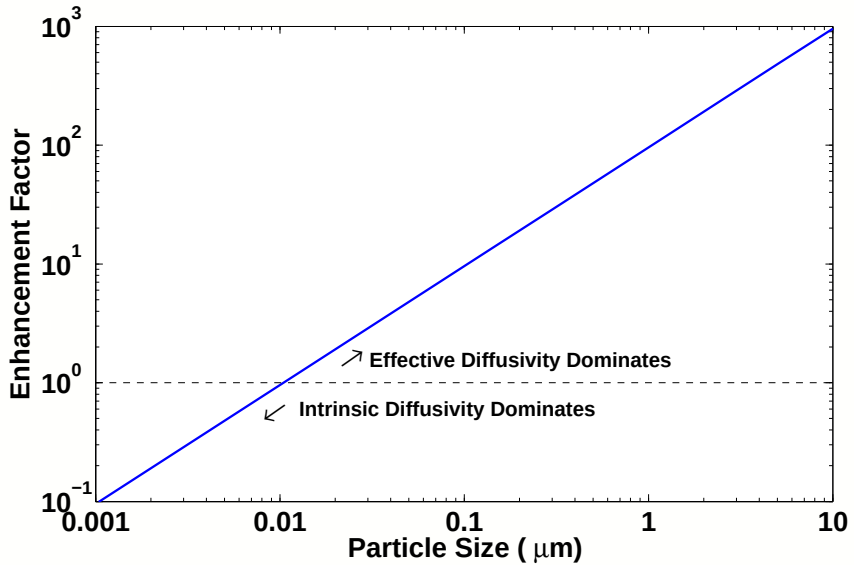

Figure 6.13: The enhancement factor of the cilia-generated mixing below the tips, as calculated from equation 6.3. For smaller particles, their intrinsic diffusive motion begins to dominate the cilia-generated effective diffusivity. Below about 10 nm the intrinsic diffusivity is faster than the cilia-driven flow, and so mixing will no longer be enhanced by the cilia beat.

limit and so it is difficult to predict where this limit lies for biological systems. However, in a study of tracer motion above a field of surface-adhered flagellated bacteria, which exhibited mixing but no net transport, a similar size limit for flagella-driven mixing has been observed (Darnton et al., 2004). On the other hand, airway cilia are around 100 times more densely arrayed than in my samples, and so the enhancement could be more significant in that case.

6.3 Strange Kinetics: Lévy Flights and Chaotic Advection

The framework of describing cilia-driven fluid flow below the cilia tips by an effective diffusivity is useful because it is immediately possible to infer how particles of different sizes will ultimately be transported. However, it is not an exclusive framework with

which to describe the particle motion. In this section I turn to a discussion of two other phenomena which are potentially occurring in cilia-driven fluids flows. These alternative descriptions of the tracer motion are somewhat more abstract than the effective diffusivity, but are also a much richer description of behavior in a dynamical system. Neither phenomena has been previously observed in any ciliated system, biological or otherwise.

While these two phenomena are distinct, the types of dynamical processes which can generate these behaviors share common elements. Specifically, they can both be generated by random processes which have characteristics which are non-Gaussian. The study of such random variables was begun by Paul Lévy in the 1920s and 1930s, among others, as an extension of the central-limit theorem to non-Gaussian processes, with applications from economics to game theory. The development of probability theory around this time is (rather humorously) reviewed by Le Cam (Le Cam, 1986). The processes of interest were those which were scale-invariant. A trajectory in a scale-invariant process has features at many scales, but the behavior looks self-similar regardless of the scale. Diffusion is a self-similar process which is often referred to as a random walk. However, diffusion obeys Gaussian statistics and this type of random walk possesses a characteristic scale determined by the diffusivity (and thus the standard deviation of the Gaussian distribution which describes the process). In contrast, an example of a scale-invariant random walk is one in which the distribution has an infinite variance. In statistics this means that the second moment of the distribution is an integral which diverges to infinity. The conventional understanding of the standard deviation (which is the square root of the variance) as the error expected for a measurement makes an infinite variance difficult to grasp. For this reason, in the box below I reproduce an explanation of the St. Petersburg paradox from Shlesinger et al. (1993) to provide an example of a process with infinite variance.

The St. Petersburg Paradox. "This classic paradox provides us with a beautiful example of a kind of scaling. The problem involves a game of chance. The game is to flip a coin until a head appears. There is a probability of $1/2$ that this occurs on the first flip, and a probability of $1/2^n$ that the first head appears on the nth flip. Suppose you win 2^n coins if $n-1$ tails occur before the first head. Then your expected winnings are

$$(1 \times 1/2) + (2 \times 1/4) + \cdots + (2^n/2^{n+1}) + \cdots = \infty \tag{6.4}$$

... The question is how many coins a player has to risk (the ante) to play. Ideally, in a fair game, the ante should be to equal the expected winnings. The banker requires the player to ante an infinite number of coins because this is his expected loss. The player, however, favours a small ante because he will only win one coin half of the time, two coins or fewer with probability $3/4$, four coins or fewer with probability $7/8$, and so on. The two parties cannot come to an agreement because they are trying to determine a characteristic scale from a distribution which does not possess one. An infinite number of possible scales of winning (in powers of two) enter, but no scale is dominant. The discovery of this paradox was to cast doubt on the firm mathematical foundations of probability theory. Today, we see this paradox as a rich example of scaling with all its inherent exponents, fractal dimensions, and renormalization scaling properties." (Shlesinger et al., 1993)

Fluid dynamics problems are a particularly interesting version of dynamical systems because of the fact that the two-dimensional position of an advected particle is one of the few examples were phase space and real space are equivalent. Given a 2D velocity field, everything there is to know about a particle can be determined by its position. In a phase space, structures which are often responsible for anomalous transport are those which Shlesinger calls 'sticky', meaning that they are locations in phase space in which it is likely for a particle to become trapped for some amount of time before escaping. This, of course, sounds very much like the descriptions I have given of the vortical trapping-and-escape of particles around a cilium, and so it is my speculation that this collection of vortices around each cilium generates particle transport which has anomalous statistical properties.

6.3.1 Lévy Flights

To begin I will demonstrate that the tracer motion below the cilia tips exhibit characteristics of Lévy flights, a type of random walk which is different from the Brownian motion of diffusion. A Lévy flight is simply defined as a random walk in which the size of the steps (or equivalently the velocities at each step) trends towards a distribution with infinite variance. The search for distributions with such characteristics led to the development of the Lévy skew-alpha stable distribution, or just the stable distribution. This distribution is embodied by the four parameters α, β, γ, and δ. These parameters determine, respectively, the rate of decay of the distribution tails, the skewness, the scale (or width), and the location. The distribution function for a stable distribution is not analytically expressible, and forms a family of distributions with special cases which are more familiar. Specifically, a Gaussian distribution is equivalent to a stable distribution which has the parameter α equal to 2 as well as $\beta = 0$. The parameter α is restricted to be in the range $1/2 \leq \alpha \leq 2$. Most importantly, for any $\alpha < 2$ the stable distribution has infinite variance, and so such a process is scale-invariant and can be called a Lévy flight (Shlesinger et al., 1993).

Stable distributions with infinite variance ($\alpha < 2$) are also known as 'heavy-tailed' distributions. Heavy-tailed distributions have larger probabilities for events to occur at the largest values in the distribution. Thus, a Lévy flight has rare, but large excursions from the small steps which are much more likely. In contrast, the peak of the distribution in a Gaussian process can be wider, but the tails of the Gaussian decay much faster and so diffusive random walks to do not exhibit these large excursions from the mean. In nature, Lévy flights have been observed in systems in which an organism is hunting. Whether it be a bacterium's search for nutrients or a child's search for a good hiding spot to play hide-and-seek, the motion consists initially of small steps (as the child, for example, looks around the local area for a good spot), and then occasional

large excursions (as the child runs to a new area to search for a better spot). Bacteria do this in their hunt for nutrients in order to outrun the effects of diffusion. In other words, if bacteria did not perform Lévy flights then there would be little reason to move at all, because without the large excursions the bacterium cannot move faster than diffusion (Berg and Anderson, 1973).

I have previously displayed the velocity distribution of the tracer motion below the cilia tips, and in that case I fit a skew normal distribution to the data. However, I now make it clear that this skew normal distribution was really a subset of the stable distribution, with some skew, and with $\alpha = 2$. However, the astute reader will notice that this fit was not a good match for the tails of the distribution. If the skew is fixed to be zero, then the normal distribution does an even poorer job of describing the data.

In Figure 6.14 I reinforce this notion by plotting a number of velocity distributions with Gaussian and stable distributions fits to the data. I have plotted two methods of matching a Gaussian (see caption), and neither fits the data. One method does not match either the tails or the peak, whereas the second method fits the peak relatively well, but indicates that the data is heavier-tailed than a Gaussian, an indication that the particles are undergoing Lévy flights. Finally, another separate method is to only look at the distribution's tail asymptotics, as shown in Figure 6.14c. For the family of stable distributions with $\alpha < 2$ the rate of decay of the tail should go as $x^{-(1+\alpha)}$ (Shlesinger et al., 1993).

The long excursions exhibited by a Lévy flight increase the rate at which a species can explore a given area, which for a passive species is essentially analogous to an increase in mixing rates. In other words, if biological cilia were to generate particle motion which was a Lévy flight, then this particle motion would rapidly explore an area of the environment that would take it much longer to reach by its intrinsic diffusive motion. As I will discuss, this could have implications for how biochemical signaling

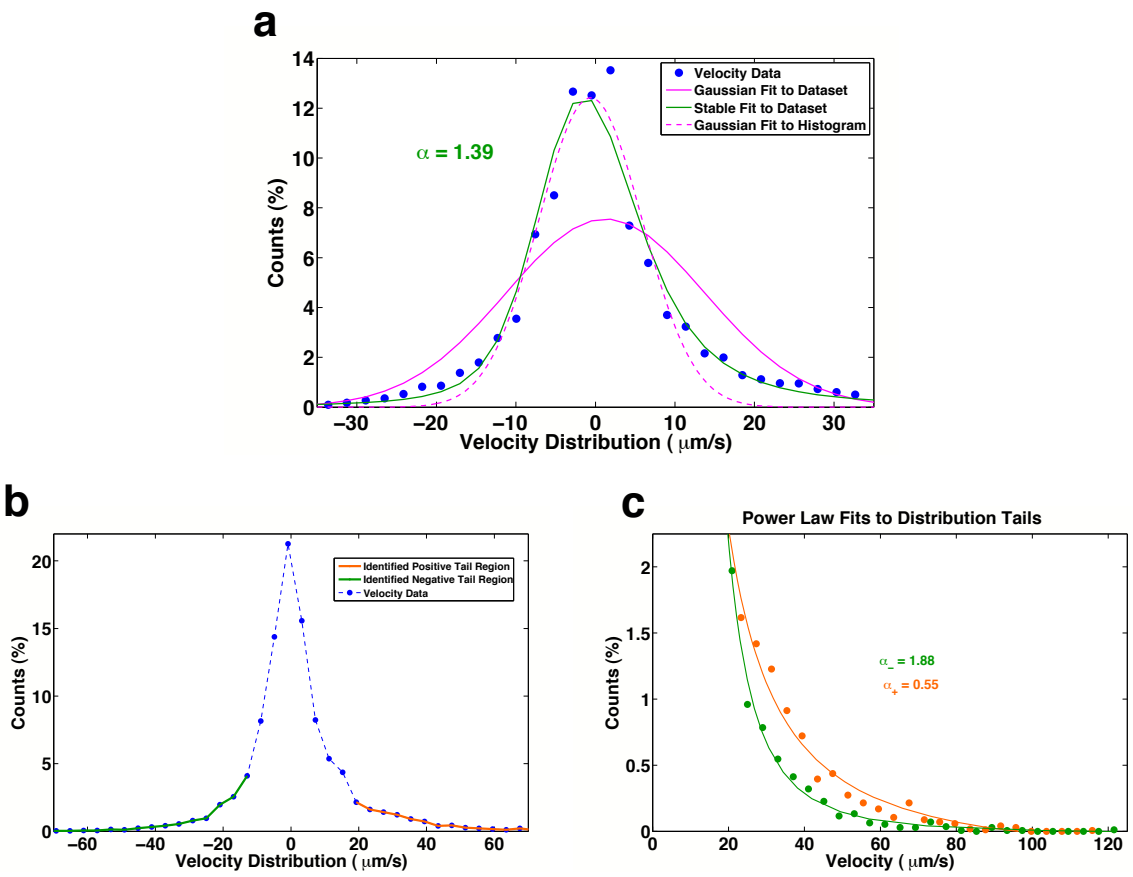

Figure 6.14: Velocity distributions of the cilia-driven flow exhibit non-Gaussian statistics. In (a) I plot several ways to fit a Gaussian to the distribution. The solid magenta line is the Gaussian distribution which has the same mean and standard deviation as the velocity dataset. In contrast, the dotted magenta line is a true fit to the histogram itself. Both examples show how the velocity distribution is non-Gaussian, and a stable distribution fit with $\alpha = 1.39$ matches the data well. Another method for determining α is the asymptotics of the tails of the distribution, as identified in (B) (I define the tails to be the point where the probability drops by a factor of 10 from the maximum). In (c) I have taken both tails and fit them to a power law to determine α separately for each tail. In each case, α is less than two, indicating the velocity distributions are infinite variance and thus the particle trajectories are Lévy flights.

processes might have evolved within ciliated systems.

6.3.2 Chaotic Advection

At the beginning of this chapter I described the importance difference between stirring and mixing. Stirring produces stretching and folding of a fluid element, which can dramatically increase the interfacial area between two unmixed fluids. In the presence of diffusion this increase in interfacial area allows a fully mixed state to be obtained much more rapidly. At large Reynolds numbers the onset of turbulence allows stirring processes to generate well-mixed states at all but the smallest scales, but in laminar flow it was long thought that diffusion would be required to produce full mixing.

However, in the last 25 years a new appreciation has developed for the existence of rich chaotic behavior even in low Reynolds number fluids. This behavior, known as chaotic advection or Lagrangian chaos, is a phenomenon whereby relatively simple Eulerian velocity fields can produce particle pathlines which are inherently unpredictable and, thus, chaotic. Although initially controversial, chaotic advection was established in the 1980s as an application of dynamical systems and has since been well validated by theory and experiment (Aref and Balachandar, 1986; Ottino, 1990).

As I mentioned in Chapter 3, a hallmark of chaos is the rapid divergence of closely spaced particles. Mathematically, chaotic advection requires that an infinitesimally small separation between particles grow at an exponential rate for a sufficiently long time. This exponential rate is defined as the Lyapunov exponent

$$\lambda = \lim_{x_0 \to 0} \frac{1}{t} ln \left(\frac{x(t)}{x_0} \right) \tag{6.5}$$

where x_0 is the initial separation. More recently, however, the increasingly widespread use of the Lyapunov exponent as a measure of dispersion in theoretical and experimental

systems has inspired several more practical forms such as the finite-size Lyapunov exponent (FSLE) and the finite-time Lyapunov exponent (Kleinfelter et al., 2005).

Another method for treatments of chaotic advection uses the coincidence of phase space and real space in order to analyze chaotic motion via Poincaré maps. This type of map describes the equations of motion of a set of particles which are seeded at initial points within the velocity field. At discrete time intervals each particle's current position is mapped to a new position, and many iterations of this produces a map of locations in phase space which were visited by a particle. In regions where the flow is not chaotic these mappings are well-behaved and dots can be easily connected to reveal the streamlines of the flow. In contrast, in other regions these mappings produce a series of positions which are stochastic and thus chaotic. These stochastic areas are often bounded by well-behaved streamlines and are thus known as 'chaotic seas' (Shlesinger et al., 1993).

The same types of phase space topologies which give rise to Lévy flights can also produce chaotic advection. Specifically, Poincaré maps reveal that the areas of phase space which can trap particles are often adjacent to chaotic seas. This implies that, in close proximity to an area where trapping occurs, particle motion can be chaotic as the particle traverses the local phase space.

The initial resistance to the notion of chaos at low Reynolds number stems from the more common connection between chaotic motion and turbulent flow. As turbulence cannot be supported by a low Reynolds number fluid the presence of chaos in a laminar flow was initially met with controversy. However, simple experiments have demonstrated that it can actually be difficult to prevent at least a degree of chaotic motion from occurring in a time-dependent, low Reynolds number flow, even if the time-dependence is simply periodic.

In addition, relatively recent theoretical work has begun to identify chaos within

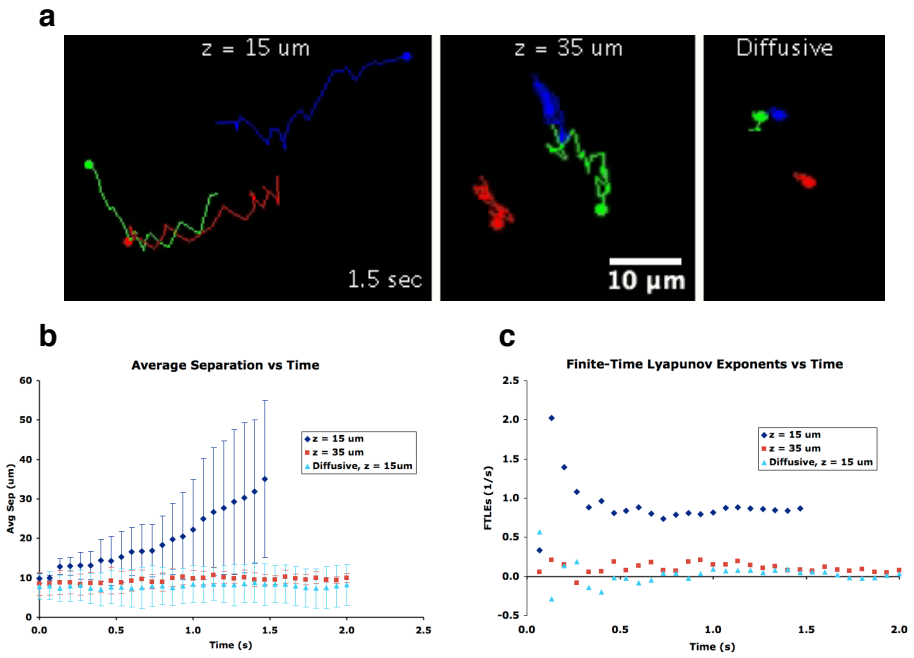

Figure 6.15: A hallmark of chaotic advection is the exponential growth of the separation between pairs of particles. Below the cilia tips I regularly observe such phenomena, but it can be difficult to find pairs which can both be tracked for a significant duration after they begin to separate. In the absence of such data, it is difficult to call a behavior chaotic. However, I note that the average separation of the three particles below the cilia tips does indeed give a finite-time Lyapunov exponent which appears to be approaching a non-zero value as time increases.

the low Reynolds number flows generated by flagella. As the velocity field around a cilium is certainly time-dependent, it would thus come as some surprise if cilia were not capable of generating chaotic motion. However, up to now chaos has not been observed in any ciliated system. Of course, the extent to which the cilia beat can generate chaos will be strongly-dependent on the interactions between neighboring cilia.

For these reasons, I believe that it is highly likely that cilia generate at least transient chaotic behavior, and yet I want to be clear that I am not claiming to have successfully identified chaos in my ciliated systems. In Figure 6.15 I present data analogous to that of Supatto et al., in that it shows the relatively rapid divergence of nearby tracers. Furthermore, this divergence does in fact give rise to a finite-time Lyapunov exponent which is non-zero. However, this by itself is not sufficient proof that the flows are

chaotic (although it is already more rigorous than the data presented to support the claims made by Supatto et al.). Instead I display these results as indications of possible future experiments, as providing the first measurement of chaotic particle motion in a ciliated system would be another excellent example of the utility of a biomimetic cilia model. In order to do this would likely require a large number of such initially closely spaced pairs to be found, as one of the main difficulties in quantifying the chaotic behavior is that it can be difficult or impossible to follow any single particle for a long duration in the complicated flows below the cilia tips.

6.4 Implications for Biology

To conclude this thesis, I end this chapter by reviewing the results I have presented and reiterating the implications of these results for biological ciliated systems. From a technological point of view, artificial cilia have great promise as responsive nanostructures for manufacturing, sensing, self-cleaning, and myriad other arenas where microscale manipulation will be required. As I have tried to make clear, however, in some sense the most interesting application of a truly biomimetic cilium is to attempt to illuminate issues of relevance for biological systems.

As these biological systems can be difficult to study, the observations and analyses I have presented constitute some of the most detailed characterizations of cilia-driven fluid flows in the literature. The discovery of the embryonic node has proven to be a fertile ground for biomimetic cilia to explore. This system plays a critically important role in embryological development, and yet little is known about its detailed workings because of the novelty of the system and the difficulty of experimentation. It has been appreciated that in order to transduce the physical fluid flow which the cilia drive into asymmetric chemical expression the node must properly balance the advective and diffusive transport of the various species in the nodal fluid. Biological experiments

have been almost exclusively focused on the fluid flow above the cilia tips, in which the uniform directionality produces a morphogen gradient. My results highlight additional challenges faced by such a system, namely that the cilia can drive mixing flows below their tips which could affect the evolution or establishment of a gradient.

One of these main challenges is represented by the Péclet number, which determines whether the cilia-driven transport is rapid enough to overcome the diffusive transport that will work to homogenize any molecular gradients. My results show that below the cilia tips the flow lacks any directionality. Thus, in order to achieve the initial gradient the morphogens must be able to reach the flow regime above the cilia tips and then be transported at $Pe > 1$.

I have previously described how sheathed lipid vesicles are loaded with morphogens, dynamically extended from the cellular surface by microvilli, and released into the flow above the tips. After crossing the node the NVPs rupture to release their signaling cargo. This release generates the initial asymmetric gradient which is transduced into the left-side signaling cascade. This mechanism addresses both of the initial challenges which are imposed by the mixing regime below the cilia tips. The extension of the microvilli into the flow above the tips allows the NVPs to avoid any mixing regime, while the transportation of the signaling molecules within the much larger vesicle allows them to cross the node at a higher Péclet number. Thus, the rapid diffusive motion of the molecules do not affect the distribution of morphogens until after the rupture of the NVP.

The healthy functioning of this mechanism poses another challenge to the system. At the time of the discovery of the NVPS, it was also shown that the proper formation the NVPs and their release from the microvilli required fibroblast growth factor (FGF) signaling. In contrast to the morphogens for left-side signaling, it is likely that the FGF signaling efficiency is increased by a uniform distribution of FGF across the nodal floor.

In this case, it may be that cilia-generated mixing of the FGF may serve to increase the efficiency of this signaling process.

To reiterate, I am thus suggesting the possibility that signaling processes in ciliated systems could take advantage of the differential affects of cilia-driven flows on morphogens of different sizes. If cilia drive an effectively diffusive flow, then there is some critical particle size below which the advective flow is unimportant. Above this size, however, cilia-driven flow could enhance mixing and increase reaction rates, thus facilitating the signaling process. In the node this might allow FGF to be mixed by cilia, while smaller morphogens persist in any established gradient until their intrinsic diffusive motion has had time to homogenize the solution. In the airways, such a system might affect the way in which the system maintains the airway surface liquid. For example, blobs of mucus are released from goblet cells and must somehow join the mucus layer above the cilia. These mucus blobs are large enough to be mixed in a cilia-driven flow, and so the transport and distribution of these objects might be determined by cilia. Finally, chemical gradients have also been shown to be important in oviductal and ependymal cilia systems, and these systems are even more poorly characterized than the airway or nodal cilia. In any of these organs it is possible that cilia-driven mixing has been harnessed in some way which assists the system in its functionality. Conversely, as with the dynamic launching of the NVPs from microvilli, ciliated systems may have had to evolve mechanisms which ensured that cilia-driven mixing was not detrimental to function.

Another nodal cilia issue which has been speculated upon is the intriguing possibility that sensors on the cilia themselves, either the motile or the immotile class, participate in the left-side signaling cascade (Cartwright et al., 2007; Hirokawa et al., 2009). This idea is bolstered by increasing evidence that cilia play a chemosensory role in other biological systems, such as in the airways were taste receptors have been found on the

ciliary membrane (Shah et al., 2009). Despite the fact that my results suggest that the intrinsic diffusive motion of small molecules is likely to dominate their transport within the node, it is possible that localizing the sensory mechanism on the surface of cilia compensates for hydrodynamic effects within this regime.

Specifically, as diffusive motion can be significantly inhibited by the presence of a no-slip boundary, the stirring generated by the cilia could counteract the effects of the surface to slow down the chemosensory process. Sensors on the cilia themselves would reduce the surface inhibition of the molecules diffusive motion simply by being elevated above the planar surface, and the motion of the cilium relative to the fluid might increase the exposure of receptors on the cilium to morphogens in the solution.

These examples highlight the exciting future for biomimetic cilia system and responsive microstructures in general. With a robust, well-developed fabrication process, methodologies for mimicking the beat of biological cilia, and protocols, analysis techniques, and theoretical benchmarks for characterizing cilia-driven fluid flows, the work I have presented in this thesis will hopefully be of interest to the diverse audience for which it was written. My experience in the world of biomimetics, one of the increasing number of fields which requires a highly interdisciplinary, collaborative approach, has been entirely positive. I have enjoyed the struggles and the successes associated with building responsive structures at the nanometer scale, and look forward to both my own next challenge as well as the next generation of exciting results which will be obtained with biomimetic cilia. Finally, I implore all those who would come after me to remember a rule which describes many aspects of nanotechnology, but more importantly is my cardinal rule for successfully fabricating biomimetic cilia: you are only as good as your best pair of tweezers.

Bibliography

Albensoeder, S., Kuhlmann, H., and Rath, H. (2001). Three-dimensional centrifugal-flow instabilities in the lid-driven-cavity proble. *Physics of Fluids*, 13(1):121–135.

Alexeev, A., Yeomans, J. M., and Balazs, A. C. (2008). Designing synthetic, pumping cilia that switch the flow direction in microchannels. *Langmuir*, 24(21):12102–6.

Aref, H. and Balachandar, S. (1986). Chaotic advection in a stokes flow. *Physics of Fluids*, 29:3515.

Artale, V., Boffetta, G., Celani, A., Cencini, M., and Vulpiani, A. (1997). Dispersion of passive tracers in closed basins: Beyond the diffusion coefficient. *Phys. Fluids*, 9(11):3162–3171.

Azzalini, A. (1985). A class of distributions which includes the normal ones. *Scand. J. Statistics*, 12:171–178.

Babiano, A., Basdevant, C., Le Roy, P., and Sadourny, R. (1990). Relative dispersion in two-dimensional turbulence. *Journal of Fluid Mechanics Digital Archive*, 214:535–557.

Badano, J. L., Mitsuma, N., Beales, P. L., and Katsanis, N. (2006). The ciliopathies: an emerging class of human genetic disorders. *Annu Rev Genomics Hum Genet*, 7:125–48.

Baltussen, M., Anderson, P., Bos, F., and den Toonder, J. (2009). Inertial flow effects in a micro-mixer based on artificial cilia. *Lab Chip*, 9(16):2326–31.

Barthlott, W. and Neinhuis, C. (1997). Purity of the sacred lotus, or escape from contamination in biological surfaces. *Planta*, 202:1–8.

Batchelor, G. (1970). Slender-body theory for particles of arbitrary cross-section in stokes flow. *J. Fluid Mechanics*, 44(3):419–440.

Bellomo, D., Lander, A., Harragan, I., and Brown, N. A. (1996). Cell proliferation in mammalian gastrulation: the ventral node and notochord are relatively quiescent. *Dev Dyn*, 205(4):471–85.

Berg, H. C. and Anderson, R. A. (1973). Bacteria swim by rotating their flagellar filaments. *Nature*, 245:380–384.

Biswal, S. L. and Gast, A. P. (2004). Micromixing with linked chains of paramagnetic particles. *Anal Chem*, 76(21):6448–55.

Blake, J. (1970). Infinite models for ciliary propulsion. *J. Fluid Mechanics*, 49(2):209–222.

Bouzarth, E. L., Brooks, A., Camassa, R., Jing, H., Leiterman, T. J., McLaughlin, R. M., Superfine, R., Toledo, J., and Vicci, L. (2007). Epicyclic orbits in a viscous fluid about a precessing rod: theory and experiments at the micro- and macro-scales. *Phys Rev E Stat Nonlin Soft Matter Phys*, 76(1 Pt 2):016313.

Brennen, C. and Winet, H. (1977). Fluid mechanics of propulsion by cilia and flagella. *Annual Review of Fluid Mechanics*, 9:339–398.

Bye, J. A. (1966). Numerical solutions of the steady-state vorticity equation in rectangular basins. *J. Fluid Mech.*, 26(3):577–598.

Cartwright, J. H. E., Piro, N., Piro, O., and Tuval, I. (2007). Embryonic nodal flow and the dynamics of nodal vesicular parcels. *J R Soc Interface*, 4(12):49–55.

Cartwright, J. H. E., Piro, N., Piro, O., and Tuval, I. (2008). Fluid dynamics of nodal flow and left-right patterning in development. *Dev Dyn*, 237(12):3477–90.

Cartwright, J. H. E., Piro, O., and Tuval, I. (2004). Fluid-dynamical basis of the embryonic development of left-right asymmetry in vertebrates. *Proc Natl Acad Sci U S A*, 101(19):7234–9.

Darnton, N., Turner, L., Breuer, K., and Berg, H. C. (2004). Moving fluid with bacterial carpets. *Biophys J*, 86(3):1863–70.

Einstein, A. (1905). On the movement of small particles suspended in stationary liquids required by the molecular-kinetic theory of heat. *Annalen der Physik*, 17:549–560.

Eley, L., Yates, L. M., and Goodship, J. A. (2005). Cilia and disease. *Curr Opin Genet Dev*, 15(3):308–14.

Essner, J. J., Vogan, K. J., Wagner, M. K., Tabin, C. J., Yost, H. J., and Brueckner, M. (2002). Left-right development: Conserved function for embryonic nodal cilia. *Nature*, 418(6893):37–38.

Evans, B. (2008). *Design, fabrication, and actuation of biomimetic cilia.* PhD thesis, UNC - Chapel Hill.

Evans, B. A., Shields, A. R., Carroll, R. L., Washburn, S., Falvo, M. R., and Superfine, R. (2007). Magnetically actuated nanorod arrays as biomimetic cilia. *Nano Letters*, 7(5):1428–1434.

Fahrni, F., Prins, M. W. J., and van Ijzendoorn, L. J. (2009). Micro-fluidic actuation using magnetic artificial cilia. *Lab Chip*, 9(23):3413–21.

Fauci, L. J. and Dillon, R. (2006). Biofluidmechanics of reproduction. *Annu. Rev. Fluid Mech.*, 38:371–94.

Geim, A. K., Dubonos, S. V., Grigorieva, I. V., Novoselov, K. S., Zhukov, A. A., and Shapoval, S. Y. (2003). Microfabricated adhesive mimicking gecko foot-hair. *Nat Mater*, 2(7):461–3.

Gravesen, P., Branebjerg, J., and Jensen, O. (1993). Microfluidics - a review. *J. Micromech. Microeng.*, 3:168–182.

Gray, J. and Hancock, G. (1955). The propulsion of sea-urchin spermatozoa. *J. Experimental Biology*, 32(802-814).

Hansen, W. R. and Autumn, K. (2005). Evidence for self-cleaning in gecko setae. *Proc Natl Acad Sci U S A*, 102(2):385–9.

Happel, J. and Brenner, H. (1963). *Low Reynolds number hydrodynamics*. Martinus Nijhoff, Netherlands, 3rd edition.

He, M., Kuo, J., and Chiu, D. (2005). Electro-generation of single femtoliter- and picoliter-volume aqueous droplets in microfluidics systems. *Applied Physics Letters*, 87(031916).

Hirokawa, N. (1998). Kinesin and dynein superfamily proteins and the mechanism of organelle transport. *Science*, 279(5350):519–26.

Hirokawa, N., Okada, Y., and Tanaka, Y. (2009). Fluid dynamic mechanism responsible for breaking the left-right symmetry of the human body: The nodal flow. *Annual Review of Fluid Mechanics*, 41:53–72.

Keller, S., Wu, T., and Brennen, C. (1975). A traction-layer model for ciliary propulsion. *Proceedings of the Symposium on Swimming and Flying in Nature*, pages 253–271.

Kim, M. J. and Breuer, K. S. (2008). Microfluidic pump powered by self-organizing bacteria. *Small*, 4(1):111–8.

Kleinfelter, N., Moroni, M., and Cushman, J. (2005). Application of the finite-size lyapunov exponent to particle tracking velocimetry in fluid mechanics experiments. *Phys. Rev. E*, 72(056306).

Koseff, J. R. and Street, R. L. (1984). The lid-driven cavity flow: a synthesis of qualitative and quantitative observations. *Journal of fluids engineering*, 106(4):390–398.

LaCasce, J. H. and Bower, A. (2000). Relative dispersion in the subsurface north atlantic. *Journal of Marine Research*, 58(6):863–894.

Lau, K., Bico, J., Teo, K., Chhowalla, M., Amaratunga, G., McKinley, G., and Gleason, K. (2003). Superhydrophobic carbon nanotube forests. *Nano Letters*, 3(12):1701–1705.

Le Cam, L. (1986). The central limit theorem around 1935. *Statistical Science*, 1(1):78–91.

Liron, N. (1978). Fluid transport by cilia between parallel plates. *Journal of Fluid Mechanics Digital Archive*, 86(04):705–726.

Liron, N. and Meyer, F. A. (1980). Fluid transport in a thick layer above an active ciliated surface. *Biophys J*, 30(3):463–72.

Matsui, H., Randell, S. H., Peretti, S. W., Davis, C. W., and Boucher, R. C. (1998). Coordinated clearance of periciliary liquid and mucus from airway surfaces. *J Clin Invest*, 102(6):1125–31.

McGrath, J., Somlo, S., Makova, S., Tian, X., and Brueckner, M. (2003). Two populations of node monocilia initiate left-right asymmetry in the mouse. *Cell*, 114(1):61–73.

Mitran, S. M. (2007). Metachronal wave formation in a model of pulmonary cilia. *Comput Struct*, 85(11-14):763–774.

Mitran, S. M., Forest, M. G., Yao, L., Lindley, B., and Hill, D. B. (2008). Extensions of the ferry shear wave model for active linear and nonlinear microrheology. *J Nonnewton Fluid Mech*, 154(2-3):120–135.

Narasimhan, T. (2009). The dichotomous history of diffusion. *Physics Today*, 62(7):48–53.

Navier, L. (1827). Sur les lois de l'équilibre et du mouvement des corps élastiques. *Mem. Acad. Sci.*, 6:389.

Newton, I. (1687). The mathematical principles of natural philosophy.

Nonaka, S., Shiratori, H., Saijoh, Y., and Hamada, H. (2002). Determination of left-right patterning of the mouse embryo by artificial nodal flow. *Nature*, 418(6893):96–9.

Nonaka, S., Tanaka, Y., Okada, Y., Takeda, S., Harada, A., Kanai, Y., Kido, M., and Hirokawa, N. (1998). Randomization of left-right asymmetry due to loss of nodal cilia generating leftward flow of extraembryonic fluid in mice lacking kif3b motor protein. *Cell*, 95(6):829–37.

Nonaka, S., Yoshiba, S., Watanabe, D., Ikeuchi, S., Goto, T., Marshall, W. F., and Hamada, H. (2005). De novo formation of left-right asymmetry by posterior tilt of nodal cilia. *PLoS Biol*, 3(8):e268.

Oh, K., Chung, J.-H. H., Devasia, S., and Riley, J. J. (2009). Bio-mimetic silicone cilia for microfluidic manipulation. *Lab Chip*, 9(11):1561–6.

Okada, Y., Takeda, S., Tanaka, Y., Belmonte, J.-C. I. C., and Hirokawa, N. (2005). Mechanism of nodal flow: a conserved symmetry breaking event in left-right axis determination. *Cell*, 121(4):633–44.

Ottino, J. (1990). Mixing, chaotic advection, and turbulence. *Annu. Rev. Fluid Mech.*, 22:207–253.

Pamme, N. (2006). Magnetism and microfluidics. *Lab Chip*, 6(1):24–38.

Pazour, G. J. and Witman, G. B. (2003). The vertebrate primary cilium is a sensory organelle. *Curr Opin Cell Biol*, 15(1):105–10.

Praetorius, H. A. and Spring, K. R. (2001). Bending the mdck cell primary cilium increases intracellular calcium. *Journal of Membrane Biology*, 184(1):71–79.

Roca-Cusachs, P., Rico, F., Martínez, E., Toset, J., Farré, R., and Navajas, D. (2005). Stability of microfabricated high aspect ratio structures in poly(dimethylsiloxane). *Langmuir*, 21(12):5542–8.

Ruibal, R. and Ernst, V. (1965). The structure of the digital setae of lizards. *J Morphol*, 117(3):271–93.

Satir, P. and Christensen, S. T. (2007). Overview of structure and function of mammalian cilia. *Annu Rev Physiol*, 69:377–400.

Sawamoto, K., Wichterle, H., Gonzalez-Perez, O., Cholfin, J. A., Yamada, M., Spassky, N., Murcia, N. S., Garcia-Verdugo, J. M., Marin, O., Rubenstein, J. L. R., Tessier-Lavigne, M., Okano, H., and Alvarez-Buylla, A. (2006). New neurons follow the flow of cerebrospinal fluid in the adult brain. *Science*, 311(5761):629–32.

Shah, A. S., Ben-Shahar, Y., Moninger, T. O., Kline, J. N., and Welsh, M. J. (2009). Motile cilia of human airway epithelia are chemosensory. *Science*.

Shah, R. and London, A. (1978). Laminar flow forced convection in ducts. *Adv. Heat Transf. Sppl. 1*.

Sharma, N., Berbari, N., and Yoder, B. (2008). Ciliary dysfunction in developmental abnormalities and diseases. *Current Topics in Developmental Biology*, 85:371–413.

Shlesinger, M., Zaslavsky, G., and Klafter, J. (1993). Strange kinetics. *Nature*, 363:31–37.

Sidorenko, A., Krupenkin, T., Taylor, A., Fratzl, P., and Aizenberg, J. (2007). Reversible switching of hydrogel-actuated nanostructures into complex micropatterns. *Science*, 315(5811):487–90.

Singh, H., Laibinis, P. E., and Hatton, T. A. (2005). Synthesis of flexible magnetic nanowires of permanently linked core-shell magnetic beads tethered to a glass surface patterned by microcontact printing. *Nano Lett*, 5(11):2149–54.

Sleigh, M. and Aiello, E. (1972). The movement of water by cilia. *Acta. Protozool.*, 11:265–277.

Smith, D. J., Blake, J. R., and Gaffney, E. A. (2008). Fluid mechanics of nodal flow due to embryonic primary cilia. *J R Soc Interface*, 5(22):567–73.

Smith, D. J., Gaffney, E. A., and Blake, J. R. (2007). Discrete cilia modelling with singularity distributions: application to the embryonic node and the airway surface liquid. *Bull Math Biol*, 69(5):1477–510.

Squires, T. M. and Quake, S. R. (2005). Microfluidics: Fluid physics at the nanoliter scale. *Rev Mod Phys*, 77(3):977–1026.

Suh, J., Glander, S., Darling, R., Storment, C., and Kovacs, G. (1997). Organic thermal and electrostatic ciliary microactuator array for object manipulation. *Sensors and Actuators A*, 58:51–60.

Sulik, K., Dehart, T. I., Carson, J., Vrablic, T., Gesteland, K., and Schoenwolf, G. (1994). Morphogenesis of the murine node and notochordal plate. *Dev. Dynamics*, 201:260–278.

Supatto, W., Fraser, S. E., and Vermot, J. (2008). An all-optical approach for probing microscopic flows in living embryos. *Biophys J*, 95(4):L29–31.

Tabata, O., Hirasawa, H., Aoki, S., Yoshida, R., and Kokufuta, E. (2002). Ciliary motion actuator using self-oscillating gel. *Sensors & Actuators: A. Physical*, 95(2-3):234–238.

Tabin, C. J. and Vogan, K. J. (2003). A two-cilia model for vertebrate left-right axis specification. *Genes Dev*, 17(1):1–6.

Talbot, P., Geiske, C., and Knoll, M. (1999). Oocyte pickup by the mammalian oviduct. *Mol. Biol. Cell*, 10:5–8.

Tanaka, Y., Okada, Y., and Hirokawa, N. (2005). Fgf-induced vesicular release of sonic hedgehog and retinoic acid in leftward nodal flow is critical for left-right determination. *Nature*, 435(7039):172–7.

Taylor, G. (1951). Analysis of the swimming of microscopic organisms. *Proc. of the Royal Society of London, Series A*, 209(1099):447–461.

Toonder, J. d., Bos, F., Broer, D., Filippini, L., Gillies, M., de Goede, J., Mol, T., Reijme, M., Talen, W., Wilderbeek, H., Khatavkar, V., and Anderson, P. (2008). Artificial cilia for active micro-fluidic mixing. *Lab Chip*, 8(4):533–41.

van Oosten, C. L., Bastiaansen, C. W. M., and Broer, D. J. (2009). Printed artificial cilia from liquid-crystal network actuators modularly driven by light. *Nat Mater*, 8(8):677–82.

Vilfan, M., Potocnik, A., Kavcic, B., Osterman, N., Poberaj, I., Vilfan, A., and Babic, D. (2009). Self-assembled artificial cilia. *Proc Natl Acad Sci U S A*.